Miniaturized Air-to-Refrigerant Heat Exchangers
US DOE Award: DE-EE0006114

Final Report

PI: Reinhard Radermacher
Co-Authors: Daniel Bacellar, Vikrant Aute, Zhiwei Huang, Yunho Hwang, Jiazhen Ling, Jan Muehlbauer, James Tancabel, Omar Abdelaziz, Mingkan Zhang

Partners: Oak Ridge National Laboratory (ORNL), Luvata, International Copper Association (ICA), Heat Transfer Technologies (HTT), Wieland, Burr Oak Tool

Center for Environmental Energy Engineering
Department of Mechanical Engineering
University of Maryland
College Park, MD 20742-3035

May 2017

Contents

List of Figures 4
List of Tables 6
Acknowledgement 7
Disclaimer 7
Team Members 8
Executive Summary 10
1 Introduction 11
1.1 Project Objective and Background 11
1.2 Summary of Project Achievements 11
2 Heat Exchanger Analysis 12
2.1 CFD Modeling and Simulation 13
2.1.1 Airside Modeling 13
2.1.2 CFD Modeling and Simulation 13
2.1.3 CFD Data Reduction 16
2.1.4 CFD Grid Uncertainty Analysis 17
2.2 1.0kW Radiator Optimization Results 19
2.2.1 Prototypes and Experimental Validations 21
2.3 10kW Radiator Optimization Results 25
2.4 Two-Phase HX Optimization 26
2.4.1 HX Design and Optimization 27
2.4.2 System Level Analysis 29
2.4.3 Charge Optimization 30
2.5 Additional Mini Heat Exchanger Geometries 31
2.5.1 Alternative Offset-Strip Fin Heat Exchanger 31
2.5.2 Pipe-Attached Fins Heat Exchanger 33
2.5.3 Airfoil/Droplet Shape Heat Exchanger 33
2.5.4 EHD-Enhanced Mini Heat Exchanger 35
3 Experimental Work 37
3.1 Test Facility Description 37
3.1.1 Airside Test Facility 37
3.1.2 Refrigerant Side Test Facility 38
3.2 NTHX-001 40

3.2.1 Wilson Plot Method *42*
3.2.2 Experimental Results *43*
3.3 BTHX-001 45
3.3.1 Wilson Plot Method *45*
3.3.2 Test Matrix *47*
3.3.3 Vertical Orientation *48*
3.3.4 Horizontal Orientation *52*
3.4 Experimental Validation: 1.0kW Air-to-Water HX 55
3.5 10 kW BTHX 56
3.5.1 Blockage Test and Cleaning *56*
3.5.2 Dry Condition Results, Pre-Cleaning *57*
3.5.3 Dry Condition Results, Post-Cleaning *60*
3.5.4 Dry Condition Results, Comparison, Pre- and Post-Cleaning *62*
3.5.5 Dry Condition Results Comparsion, Experimental and Simulation *63*
3.6 WTHX Concept 65
3.7 Uncertainty Analysis 68
3.8 Lessons Learned 68
4 CFD-Based Correlation Development 69
5 List of Publications 70
6 List of Inventions 71
7 Future Work 71
8 References 72
Appendix A – Round Bare Tubes 75
Appendix B – NURBS Shape Tubes 77
Appendix C – BTHX-001 Test Data Tables 78

List of Figures

Figure 1 – Typical CFD Two-dimensional Computational Domain. 14
Figure 2 – Two-dimensional Computational Domain Mesh Schemes: a) Triangle; b) Quadrilateral. 14
Figure 3 – Typical CFD Three-dimensional Computational Domain. 15
Figure 4 – Dry Air Properties as Funcitons of Temperature. 16
Figure 5 – Sequentially Increasing Grid Resolutions. 18
Figure 6 – Radiator Optimum Designs: Air DP vs. Heat Exchanger Volume. 20
Figure 7 – RTHX-001 Prototype Drawing. 22
Figure 8 – Stainless Steel RTHX-001 Sample Images. 22
Figure 9 – NTHX-001 Prototype Drawing. 23
Figure 10 – NTHX-001 Sample Images. 23
Figure 11 – Experimental Validation: Energy Balance and Overall Capacity. 24
Figure 12 – Experimental Validation: Airside Heat Transfer Coefficient and Pressure Drop. 24
Figure 13 – NTHX-001 CFD Validation: Contour Plots. 25
Figure 14 – DP II: Optimization Results. 26
Figure 15 – System Level Study for COP Improvement. 27
Figure 16 – HX Pass Configurations. 28
Figure 17 – DP III: Optimization Results. 29
Figure 18 – DP III: System Level Analysis. 30
Figure 19 – Charge Optimization: a.) Condenser; b.) Evaporator. 30
Figure 20 – Alternative Offset-Strip Fin HX. 31
Figure 21 – Air Flow Streamlines around Alternative Offset-Strip Fin HX. 31
Figure 22 – Pipe-Attached Fin HX. 33
Figure 23 – Air Flow Streamlines around Pipe-Attached Fin HX. 33
Figure 24 – Airfoil (top), Droplet (middle) and Circle (bottom) Cross-Section and Flow Structure. 34
Figure 25 – Droplet Shape Pipe Styles: Asymmetric (top) and Symmetric (bottom). 34
Figure 26 – EHD-Enhanced Mini HX Simulation Schematic. 35
Figure 27 – Velocity Vector Field at Simulation Domain Center. 36
Figure 28 – Schematic Diagram of Airside Test Facility. 38
Figure 29 – Cold Water Loop (top), Glycol Water Loop (middle), Hot Water Loop (bottom) Schematic Diagram. 39
Figure 30 – Water/Brines System Loop Schematic Diagram. 39
Figure 31 – Refrigerant System with Oil Loop Schematic Diagram. 40
Figure 32 – Refrigerant System without Oil Schematic Diagram. 40
Figure 33 – NURBS Tube Shape HX. 41
Figure 34 – 3D printed NURBS Shape Tube HX. 42
Figure 35 – a.) NTHX-001 Wilson Plot; b.) Air HTC 43
Figure 36 – NTHX-001 Capacity 44
Figure 37 – NTHX-001 Airside Pressure Drop. 44
Figure 38 – NTHX-001 Energy Balance. 45
Figure 39 - BTHX-001 45
Figure 40 – BTHX-001 Capacity. 46
Figure 41 – BTHX-001 Airside Pressure Drop 46
Figure 42 – BTHX-001 Energy Balance 47
Figure 43 – a.) BTHX-001 Wilson Plot; b.) Air HTC 47
Figure 44 – Vertical Orientation Energy Balance. 49
Figure 45 – Vertical Orientation Capacity. 49

Figure 46 – Vertical Orientation Sensible Heat (Wet Condition). 50
Figure 47 – Verical Orientation Latent Heat (Wet Condition). 50
Figure 48 – Vertical Orientation Sensible Heat Ratio (Wet Condition). 51
Figure 49 – Vertical Orientation Airside Pressure Drop. 51
Figure 50 – Horizontal Orientation Capacity. 52
Figure 51 – Horizontal Orientation Sensible Heat (Wet Condition). 53
Figure 52 – Horizontal Orientation Latent Heat (Wet Condition). 53
Figure 53 – Horizontal Orientation Sensible Heat Ratio (Wet Condition). 54
Figure 54 – Horizontal Orientation Airside Pressure Drop Pressure. 54
Figure 55 – Experimental Validation: Capacity. 55
Figure 56 – Experimental Validation: Airside Pressure Drop. 56
Figure 57 – 10 kW HX. 56
Figure 58 – Blockage Test before Cleaning: (a) Front View; (b) Back View. 57
Figure 59 – Blockage Test after Cleaning: (a) Front View; (b) Back View. 57
Figure 60 – 10kW HX Energy Balance, Pre-Cleaning, Dry Condition. 58
Figure 61 – 10kW HX Capacity, Pre-Cleaning, Dry Condition. 59
Figure 62 – 10kW HX Airside Pressure Drop, Pre-Cleaning, Dry Condition. 59
Figure 63 – 10kW HX Energy Balance, Post-Cleaning, Dry Condition. 61
Figure 64 – 10kW HX Capacity, Post-Cleaning, Dry Condition. 61
Figure 65 – 10kW HX Airside Pressure Drop, Post-Cleaning, Dry Condition. 62
Figure 66 – Air HTC, Pre-Cleaning. 62
Figure 67 – Air HTC, Post-Cleaning. 62
Figure 68 – Airside Pressure Drop, Pre-Cleaning. 63
Figure 69 – Airside Pressure Drop, Post-Cleaning. 63
Figure 70 – 10kW HX Capacity, Experiments and Simulations Comparison. 63
Figure 71 – 10kW HX Airside Pressure Drop, Experiments and Simulations Comparison. 64
Figure 72 – 10kW HX UA Value, Experiments and Simulations Comparison. 64
Figure 73 – 10kW HX Air HTC, Experiments and Simulations Comparison. 65
Figure 74 – WTHX. 65
Figure 75 – WTHX Dimensions. 66
Figure 76 – WTHX Capacity. 66
Figure 77 – WTHX Airside Pressure Drop. 67
Figure 78 – a.) WTHX Wilson Plot; b.) Air HTC. 67
Figure 79 – BTHX Optimum Design. 75
Figure 80 – BTHX Copper Version. 76
Figure 81 – BTHX Stainless Steel Version. 76
Figure 82 – NURBS Curves generated for a given Control Polygon. 77
Figure 83 – Tube Shape Parameterization. 77

List of Tables

Table 1 – Analyses Summary. 12
Table 2 – 1.0kW Baseline MCHX. 19
Table 3 – Selected Designs. 21
Table 4 – 10kW BTHX Optimum Design. 26
Table 5 – Baseline Cycle Verification. 26
Table 6 – Two-Phase HX's Operating Conditions. 27
Table 7 – Alternative Offset-Strip Fin HX LHS Design Parameters. 32
Table 8 – Alternative Offset-Strip Fin HX LHS Results. 32
Table 9 – Airfoil, Droplet, and Circle Cross-Section HX Results Comparison. 34
Table 10 – Droplet Shape Pipe Simulation Results Comparison. 35
Table 11 – EHD-Enhanced Mini HX Box-Behnken Design Parameters and Results. 36
Table 12 – Experimental Specifications. 37
Table 13 – Test Facility Specifications 38
Table 14 – NTHX Design for Manufacture. 41
Table 15 – Wet Condition Test Matrix. 48
Table 16 – 1.0kW Air-to-Water HX Validation Test Results. 55
Table 17 – Pre-Cleaning Dry Condition Test Matrix 57
Table 18 – Post-Cleaning Dry Condition Test Matrix. 60
Table 19 – Instrument Systematic Error. 68
Table 20 – CFD-Based Correlations (taken from D. Bacellar Ph.D. Dissertation Defense). 69
Table 21 – Project Timeline. 74
Table 22 – BTHX Designs being Manufactured. 75
Table 23 – Dry Conditions 78
Table 24 – Wet Conditions, Inlet RH=51% 79
Table 25 – Wet Conditions, Inlet RH=70% 80

Acknowledgement

"This material is based upon work supported by the United States Department of Energy under Award Number DE-EE0006114."

Disclaimer

"This report was prepared as an account of work sponsored by an agency of the United States Government. Neither the United States Government nor any agency thereof, nor any of their employees, makes any warranty, express or implied, or assumes any legal liability or responsibility for the accuracy, completeness, or usefulness of any information, apparatus, product, or process disclosed, or represents that its use would not infringe privately owned rights. Reference herein to any specific commercial product, process, or service by trade name, trademark, manufacturer, or otherwise does not necessarily constitute or imply its endorsement, recommendation, or favoring by the United States Government or any agency thereof. The views and opinions of authors expressed herein do not necessarily state or reflect those of the United States Government or any agency thereof."

Team Members

Project Team

University of Maryland, College Park (UMCP)

Reinhard Radermacher, PI; Minta Martin Professor of Engineering and Director, Center for Environmental Energy Engineering (CEEE)

Vikrant Aute, Co-PI; Associate Research Scientist and Director, Modeling & Optimization Consortium (MOC), CEEE

Yunho Hwang, Co-PI; Research Professor and Assistant Director, Energy Efficiency and Heat Pumps (EEHP), CEEE

Daniel Bacellar; Graduate Research Assistant, MOC, CEEE

Zhiwei Huang; Graduate Research Assistant, EEHP, CEEE

Jiazhen Ling; Research Assistant Professor, EEHP & MOC, CEEE

Jan Muehlbauer; Faculty Specialist, EEHP, CEEE

James Tancabel; Graduate Research Assistant, MOC, CEEE

Oak Ridge National Laboratory (ORNL)

Omar Abdelaziz, Co-PI; Group Leader and Senior R&D Staff, Building Equipment Research Group

Patrick Geoghegan; R&D Staff, Building Equipment Research Group

Vishaldeep Sharma; R&D Staff, Building Equipment Research Group

Mingkan Zhang; Postdoctoral Research Associate, Building Equipment Research Group

Frederick A. List III; Group Member, Deposition Science & Technology – Metal Additive Manufacturing

Keith Carver; Tech Intern, Metal Additive Manufacturing

Industry Partners

Luvata

Mike Heidenreich

Russ Cude

Randy Weaver

International Copper Association (ICA)

John Black

Hal Stillman

Heat Transfer Technologies (HTT)

Yoram Shabtay

Wieland

Steffen Rieger

Burr Oak Tool

Roger Tetzloff

[This page intentionally left blank]

Executive Summary

Air-to-refrigerant Heat eXchangers (HX) are an essential component of Heating, Ventilation, Air-Conditioning, and Refrigeration (HVAC&R) systems, serving as the main heat transfer component. The major limiting factor to HX performance is the large airside thermal resistance. Recent literature aims at improving heat transfer performance by utilizing enhancement methods such as fins and small tube diameters; this has lead to almost exhaustive research on the microchannel HX (MCHX). The objective of this project is to develop a miniaturized air-to-refrigerant HX with at least 20% reduction in volume, material volume, and approach temperature compared to current state-of-the-art multiport flat tube designs and also be capable of production within five years. Moreover, the proposed HX's are expected to have good water drainage and should succeed in both evaporator and condenser applications.

The project leveraged Parallel-Parametrized Computational Fluid Dynamics (PPCFD) and Approximation-Assisted Optimization (AAO) techniques to perform multi-scale analysis and shape optimization with the intent of developing novel HX designs whose thermal-hydraulic performance exceeds that of state-of-the-art MCHX. Nine heat exchanger geometries were initially chosen for detailed analysis, selected from 35+ geometries which were identified in previous work at the University of Maryland, College Park.

The newly developed optimization framework was exercised for three design optimization problems: (DP I) 1.0kW radiator, (DP II) 10kW radiator and (DP III) 10kW two-phase HX.

- DP I consisted of the design and optimization of 1.0kW air-to-water HX's which exceeded the project requirements of 20% volume/material reduction and 20% better performance. Two prototypes for the 1.0kW HX were prototyped, tested and validated using newly-designed airside and refrigerant side test facilities.
- DP II, a scaled version DP I for 10kW air-to-water HX applications, also yielded optimized HX designs which met project requirements. Attempts to prototype a 10kW have presented unique manufacturing challenges, especially regarding tube blockages and structural stability.
- DP III comprised optimizing two-phase HX's for a 3.0Ton capacity in a heat pump / air-conditioning unit for cooling mode application using R410A as the working fluid. The HX's theoretically address the project requirements. System-level analysis showed the HX's achieved up to 15% improvement in COP while also reducing overall unit charge by 30-40%.

The project methodology was capable of developing HX's which can outperform current state-of-the-art MCHX by at least 20% reduction in volume, material volume, and approach temperature. Additionally, the capability for optimization using refrigerant charge as an objective function was developed. The five-year manufacturing feasibility of the proposed HX's was shown to have a good outlook. Successful prototyping through both conventional manufacturing methods and next generation methods such as additive manufacturing was achieved.

1 Introduction

The Center for Environmental Energy Engineering (CEEE) at the University of Maryland, College Park, is a leading research and educational institute in the field of environmentally responsible, economically feasible integrated energy conversion systems. CEEE's vision is to excel in research and development of energy conversion systems that are highly energy-efficient and cost-effective, while also using the least amount of material and having minimal environmental impact.

CEEE is organized into three consortia based on their individual research pursuits:

- Energy Efficiency and Heat Pumps (EEHP)
- Advanced Heat Exchangers and Process Intensification (AHXPI)
- Modeling and Optimization (MO)

CEEE conducts extensive experimental and theoretical research, the results of which are made available in part through user-friendly, verified, and validated software for the design and analysis of energy conversion systems. The software is capable of systematically searching for lowest-cost systems and components that are highly energy-efficient and/or require the least amount of material. Through its graduate education program, CEEE educates the newest generation of creative, team-oriented engineering professionals who will be future leaders in their field.

1.1 Project Objective and Background

The objective of this project is to develop miniaturized air-to-refrigerant heat exchangers (HX) with at least 20% reductions in volume, material volume, and approach temperature as compared to current multiport flat tube designs. Further, the designs should be production-capable within five years. While the proposed technology allows for more performance improvements, these need to be balanced with design robustness regarding clogging flow channels with compressor oil or debris on the airside. Thus, for the first generation of heat exchangers, performance estimates have been made on the conservative side. The proposed heat exchangers are expected to have good water drainage and should succeed as both an evaporator and condenser.

A novel miniaturized air-to-refrigerant HX is obtained by eliminating all tubes of a flat tube multiport heat exchanger while the refrigerant flows through the fins. Because of small refrigerant flow channel dimensions, the overall HX becomes very compact. In addition, through extensive use of primary surface area, the heat transfer is considerably improved. Refrigerant and airside pressure drops are minimized by using many parallel flow channels. The concept was successfully demonstrated in a 100W laboratory sample.

1.2 Summary of Project Achievements

This report summarizes the overall analytical and experimental results from the project. The highlights of project achievements are:

- Succesfully designed and optimized 1.0kW air-to-water HX's exceeding the project requirements of 20% volume/material reduction and 20% better performance;
- Successfully designed and built a modular airside test facility and a refrigerant side test facility, the latter capable of utilizing three different refrigerant loops;
- Succesfully prototyped, tested, and validated two prototypes for the 1.0kW air-to-water application;
- Designed and optimized 10kW air-to-water HX's;
    - 10kW prototype presented challenges including tube blockage and structural stability;
- Designed and optimized two-phase HX's for a 3.0Ton SEER 16 unit;

- HX's theoretically address all the project requirements mentioned above;
- System-level analysis shows the HX's achieve up to 15% improvement in COP while reducing charge by 30% to 40%;
- Capability for optimization using charge as an objective function.

2 Heat Exchanger Analysis

Table 1 presents a summary of all analyses performed in this study.

Table 1 – Analyses Summary.

HX	Airside Characterization					1.0kW SP			10kW SP			10-13kW TP		
	IA	PPCFD	UA	MM	CORR	AAO	PT	VAL	AAO	PT	VAL	AAO	PT	VAL
RTHX (St)	X	X	X	X	X	X	X	X	X	X	O	X	X	→
RTHX (In)	X	X	X	X	X	X	→					X	X	→
WFHX (St)	X	X	X	X	X	→								
NTHX (St)	X	X	X	X	N/A	X	X	X	→					
WTHX (In)	X	X	X	X	X	X	→							
VGHX	O	→												
NGHX13*	X	X	X	X	N/A	X	O	→						
HCHX**	X	O	→											
RTHX (Ch)	X	D												
RTHX (Mt)	X	X	D											
FTHX (St)	X	X	X	X	X	X	D							
FTHX (In)	X	D												
AFHX	X	X	X	X	N/A	X	D							
SFHX (1b)	X	X	X	X	N/A	X	D							
SFHX (2b)	X	X	X	X	N/A	X	D							

Legend:

RTHX	Round finless tubes	**St**	Staggered	**IA**	Initial Analysis	**X**	Accomplished
FTHX	Flat fin and tubes	**In**	In-line	**PPCFD**	Parallel Parameterized CFD	**O**	In process
WFHX	Wavy fin and tubes	**Ch**	Chevron	**UA**	Uncertainty Analysis	**→**	Path Forward
NTHX	NURBS tubes	**Mt**	Matrix	**MM**	Metamodeling	**D**	Discontinued
WTHX	Webbed NURBS tubes	**1b**	1 slab	**CORR**	Correlation Development	**N/A**	Not Applicable
VGHX	Variable Geometry	**2b**	2 slabs	**AAO**	Approximated Assisted Optimization		
AFHX	Airfoil tubes			**PT**	Prototype		
SFHX	Slanted finless microchannels			**VAL**	Validation		
NGHX	Webbed round tubes						
HCHX	Honeycomb tubes						

2.1 CFD Modeling and Simulation

2.1.1 Airside Modeling

The streamwise periodic flow numerical method introduced by Patankar [1] is extensively used in Computational Fluid Dynamics (CFD) for HX problems. CFD is now a required tool in such applications, in spite the criticism regarding the numerical uncertainty associated with it. Shah [2] argued the uncertainties related to CFD simulations, in many cases, can be comparable to the performance improvement obtained. For this reason, CFD uncertainty analysis and validations must be carried out.

2.1.2 CFD Modeling and Simulation

The method proposed by Pantakar [1] aims at reducing the computational cost by adequately reducing the computational domain without losing physical meaning. Typically, the end-effects can be neglected and the thermal-hydraulic characteristics of a surface can be determined by a segment of the HX where the lower, upper and longitudinal boundaries are assumed periodic or symmetric. In the literature, numerical analysis of finless surfaces commonly employs two-dimensional computational domains [3], [4], [5], [6]; however, finned computational domains must be three-dimensional.

When using CFD for heat transfer applications, three fundamental set of equations must be solved: continuity (Eq. (1)), momentum (Navier-Stokes) (Eq. (2)), and energy (Eq. (3)) The assumptions used in this work include: a) steady-state flow; b) non-existent energy and mass sources nor external forces; c) negligible gravitational effects; d) pressure work and kinetic energy are negligible. The physical model is then reduced to a convection-diffusion problem with no external components. The resulting governing equations are described below:

$$\nabla\left(\rho\tilde{u}\right)=0 \tag{1}$$

$$\left(\tilde{u}\cdot\nabla\right)\left(\rho\tilde{u}\right)=-\nabla P+\mu\nabla^{2}\tilde{u} \tag{2}$$

$$\tilde{u}\cdot\nabla\left(\rho c_{p}T\right)-k\cdot\nabla^{2}T=0 \tag{3}$$

There are three important aspects regarding this type of CFD simulation that are seldom discussed in detail including: (1) near wall meshing, (2) flow regime models, and (3) thermophysical properties.

Thermal diffusion (Eq. (4)) and viscous resistance (Eq. (5)) within the boundary layer are functions of the temperature and velocity gradient at the surface, respectively). One must consider a much finer mesh near the wall in order to better capture the boundary layer physics.

$$h_{x}\left(T_{\infty}-T_{w}\right)=-k\frac{\partial T}{\partial y}\Bigg)_{w} \tag{4}$$

$$C_{f}=\frac{\tau_{w}}{\frac{1}{2}\rho u_{\infty}}=\frac{1}{\frac{1}{2}\rho u_{\infty}}\left(\alpha+\varepsilon\right)\frac{\partial\bar{u}}{\partial r}\Bigg)_{w} \tag{5}$$

Hilbert et al. [5] illustrated their computational domain with an unstructured pave mesh with uniform element size, however no refinement near the tube wall. In this work, we consider a two-dimensional computational domain (Figure 1) with pave meshing scheme as well; however, the near wall region mesh is a fine map scheme with growing layers at a ratio of at most 1.2.

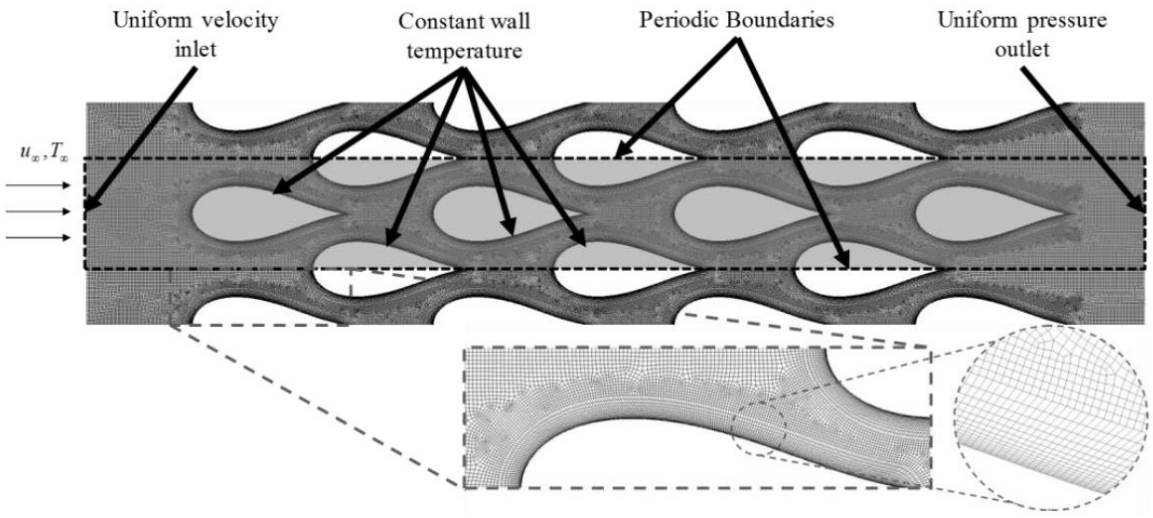

Figure 1 – Typical CFD Two-dimensional Computational Domain.

For the two-dimensional computational domain, both triangle and quadrilateral mesh schemes were used, depending upon the geometry.

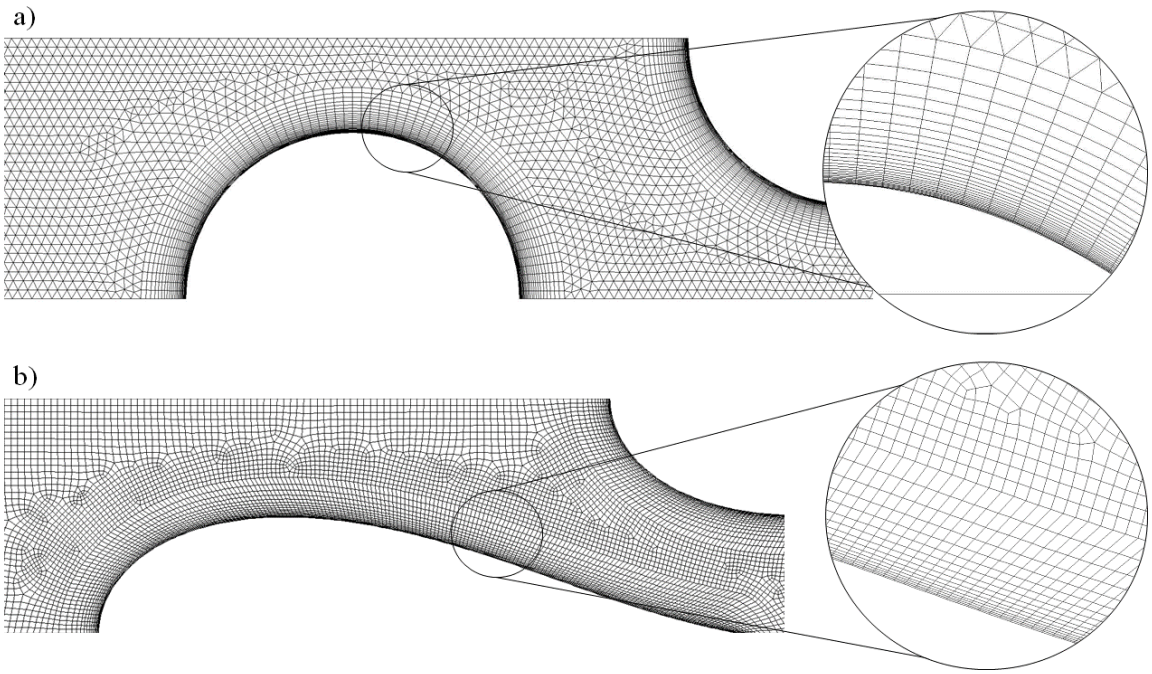

Figure 2 – Two-dimensional Computational Domain Mesh Schemes:
a) Triangle; b) Quadrilateral.

Hexahedron elements using Cooper scheme is the most efficient way of modeling 3-D computational domain. The periodicity requires mesh link between periodic boundaries, and Cooper scheme becomes convenient since it uses a source face to project the mesh onto parallel faces.

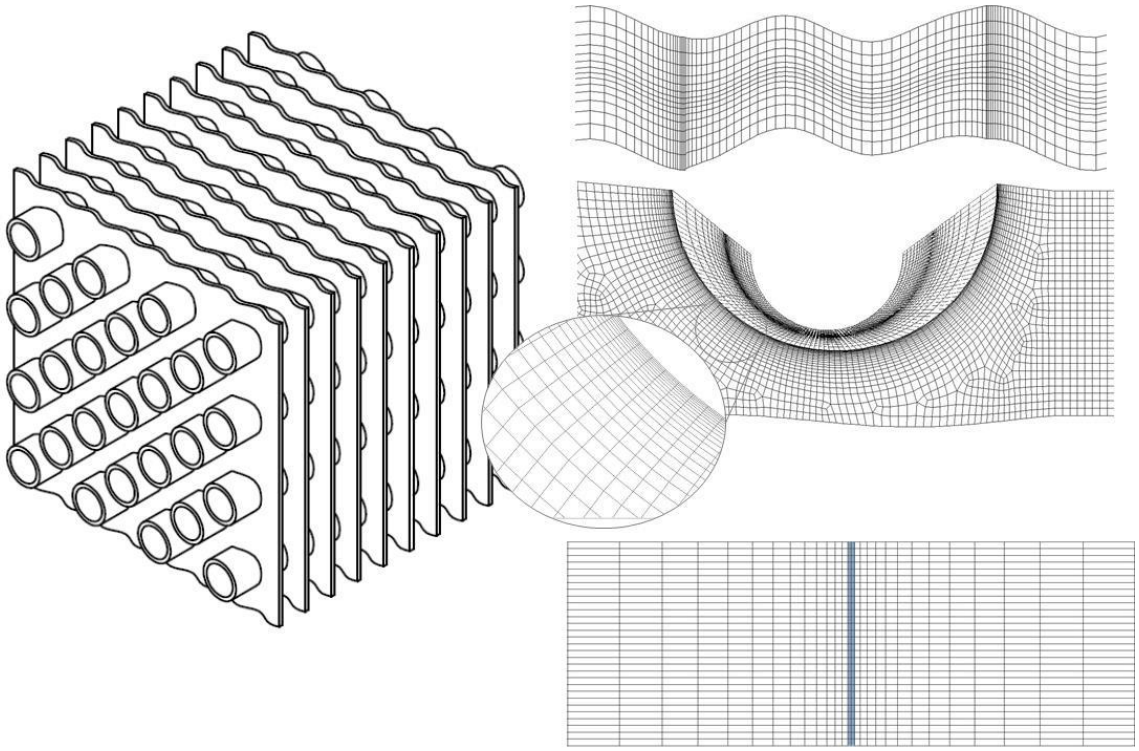

Figure 3 – Typical CFD Three-dimensional Computational Domain.

Flow regimes models are a very debatable issue. For instance, Hilbert et al. [5] and Ranut et al. [6] used laminar flow with the argument that the Reynolds number was low (~160). There are two considerations to their statement. One, they defined the Reynolds number based on the tube vertical spacing, which is fixed in their model, although the most adequate would be using the surface hydraulic diameter, which can vary for different shapes. Second, the same Reynolds number for different surfaces can result in different flow regimes; i.e., eddies can be developed in the inevitable flow separation, generating wakes which affects the flow regime of subsequent tube banks, even if the first tube has a laminar flow. Although turbulence models are known to overpredict heat transfer and friction for truly laminar flows, they can better solve a broader range of problems. This is preferable when one has to simulate a large number of samples using common CFD settings. There are many turbulence models available in commercial CFD packages. The two-equation k-ε realizable (RKE) model [7] has proven to be very robust. The RKE ensures the solution obeys the non-negativity of turbulent normal stress [8]; thus, the solutions are realistic from the physical viewpoint when converged. Additionally, the authors have observed a higher rate of convergence when using RKE for a large number of CFD simulations compared to other models, including laminar.

The thermophysical properties also have an impact to the outcomes of the CFD simulations. In many heat transfer applications, the fluid flow is significantly subsonic ($Ma << 0.3$), which characterizes as incompressible flow. Many authors simplify the problem by using constant properties [5], [6]. The temperature, however, may have a significant impact, particularly on density, conductivity and viscosity. There are consequences on both momentum and heat transfer. As the airstream gets warmer, the constant density assumption leads to an under prediction of the accelerating airflow; constant conductivity underpredicts the thermal diffusion within the boundary layer; constant viscosity overpredicts the shear stress at the surface. Therefore, the ideal-gas model is reasonable for density, whereas the other thermophysical properties can easily be estimated with polynomial curve fits as functions of temperature (Figure 4).

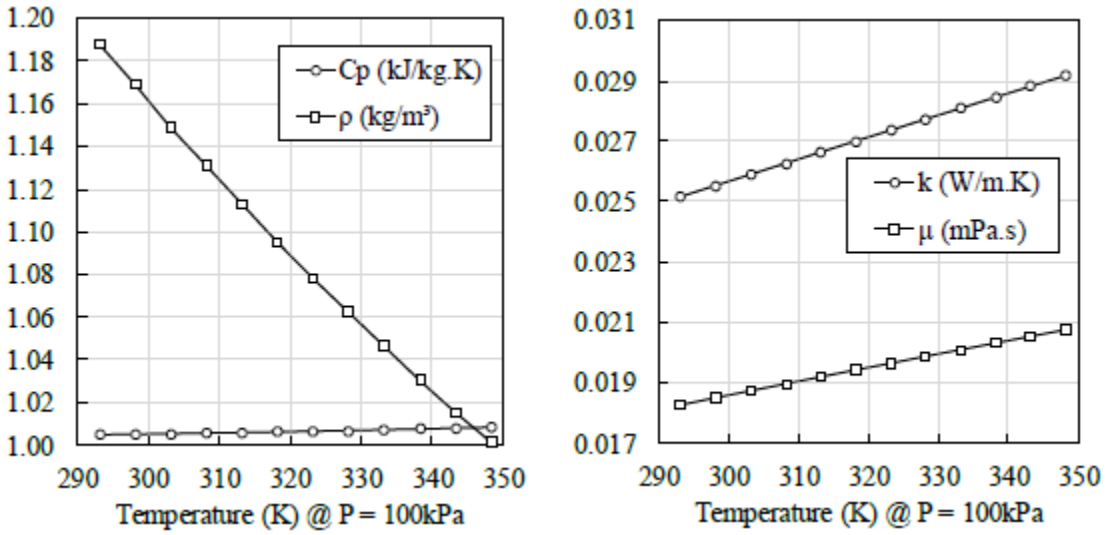

Figure 4 – Dry Air Properties as Funcitons of Temperature.

Finally, the simulation convergence criteria are set to a maximum residual of 10E-5 for momentum and continuity, 10E-6 for energy and 10E-3 (default) for turbulence. If the simulation does not meet the criteria, however it stabilizes into a solution, we assume that if the standard deviation of the last 100 iterations is less than 0.5% of the average of those same 100 iterations, then it is converged.

2.1.3 CFD Data Reduction

For this type of problem, it is convenient to define uniform wall temperature (Figure 1), allowing for easy calculation of airside heat transfer coefficient from the UA – Log Mean Temperature Difference (UA-LMTD) method (Eq. (6) and (7)). When studying surface performance in particular, it is also of interest to determine the non-dimensional heat transfer (Colburn j factor) as per Eq. (8).

$$\dot{Q} = \dot{m}\bar{c}_p\left(T_o - T_i\right) = \eta_o h A_o \Delta T_{lm} \tag{6}$$

$$\eta_o h = \frac{\dot{m}\bar{c}_p}{A_o}\cdot\frac{T_o - T_i}{\Delta T_{lm}} = \frac{\dot{m}\bar{c}_p}{A_o}\cdot\frac{T_o - T_i}{\dfrac{\left[\left(T_w - T_i\right) - \left(T_w - T_o\right)\right]}{\ln\left[\left(T_w - T_i\right) - \left(T_w - T_o\right)\right]}} = \frac{\dot{m}\bar{c}_p}{A_o}\cdot\ln\left[\frac{\left(T_w - T_i\right)}{\left(T_w - T_o\right)}\right] \tag{7}$$

$$j = \frac{h}{\bar{\rho}u_c\bar{c}_p}\cdot \mathrm{Pr}^{2/3} \tag{8}$$

For finless designs, fin effectiveness $\left(\eta_o\right)$ is logically equal to unity. However, when that is not the case, the fin efficiency / effectiveness and heat transfer coefficient are calculated using the Schmidt [9] approach (Eq. (9) – (14)) and iteratively using Newton-Raphson method [10] (Eq. (15) and (16)).

$$\eta_o = 1 - \frac{A_{fr}}{A_o}\left(1 - \eta\right) \tag{9}$$

$$\eta = \frac{\tanh\left(0.5 m D_o \phi\right)}{0.5 m D_o \phi} \tag{10}$$

$$m = \left(\frac{h}{k_f \delta_f} \right)^{1/2} \tag{11}$$

$$\phi = \left(R_{eq} - 1 \right) \left(1 + 0.35 \ln \left[R_{eq} \right] \right) \tag{12}$$

$$R_{eq} = 1.27 \frac{P_t}{D_o} \left(\frac{2X_L}{P_t} - 0.3 \right)^{1/2} \tag{13}$$

$$X_L = \frac{1}{2} \left(\frac{P_t^2}{4} + P_l^2 \right)^{1/2} \tag{14}$$

$$h^n = h^{n-1} - \frac{\beta\left(h^{n-1}\right)}{\beta'\left(h^{n-1}\right)} \tag{15}$$

$$\beta'\left(h^{n-1}\right) = \left(UA\right)_o - \left[1 - \frac{A_{fr}}{A_o} \left(1 - \frac{\tanh\left(\frac{1}{2} D_o \phi \left(\frac{2h^{n-1}}{k_f \delta_f} \right)^{1/2} \right)}{\frac{1}{2} D_o \phi \left(\frac{2h^{n-1}}{k_f \delta_f} \right)^{1/2}} \right) \right] \cdot h^{n-1} \tag{16}$$

For pressure drop, it is convenient to set the outlet boundary at uniform atmospheric pressure (0.0 gauge). Additionally, the dynamic pressure difference between inlet and outlet can be assumed insignificant compared to the static pressure difference. Lastly, the buoyancy term is also negligible for gases. Therefore, the pressure drop is simply computed according to Eq. (17). Similarly, the non-dimensional pressure drop neglecting local effects is computed using Eq. (18).

$$\Delta P = P_{in} - P_{out} + \frac{1}{2} \rho_{in} u_{in}^2 \left(1 - \frac{\rho_{out}}{\rho_{in}} \right) \tag{17}$$

$$f = \frac{\Delta P}{\bar{\rho} u_c^2} \cdot \frac{D_{hs}}{2d} \tag{18}$$

2.1.4 CFD Grid Uncertainty Analysis

One standard approach to evaluate CFD model uncertainty is the 5-step Grid Convergence Index (GCI) method [11], [12], [13]. Grid Convergence Index (GCI) [13] is a formal methodology based on Richardson Extrapolation used to estimate the grid convergence error of a metric of interest (φ) [14].

Step 1: Define the average element length of the grid for two-dimensional (Eq. (19)) and three-dimensional (Eq. (20)) computational domains, respectively.

$$\delta_{2D} = \left(\frac{\sum \Delta A_i}{N} \right)^{1/2} \tag{19}$$

$$\delta_{3D} = \left[\frac{\sum \Delta V_i}{N} \right]^{1/3} \tag{20}$$

Step 2: Select at least three grid resolutions (Eq. (21)) where the element size ratio between subsequent grid resolutions is greater than or equal to 1.3. The procedure is simplified when using constant refinement ratio (r) since it eliminates the iterative calculations [11].

$$r_{i+1,i} = \frac{\delta_{i+1,coarse}}{\delta_{i,\,fine}} \geq 1.3 \tag{21}$$

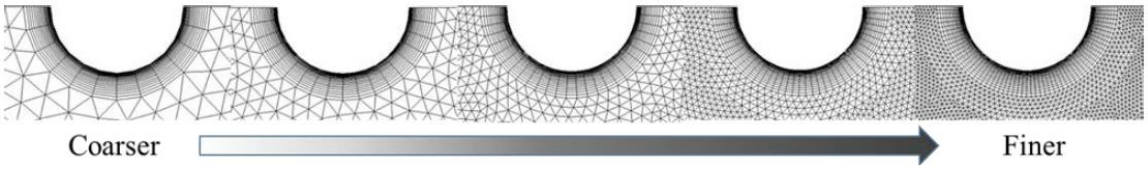

Figure 5 – Sequentially Increasing Grid Resolutions.

Step 3: Calculate the observed order of accuracy (p*) (Eq. (22)). When the observed order of accuracy deviates more than 10% from the formal spatial discretization order of accuracy (p), then the effective value (p**) (Eq. (25)) must be bounded by a minimum of 0.5 and the formal value [15].

$$p^* = \left(\frac{1}{\ln\left[r_{21}\right]} \right) \left(\ln\left| \frac{\varepsilon_{32}}{\varepsilon_{21}} \right| + \ln\left[\frac{r_{21}^p - s}{r_{32}^p - s} \right] \right) \tag{22}$$

$$s = \frac{\varepsilon_{21} / \varepsilon_{32}}{\left| \varepsilon_{21} / \varepsilon_{32} \right|} \tag{23}$$

$$\varepsilon_{21} = \varphi_2 - \varphi_1 \tag{24}$$

$$p^{**} = \min\left\{ \max\left[0.5, p\right], p^* \right\} \tag{25}$$

Step 4: Calculate the extrapolated values (Eq. (26)).

$$\varphi_{ext}^{21} = \frac{r_{21}^p \varphi_1 - \varphi_2}{\left| r_{21}^p - 1 \right|} \tag{26}$$

Step 5: Calculate and report the estimated extrapolation error (Eq. (27)) and the (GCI) (Eq. (28)).

$$e_{ext}^{21} = \left| \frac{\varphi_{ext}^{21} - \varphi_1}{\varphi_{ext}^{21}} \right| \tag{27}$$

$$GCI_{\,fine}^{21} = \frac{F_s \cdot e_a^{21}}{r_{21}^{p^{**}} - 1} \tag{28}$$

If p^* deviates more than 10% from p, then the factor of safety (F_s) must be set to 3.0 [13], otherwise a value of 1.25 is acceptable [13].

Bacellar et al. [16] proposed a method to quantify the CFD uncertainty of an entire design space. The premise is that designs at the boundaries of the design space are assumed to have fundamentally larger uncertainties than any other sample. The reason for this is that the combinations of lower and upper bounds yield the most skewed computational domains, thus having a higher potential for poorer mesh elements in terms of size and aspect ratios. For every surface investigated, the GCI method is employed for the 2^n samples represented by all variable combinations of 0's and 1's for an n-dimensional design space (e.g. n = 5, 2^5 = 32 samples).

2.2 1.0kW Radiator Optimization Results

Figure 6 presents the optimization map for all analyzed geometries according to airside pressure drop, HX volume, face area, and material volume compared to the baseline microchannel HX (Table 2).

Table 2 – 1.0kW Baseline MCHX.

Metric	Unit	Value
Air flow rate	m^3/s	0.03
Air inlet temperature	K	300
Water flow rate	g/s	25
Water inlet temperature	K	347.5
Heat load	W	1053
Pumping power	W	2.35
Air pressure drop	Pa	78
Air heat transfer coefficient	W/m^2K	144
Airside thermal resistance	K/W	0.022

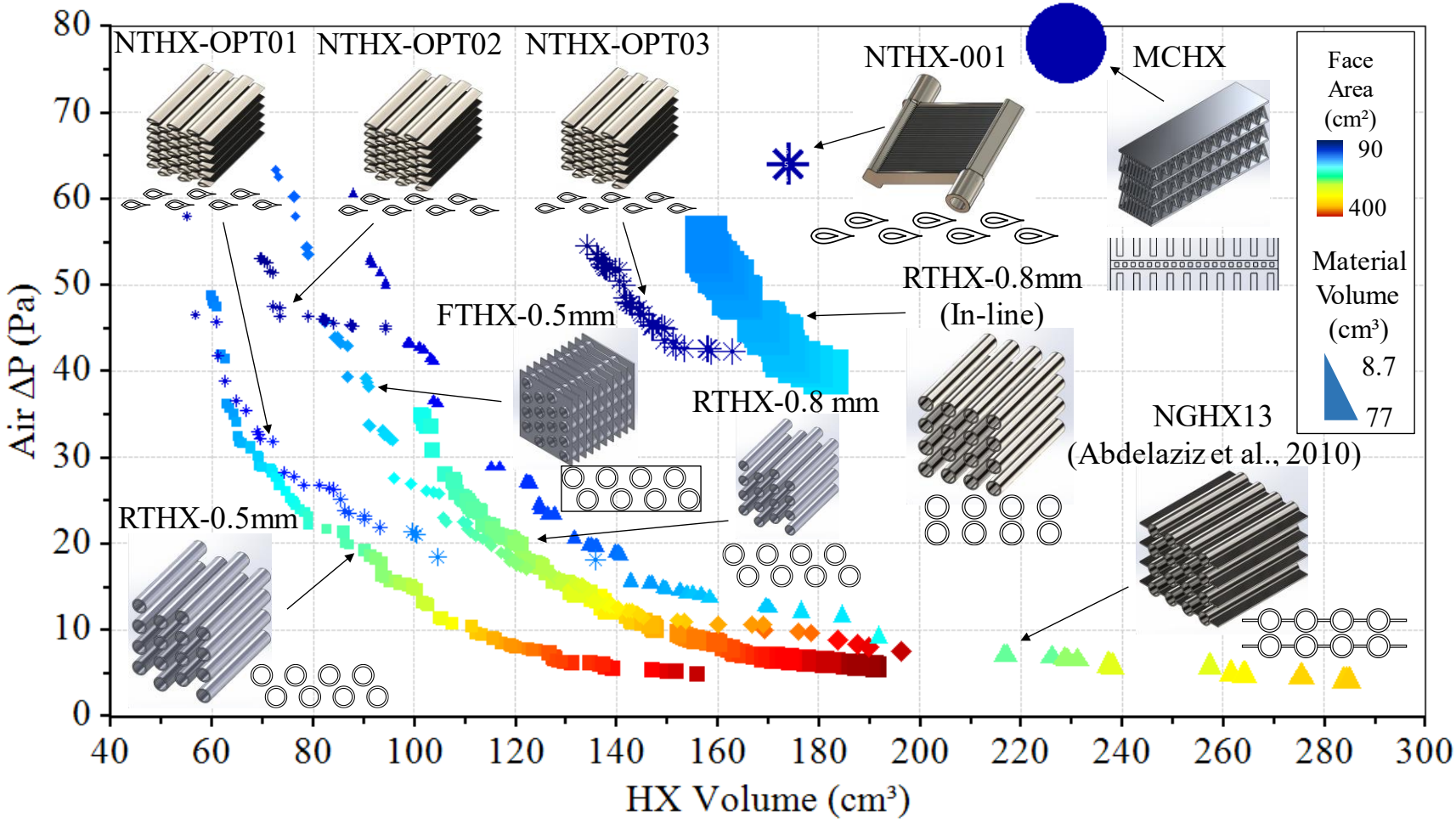

Figure 6 – Radiator Optimum Designs: Air DP vs. Heat Exchanger Volume.

From the map presented in Figure 6, four designs were chosen for prototyping (Table 3): (1) round bare tube HX with 0.8mm OD design 1 (BTHX Cu) ; (2) round bare tube HX with 0.8mm OD design 2 (BTHX SS); (3) NURBS-shape tube HX (NTHX); (4) Webbed-tube HX (NGHX13).

Table 3 – Selected Designs.

Metric	Unit	Baseline	BTHX Cu	BTHX SS	NTHX-001	NGHX13
Capacity	W	1109	1005	1005	1072	1013
Volume	cm^3	229	107	107	174	88
Face Area	m^2	0.010	0.023	0.023	0.010	0.0106
Depth	m	0.0230	0.0044	0.0044	0.0174	0.008
Height	m	0.054	0.15021	0.15021	0.0999	0.15119
Length	m	0.19	0.152	0.152	0.1001	0.07011
Material Volume	cm^3	77	15.9	15.9	46.8	10.90
Velocity	m/s	2.94	1.31	1.31	3	2.83
Air HTC	W/m^2K	144	309	309	200	140
Air DP	Pa	78	28	28	64	60.6
ΔT	K	50	42	42	50	50
Q"	kW/m^2	109	44	44	102	96
Q"'	MW/m^3	4.8	10.1	10.1	5.9	11.5

2.2.1 Prototypes and Experimental Validations

The proof-of-concepts RTHX-001 and NTHX-001 were prototyped and tested in the wind tunnel facility built in the University of Maryland laboratory. Details on the facility, data acquisition uncertainty analysis and details on the test matrices are presented in Chapter 3 of this manuscript. Two versions of the RTHX-001 concept (Figure 7 and Figure 8) were fabricated; one using stainless steel tubes brazed to a stainless steel header, the second using copper tubes and headers. The first was successfully tested and validated. The NTHX-001 prototype (Figure 9 and Figure 10) was fabricated using a metal additive manufacturing technique. The prototype is a single piece component printed in Titanium grade 5.

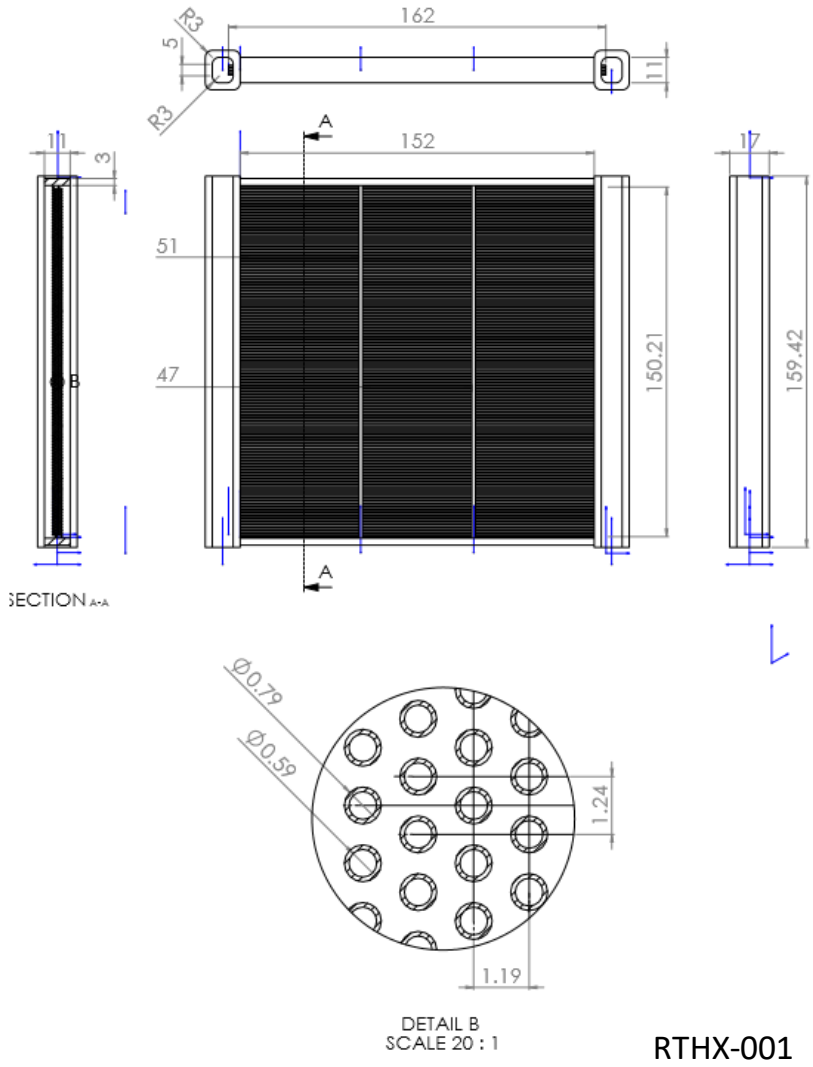

Figure 7 – RTHX-001 Prototype Drawing.

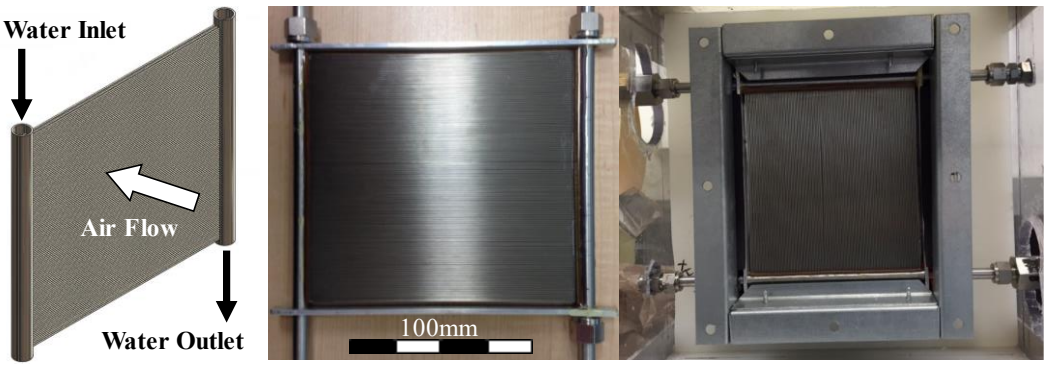

Figure 8 – Stainless Steel RTHX-001 Sample Images.

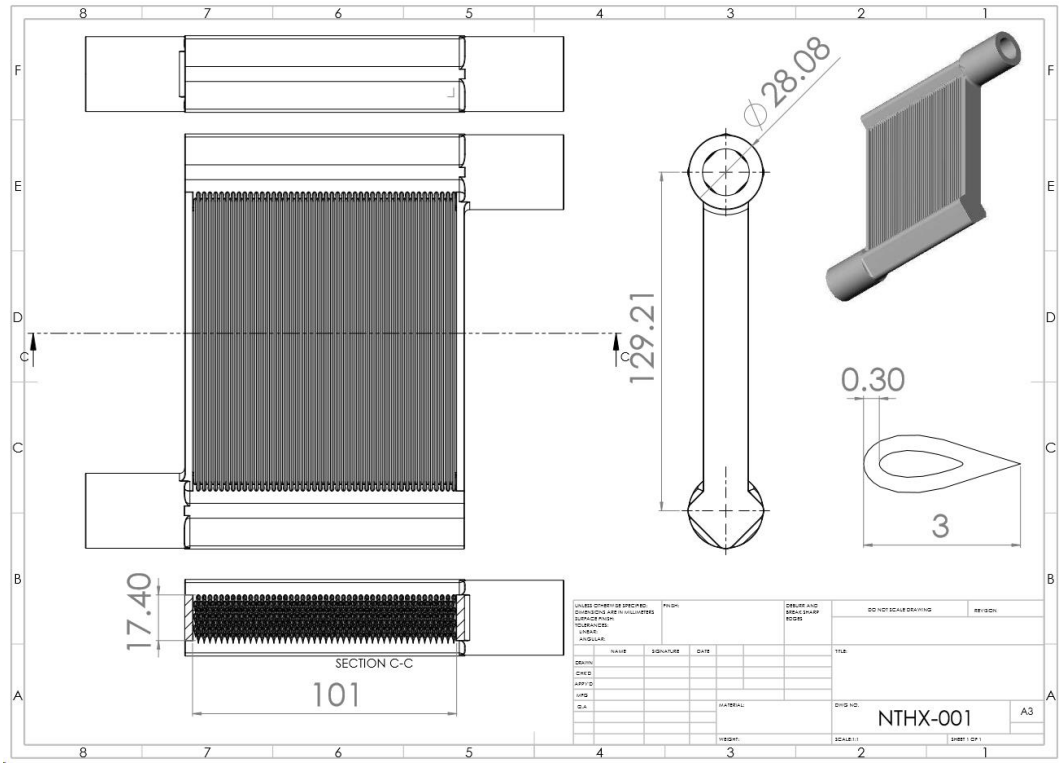

Figure 9 – NTHX-001 Prototype Drawing.

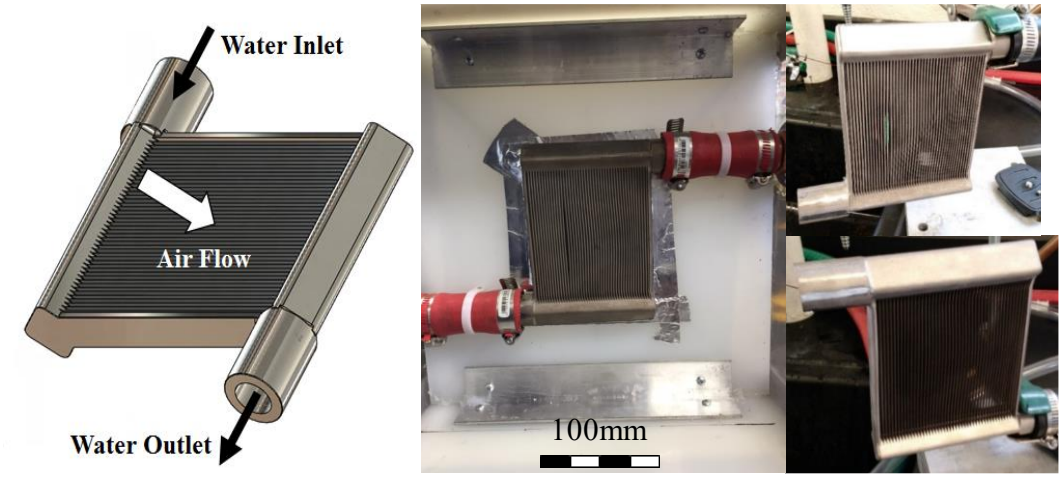

Figure 10 – NTHX-001 Sample Images.

Both prototypes were tested for 5 air flow rates and 3 water flow rates, i.e., 15 operating conditions. The inlet approach temperature was held constant at 25K, which corresponds to 50% of the design approach temperature. This results in lower capacities (<1.0kW). The average experimental capacities were compared to a HX simulation in CoilDesigner® [17], agreeing within 5% (Figure 11). The experimental data was reduced using Wilson plot method. Heat transfer coefficients obtained matched simulations within 10%, while the pressure drop matched simulations within 20% (Figure 12 and Figure 13). Pressure drop had larger differences for the RTHX-001 surface. This is likely due to the selected turbulence model overpredicting the friction resistance. For the NTHX-001, the good agreement to the pressure drop may have been a combination of factors. For example, the CFD models could have overpredicted the pressure

drop, as was the case with RTHX-001. Also, an inherited aspect of the printing process is higher surface roughness, which could have balanced out a numerical overprediction. Nevertheless, the results are encouraging and satisfactory from a validation viewpoint.

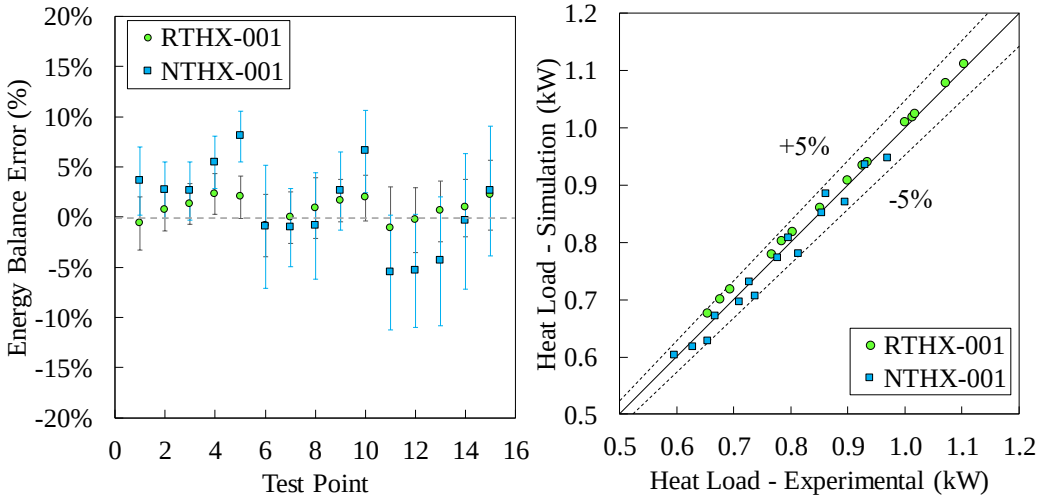

Figure 11 – Experimental Validation: Energy Balance and Overall Capacity.

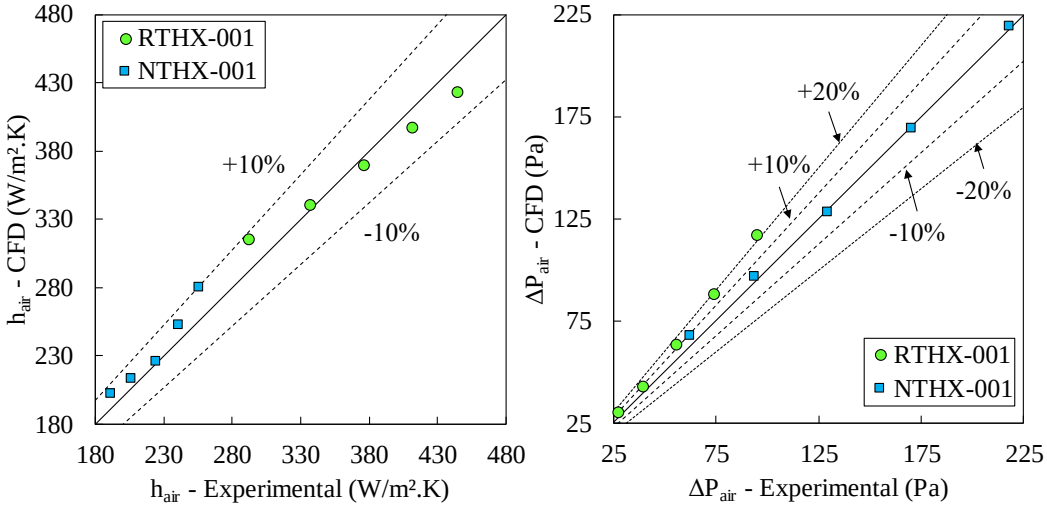

Figure 12 – Experimental Validation: Airside Heat Transfer Coefficient and Pressure Drop.

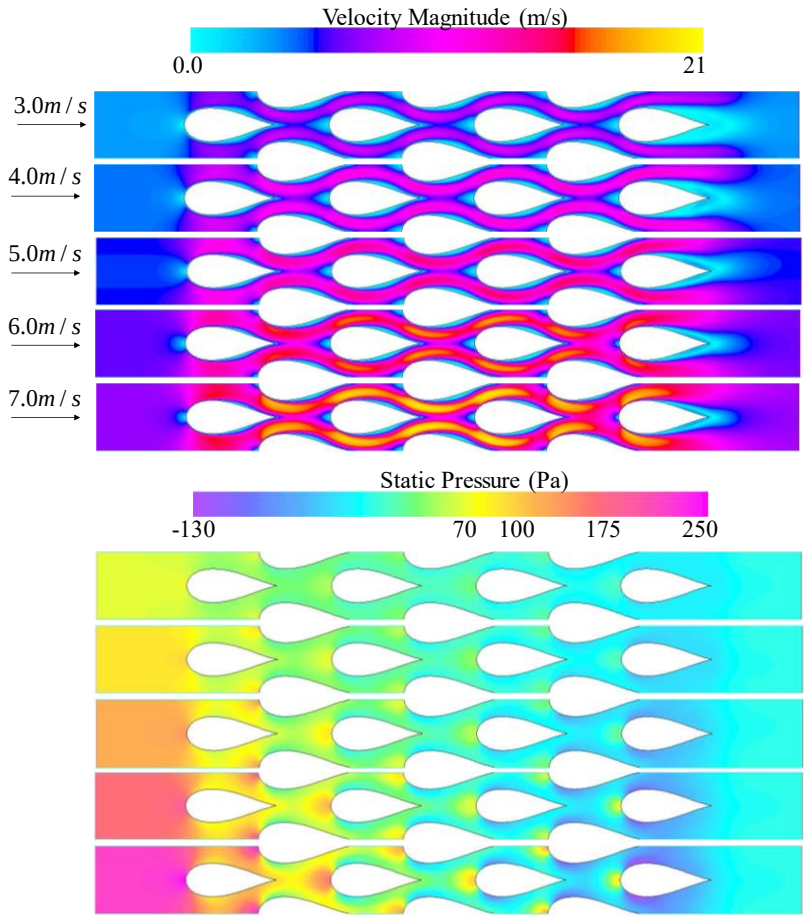

Figure 13 – NTHX-001 CFD Validation: Contour Plots.

2.3 10kW Radiator Optimization Results

The general optimization formulation and operating conditions are scaled based on the 1.0kW baseline. The main difference between this application and the previous is the water side pressure drop, which naturally will increase since longer tubes will be required. A maximum of 5kPa was established as a reasonable constraint as opposed to the 1.0kPa from the previous problem. For this application, only the RTHX surface was studied with the purpose of prototyping. Since the tubes for the BTHX-001 were available, a similar optimization problem (Eq. (29)) from the 1.0 kW HX optimization was performed for DP II as applied to the RTHX for fixed tube diameter. The optimization results (Figure 14) are presented with geometrical aspects per unit capacity such that the difference scales could be placed side-by-side. The designindicated in the optimization plot (Figure 14), RTHX-468, was selected for prototyping (Table 4).

$$
\begin{aligned}
&\min \Delta P_{air}, V_{HX} \\
&\text{s.t.} \\
&\Delta P_{air} \le 62 \text{ Pa} \\
&\Delta P_{water} \le 5.0 \text{ kPa} \\
&V_{HX} \le 1800 \text{ cm}^3 \\
&10 \le \dot{Q} \le 11 \text{ kW} \\
&D_o = 0.8 \text{ mm}
\end{aligned}
\tag{29}
$$

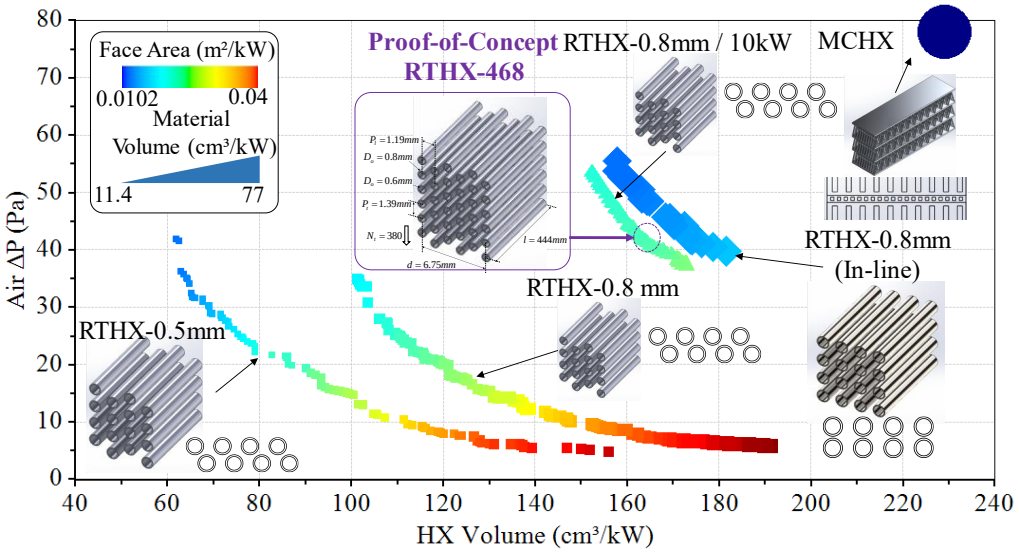

Figure 14 – DP II: Optimization Results.

Table 4 – 10kW BTHX Optimum Design.

OD	mm	0.8
HS	mm	1.19
VS	mm	1.39
L	mm	444
Tube banks	-	6
Tubes per bank	-	380
Total tubes	-	2280
FA	m^2	0.234
AHTA	m^2	2.51
Vol	cm^3	1667
AFR	m^3/s	0.3
RFR	g/s	250
ΔT	K	40
ΔP	Pa	44.1
AHTC	$W/m^2.K$	272.8
UA/V	$kW/m^3.K$	425
Q	kW	10.4
RΔP	kPa	5

2.4 Two-Phase HX Optimization

This study consisted of optimizing HX's to deliver a 3.0Ton (~10kW) capacity for a Heat Pump / Air-Conditioning Unit application. The baseline system is a rated SEER (Seasonal Energy Efficiency Ratio) 16 system using R410A as working fluid. This study considered the cooling operating mode only. The cycle was modeled and verified (Table 5) against the rated performance using VapCyc® [18]. The HX's were modeled in CoilDesigner® [17] per manufacturer specifications. The compressor was modeled using the manufacturer 10-coefficient model for mass flow rate and power predictions.

Table 5 – Baseline Cycle Verification.

Cycle	COP*	COP	Q	Sub-cooling	Super heating	Ref. ṁ	Evap. AFR	Cond. AFR
	-	-	kW	K	K	kg/s	m³/s	m³/s
Baseline (rated)	4.507	3.900	10.029	5.447	3.890	0.06224	0.505	1.84
Baseline (simulated)	4.506	3.858	10.025	5.445	3.901	0.06040	0.505	1.84

* *w/o fan power*

Engineering Equation Solver (EES®) [19] was used to investigate the potential for reducing pressure lift while maintaining the subcooling, superheating, and air flow rates while assuming constant isentropic efficiency for the compressor. The approach temperatures were monitored to avoid potential Second Law violations. New HX specifications were retrieved from the EES® model per a theoretical COP (Coefficient of Performance) improvement of 15% and outlet approach temperatures near 1.0°C (Figure 15).

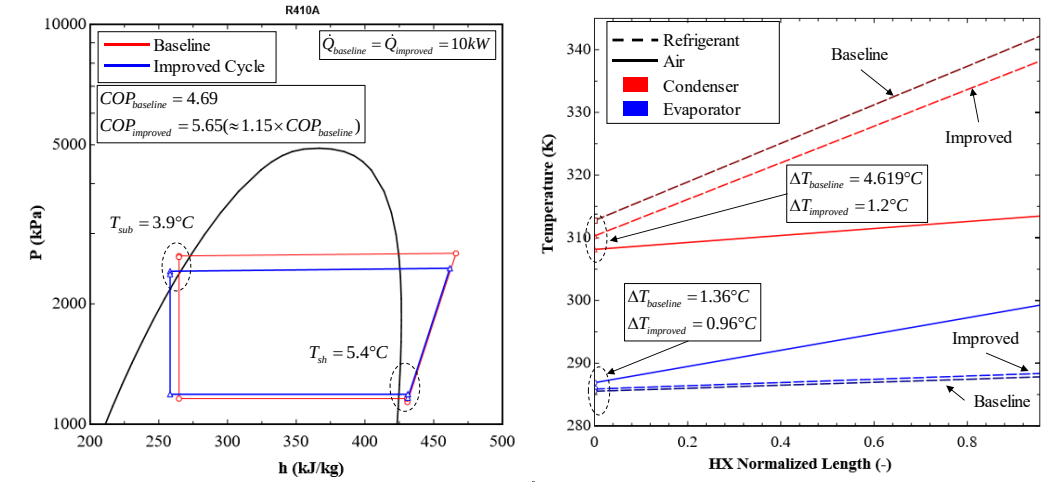

Figure 15 – System Level Study for COP Improvement.

2.4.1 HX Design and Optimization

The baseline HX's have conventional tubes and fins with tube diameters of 7.0mm and 9.5mm in the outdoor and indoor units, respectively. The fins are enhanced with louvers and slits. The HX operating conditions for both the baseline cycle and the expected improved cycle are presented in Table 6.

Table 6 – Two-Phase HX's Operating Conditions.

HX	Evaporator					Condenser				
Metric	P_{sat}	x_{in}	V_{air}	$T_{air,in}$	ΔP_{air}	P_{sat}	T_{in}	V_{air}	$T_{air,in}$	ΔP_{air}
	kPa	-	m³/s	K	Pa	kPa	K	m³/s	K	Pa
Baseline	1159	0.22	0.505	299.8	57.2*	2675	345.1	1.84	308.2	4.0**
Improved	1179	0.19	0.505	299.8	---	2488	339.7	1.84	308.2	---

* *Rated value* ** *Estimated using Wang et al. correlation* [20]

The fan power is estimated based on the total power to move air through both HX's. For design and optimization purposes, the baseline condenser pressure drop of 4.0Pa is highly restrictive; thus, the optimizer was constrained to a pressure drop of up to 10Pa. The evaporator pressure drop, however, was constrained such that total fan power is no higher than the baseline. The optimization problem (Eq. (30)) applied to each HX has airside pressure drop and HX envelope volume as objective functions while constraining capacity, rebalanced airside pressure drop, and refrigerant pressure drop.

Evaporator	Condenser
$\min \Delta P_{air}, V_{HX}$	$\min \Delta P_{air}, V_{HX}$
s.t.	s.t.
$\dot{Q} \geq 10.0$ kW	$\dot{Q} \geq 11.8$ kW
$\Delta P_{air} \leq 35$ Pa	$\Delta P_{air} \leq 10$ Pa
$\Delta P_{ref} \leq \Delta P_{ref,baseline}$	$\Delta P_{ref} \leq \Delta P_{ref,baseline}$

(30)

In addition to the design variables used in the DP I and II, pass configuration was introduced (Figure 16). For the evaporator, two passes are considered; the design variable indicates the fraction of the tubes as inlet with the remainder being the outlet. The condenser has three passes; two design variables define the fraction of the inlet tubes and the mid-section tubes, respectively.

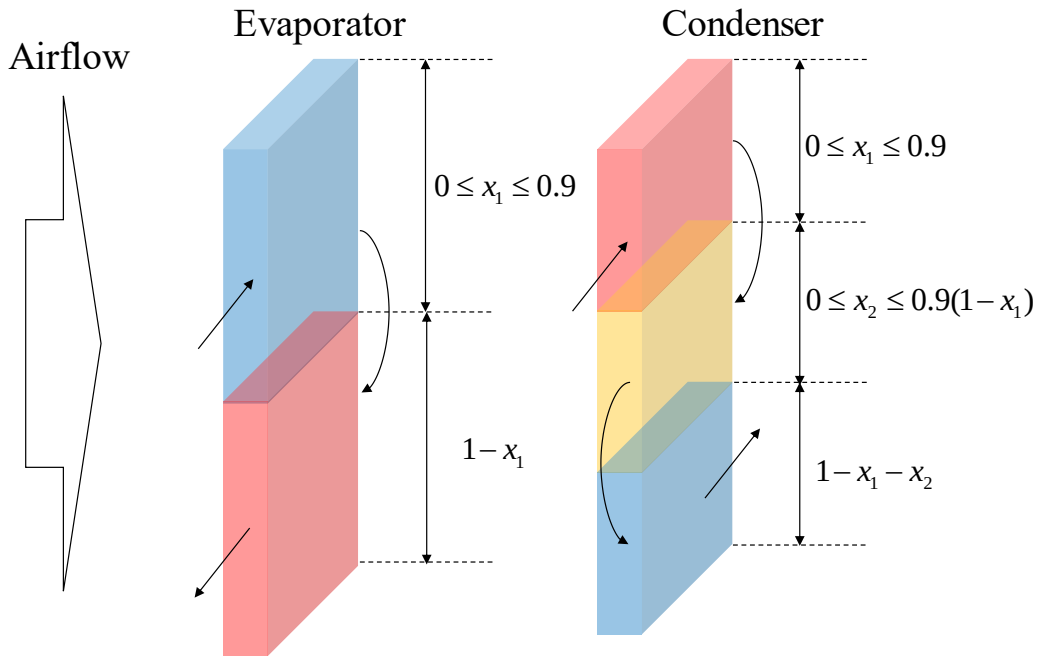

Figure 16 – HX Pass Configurations.

This study considered only the RTHX concept in both in-line and staggered arrangements. In addition to the optimum designs and baseline HX's, an optimization performed for a 3Ton SEER 13 unit [21] with HX's using 3, 4, and 5mm tube diameters was included for additional reference. Optimization results are shown in Figure 17.

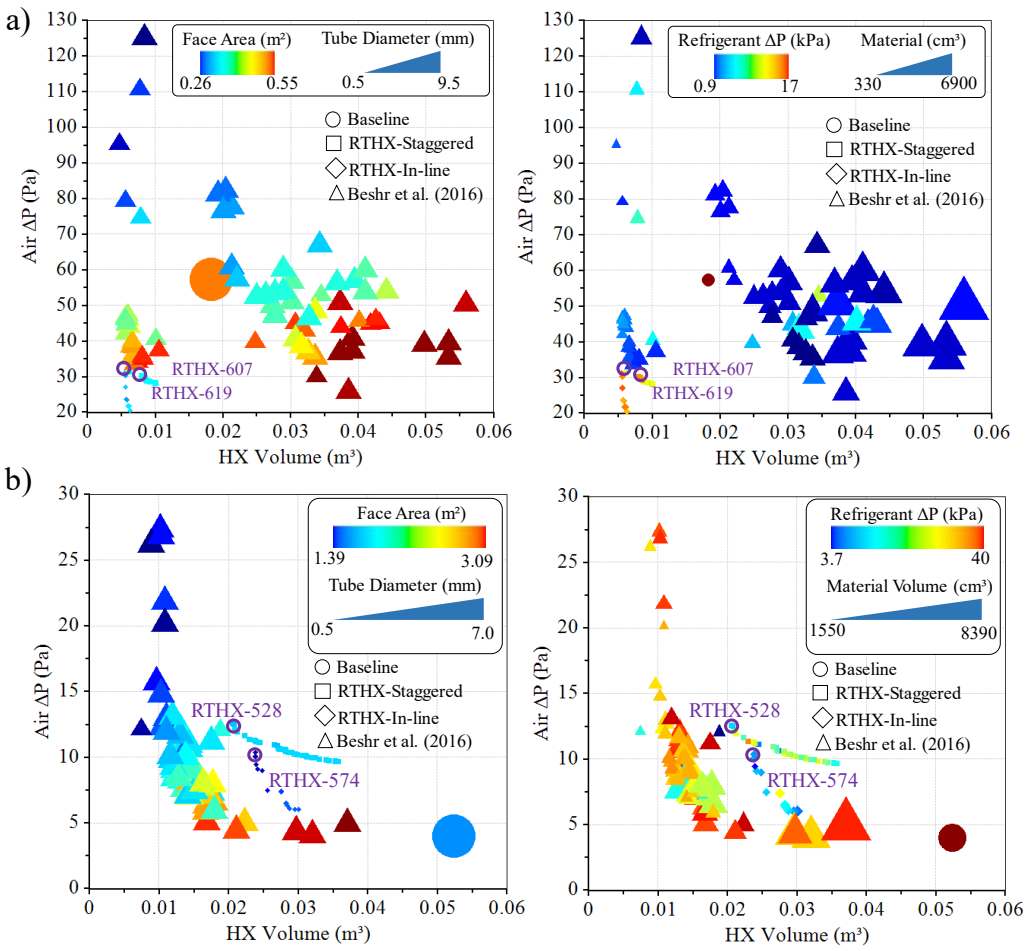

Figure 17 – DP III: Optimization Results.

2.4.2 System Level Analysis

The designs RTHX-528, 574, 607 and 619 indicated in Figure 17 were selected for system level analysis. Two novel cycles were simulated in VapCyc® [18]: Cycle I with the RTHX-528 and RTHX-607 designs and Cycle II with RTHX-574 and RTHX-619 designs. Both cycles resulted in significant refrigerant charge reduction: approximately 50% reduction in the condenser, and up to 90% in the evaporator. The overall charge reduction in the system reached approximately 30-40%. From a performance perspective, the COP improved up to 14% using the new HX's. Additionally, the charge reductions in the HX's resulted in the pipes accumulating a larger amount of relative charge. The system results are summarized in Figure 18.

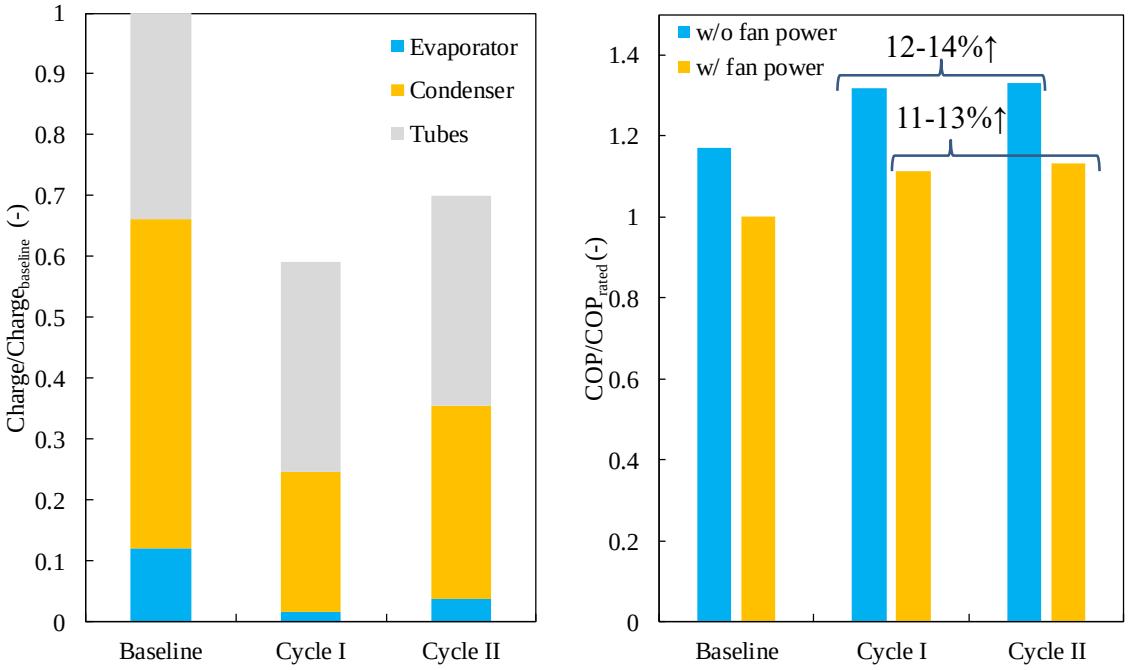

Figure 18 – DP III: System Level Analysis.

2.4.3 Charge Optimization

An additional optimization problem was applied to each HX using charge volume as an objective function instead of HX envelope volume. The optimization problem was identical to Eq. (30) except for the substitution of tube internal volume for HX envelope volume as an objective function. Tube internal volume served as a representation of charge volume since charge volume is difficult to precisely calculate due to void fraction distribution, that is, the fraction of the flow-channel volume occupied by vapor. Optimization results are shown in Figure 19. Staggered arrangement condensers show potential charge reduction at similar airside pressure drops compared to in-line arrangements. In-line arrangement evaporators have lower airside pressure drops for similar refrigerant charge volumes compared to staggered arrangements.

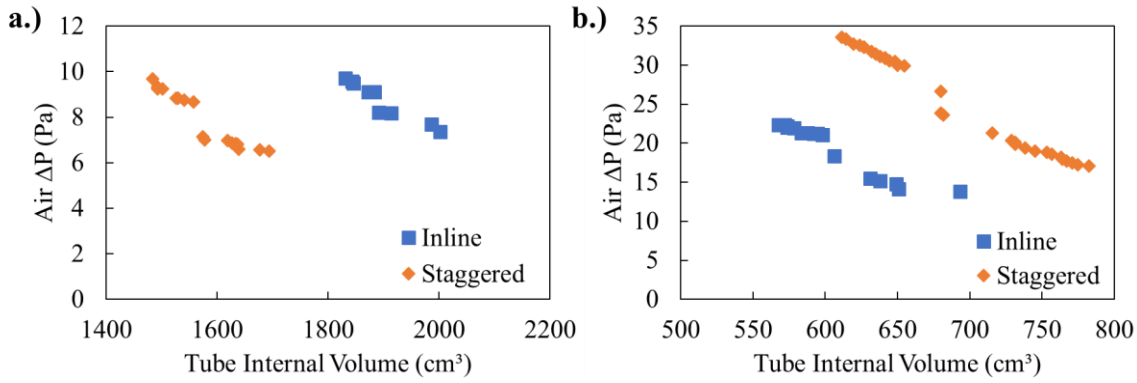

Figure 19 – Charge Optimization: a.) Condenser; b.) Evaporator.

2.5 Additional Mini Heat Exchanger Geometries

This section presents a summary of additional geometries numerically investigated by ORNL researchers. Four HX designs were investigated: (1) alternative offset-strip fin HX, (2) pipe-attached fins HX, (3) airfoil/droplet shape HX, and (4) EHD-enhanced HX.

2.5.1 Alternative Offset-Strip Fin Heat Exchanger

This HX design intended to use fins to deflect the flow and allow more air flow to contact the refrigerant pipe. An image of the design is shown in Figure 20. Note the fins are "open" in front of the pipes. As the air flow reaches the fins, part of the flow will go through the open window to the other side, which has the potential to increase the air flow path and thus air flow contact.

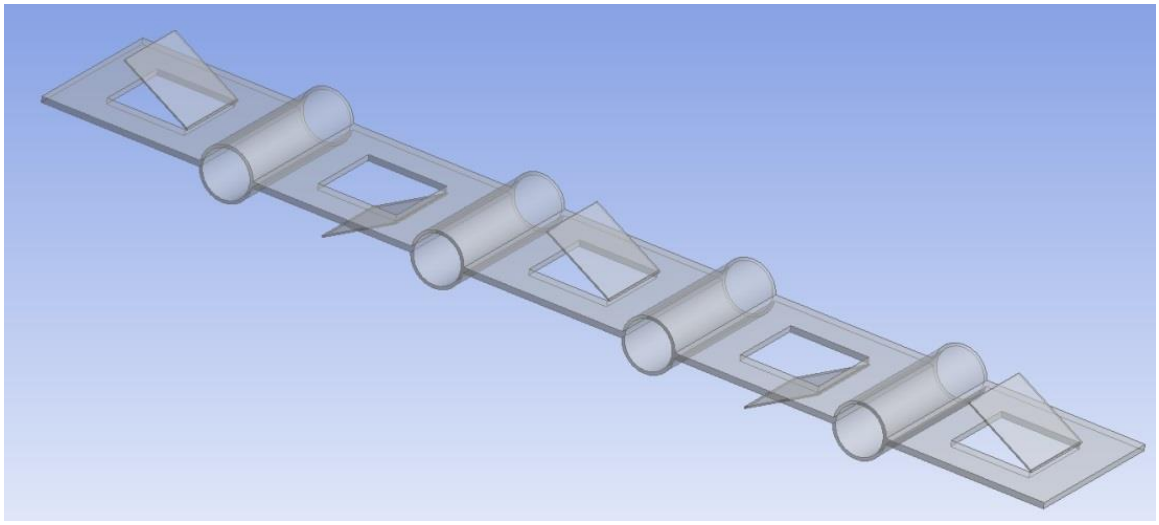

Figure 20 – Alternative Offset-Strip Fin HX.

Air flow streamline simulation results are shown in Figure 21. The fins successfully deflect some air flow to the other side of the pipe, however, the open fins also create a low velocity region behind them (see the red "A" in Figure 21). This may result in low heat transfer of the adjacent pipe. Additionally, the pipe connecting plates lead to a low-efficiency heat transfer surface, yielding a lower heat transfer coefficient.

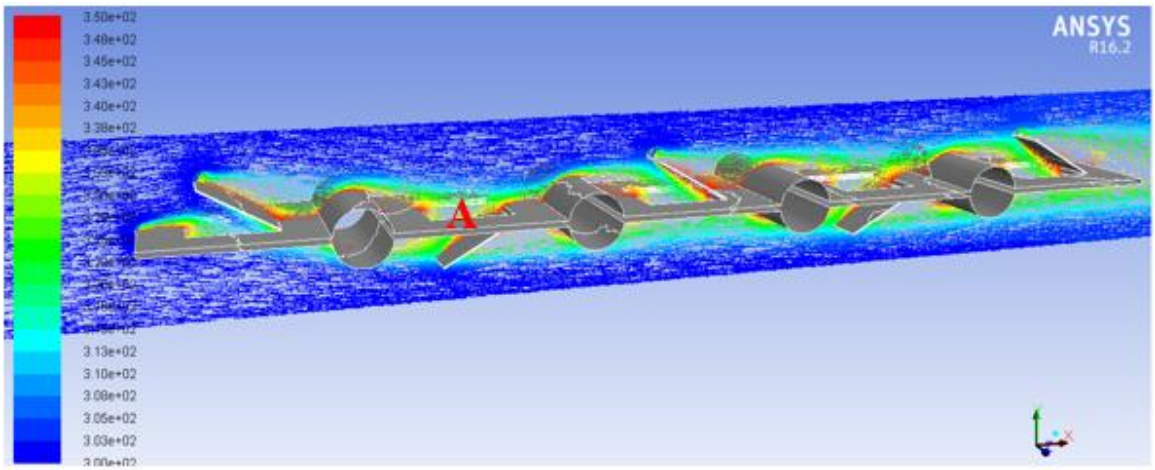

Figure 21 – Air Flow Streamlines around Alternative Offset-Strip Fin HX.

A 16-run Latin Hypercube Sampling (LHS) design was conducted to investigate the influence of different parameters on HX performance. Parameters studied included: refrigerant pipe inner diameter, vertical pipe spacing, horizontal pipe spacing, fin angle and fin length. The LHS design parameters and results are shown in Table 7 and Table 8, respectively. The experimental design shows that small vertical spacing and large fin length can lead to higher airside heat transfer coefficient.

Table 7 – Alternative Offset-Strip Fin HX LHS Design Parameters.

Run	Water Pipe Inner Diameter (mm)	Vertical Space (mm)	Horizontal space (mm)	Number Water Pipes	Fin Angle	Fin Side Length (mm)
1	1.35	3.375	5.295	5	43.594	2.283
2	0.95	6.125	1.796	3	15.469	0.662
3	1.25	6.875	1.973	8	18.281	0.875
4	1.45	4.875	3.648	10	37.969	1.755
5	1.85	5.875	5.521	4	29.531	2.726
6	1.75	6.375	3.855	6	7.031	1.277
7	1.05	3.625	3.954	8	32.344	1.260
8	1.15	5.625	2.713	9	9.844	1.238
9	0.65	4.375	2.245	8	1.406	0.856
10	0.55	3.125	0.954	5	12.656	0.399
11	1.95	4.125	6.429	5	35.156	2.210
12	1.65	4.625	5.955	9	26.719	2.792
13	0.45	5.375	0.921	7	40.781	0.363
14	1.55	3.875	4.141	4	4.219	1.682
15	0.75	6.625	2.355	7	23.906	0.721
16	0.85	5.125	2.404	6	21.094	0.856

Table 8 – Alternative Offset-Strip Fin HX LHS Results.

Run	Heat Rate (W)	Pressure Drop (Pa)	Average Outlet Temperature (K)	LMTD (K)	HTC (W/m^2K)
1	0.705	6.366	335.313	28.825	59.568
2	0.063	11.217	306.432	46.710	36.107
3	0.140	0.556	309.590	45.035	20.577
4	0.520	2.346	325.980	35.437	30.971
5	0.658	1.466	318.533	40.021	37.961
6	0.233	0.869	311.950	43.753	21.854
7	0.311	2.229	327.949	34.140	33.727
8	0.251	1.182	314.673	42.240	25.082
9	0.137	0.667	315.746	41.632	29.382
10	0.038	0.487	312.860	43.252	41.353
11	0.661	4.572	330.029	32.720	40.245
12	1.148	4.330	336.516	27.864	42.494
13	0.039	0.279	308.483	45.627	35.714
14	0.280	1.728	317.787	40.457	31.268

15	0.112	0.440	309.830	44.906	27.266
16	0.126	0.550	312.086	43.679	29.558

2.5.2 Pipe-Attached Fins Heat Exchanger

A second design attempted to limit low-efficiency heat transfer surface area by directly attaching the alternating-offset fins to the pipes. An image of the HX is shown in Figure 22. Air flow streamline simulation results are shown in Figure 23. Note the formation of vortices around the refrigerant pipes, which benefit heat transfer efficiency.

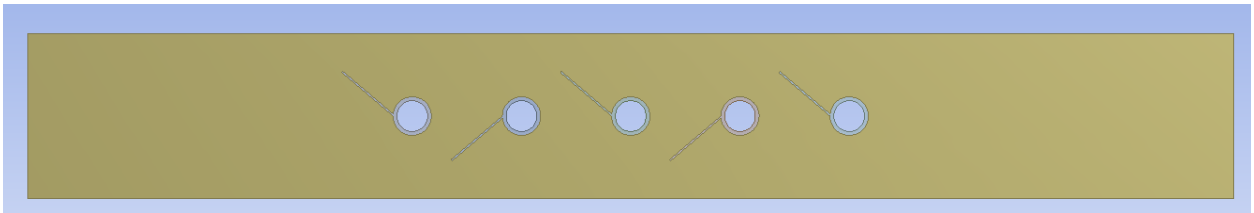

Figure 22 – Pipe-Attached Fin HX.

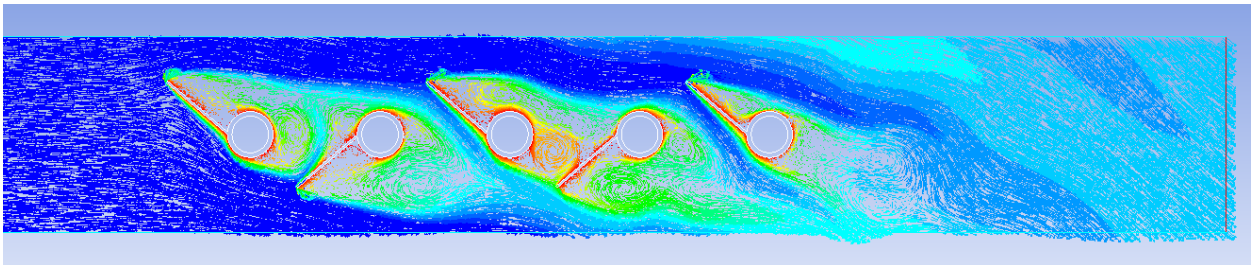

Figure 23 – Air Flow Streamlines around Pipe-Attached Fin HX.

A 60-run LHS design was conducted using the following design parameters: number of refrigerant pipes, fin length, angle between fin and horizontal, refrigerant pipe inner diameter, horizontal spacing and vertical spacing. The highest HTC achieved was 145.54W/m^{2}K, which was achieved at small vertical spacing and refrigerant pipe diameter. However, the fins increase airside pressure drop. The highest HTC design had an airside pressure drop of 75.55Pa, which is much higher than Alternative Offset-Fin HX design.

2.5.3 Airfoil/Droplet Shape Heat Exchanger

To diminish airside pressure drop penalty, refrigerant pipe cross-sections were changed from a circle to an airfoil and droplet cross-section. The airfoil shape is based on the EPPLER 862 STRUT AIRFOIL (e862-il). The HX shapes and flow regimes are shown in Figure 24.

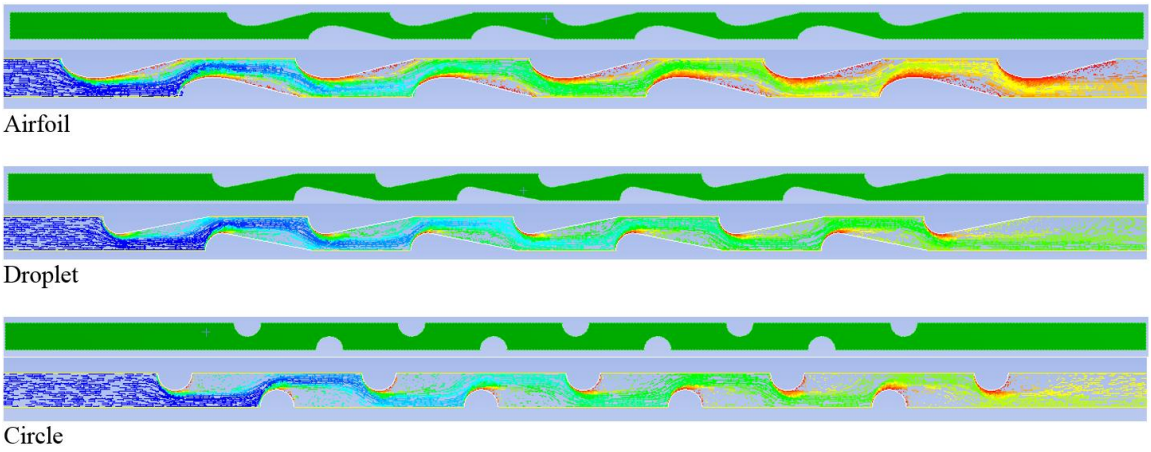

Figure 24 – Airfoil (top), Droplet (middle) and Circle (bottom) Cross-Section and Flow Structure.

Model results are compared in Table 9. Although air heat transfer coefficient is lower for the airfoil and droplet pipes compared to the circular pipes, the airfoil and droplet cross-sections could provide greater heat transfer rate with lower airside pressure drop. Moreover, while airfoil pipes have better performance versus droplet pipes, the fabrication of droplet cross-section pipes could be easier than airfoil shapes.

Table 9 – Airfoil, Droplet, and Circle Cross-Section HX Results Comparison.

	Length (Airfoil, Droplet); Diameter (Circle) (mm)	**Horizontal Space (mm)**	**Vertical Space (mm)**	**Heat Transfer Rate (W)**	**Pressure Drop (Pa)**	**Outlet Temperature (K)**	**LMTD (K)**	**HTC (W/m^2K)**
Airfoil	3.45	3.325	1.1	150.64	64.1	337.029	27.44	161.94
Droplet	3.45	3.325	1.1	146.08	74.3	335.907	28.35	147.99
Circle	1.12	3.325	1.1	132.1	106.8	332.469	30.98	269.3

Based on the droplet design, a droplet matrix was tested in two styles with different droplet angles. The styles are shown in Figure 25. Simulation results indicate that Style I (asymmetric) can offer higher heat transfer coefficient at the cost of steeper airside pressure drops as shown in Table 10.

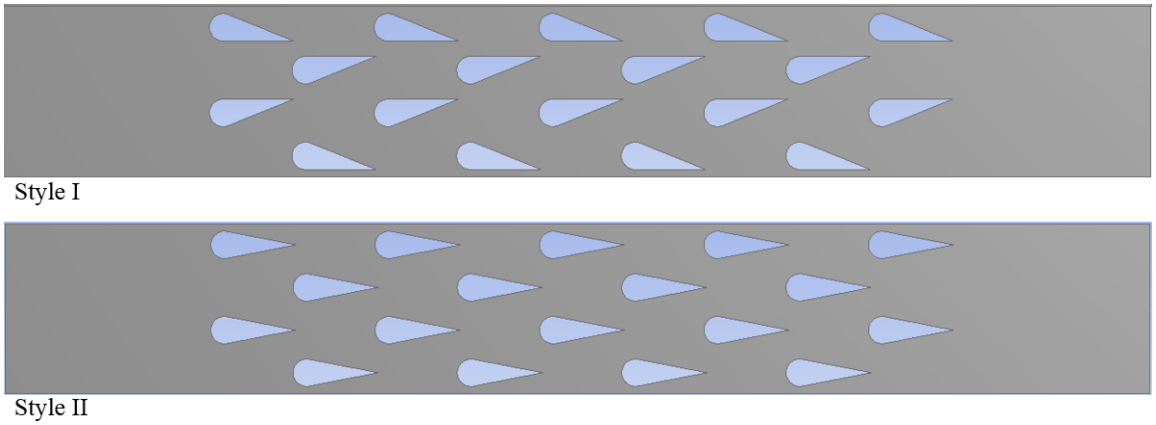

Figure 25 – Droplet Shape Pipe Styles: Asymmetric (top) and Symmetric (bottom).

Table 10 – Droplet Shape Pipe Simulation Results Comparison.

	Vertical Spacing (mm)	Heat Transfer Rate (W)	Pressure Drop (Pa)	HTC (W/m^2K)
Style I	2	732.10	44.76	144.81
	1.75	733.46	63.68	155.27
	1.5	720.54	97.89	167.43
Style II	2	645.94	23.42	122.00
	1.75	620.57	28.13	121.43
	1.5	600.03	35.42	124.05

2.5.4 EHD-Enhanced Mini Heat Exchanger

A numerical study was conducted on the electrohydrodynamic (EHD) enhanced mini HX. A schematic of the EHD-enhanced mini HX simulation setup is shown in Figure 26. The metal wire radius is 30μm, and the channel size is 6mm height with 10mm depth. Simulation results for center surface velocity vectors are shown in Figure 27. Results indicate that HTC is tremendously increased (about 3 times) by introducing EHD due to extra flow from the metal wire to refrigerant pipe which is induced by EHD. However, the electric power consumption is high under current conditions.

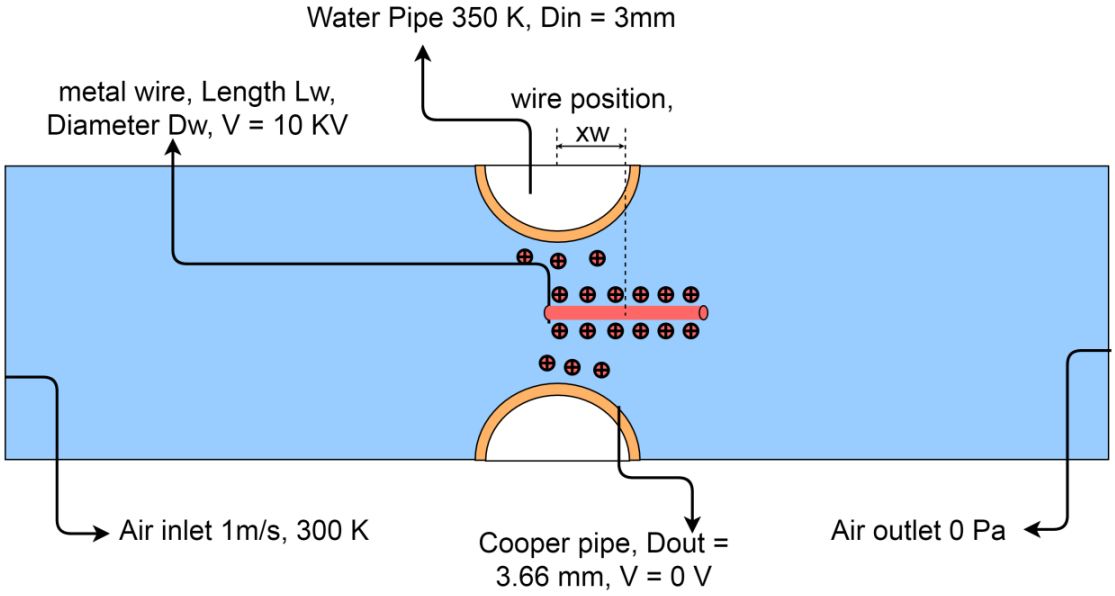

Figure 26 – EHD-Enhanced Mini HX Simulation Schematic.

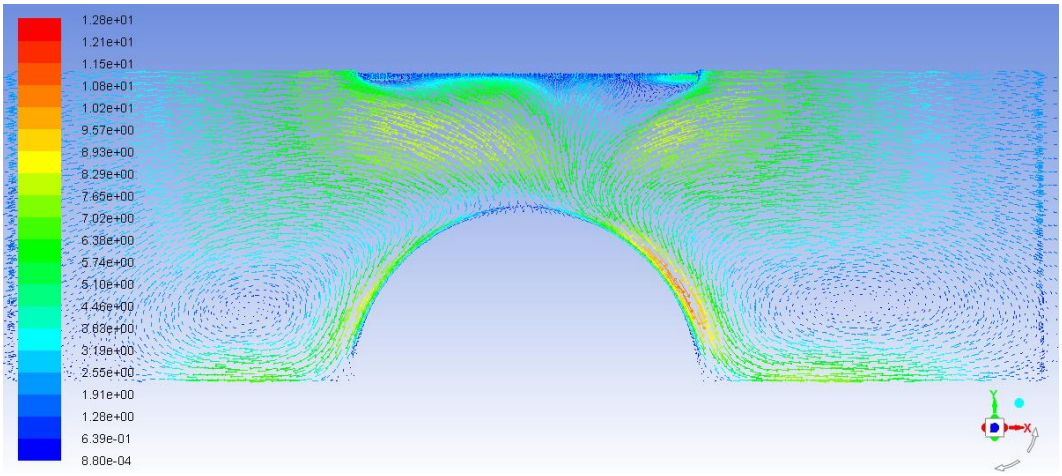

Figure 27 – Velocity Vector Field at Simulation Domain Center.

A three-factor Box-Behnken design was conducted on the EHD-enhanced mini HX with wire length (L_w), wire position (x_w), and wire diameter (D_w) as factors. Wire position is defined as the distance between refrigerant pipe center and wire center. Experimental design parameters and results are shown in Table 11. The last row of the table gives results from a HX with no EHD effect. The best option from this experiment is Run 5 (highlighted in Table 11), with short wire $(L_w = 1.66\text{mm})$ and small wire diameter $(D_w = 30\mu\text{m})$ located above the center of the refrigerant pipe $(x_w = 0\text{mm})$. This design could provide heat transfer coefficient enhancement up to a factor of three compared to the reference with a low airside pressure drop and relatively low power consumption. Further, that wire location bias to either direction will reduce heat transfer coefficient. However, as previously mentioned, current electric power consumption is high. More research should be conducted to find a method to effectively limit power consumption.

Table 11 – EHD-Enhanced Mini HX Box-Behnken Design Parameters and Results.

Run	Lw (mm)	xw (mm)	Dw (µm)	Net Heat Transfer Rate (w)	Outlet Temperature (K)	LMTD (K)	HTC (W/m^2K)	Pressure Drop (Pa)	Power Consumption (W)
1	1.66	-1.66	60	0.476	312.700	43.340	210.746	-30.109	1.829
2	4.98	-1.66	60	0.525	314.200	42.505	236.666	-37.275	3.10
3	1.66	1.66	60	0.506	313.670	42.802	226.675	72.311	1.846
4	4.98	1.66	60	0.601	316.204	41.370	278.433	71.018	3.20
5	1.66	0	30	0.673	318.190	40.222	320.950	2.831	2.54
6	4.98	0	30	0.736	319.930	39.194	360.283	13.337	3.73
7	1.66	0	90	0.666	318.010	40.327	316.865	2.825	3.15
8	4.98	0	90	0.720	319.460	39.474	349.709	13.943	4.17
9	3.32	-1.66	30	0.512	313.870	42.690	230.044	-36.888	2.44
10	3.32	1.66	30	0.576	315.600	41.715	264.931	74.450	2.46
11	3.32	-1.66	90	0.495	313.410	42.947	221.196	-34.316	2.70
12	3.32	1.66	90	0.569	315.370	41.846	260.512	71.652	2.72
13	3.32	0	60	0.691	318.674	39.938	331.624	6.754	2.8
14	3.32	0	60	0.691	318.674	39.938	331.624	6.754	2.8
15	3.32	0	60	0.691	318.674	39.938	331.624	6.754	2.8
Reference				0.258	306.974	46.426	106.537	1.920	

3 Experimental Work

A test facility was designed and constructed at the University of Maryland, College Park for both airside and refrigerant side prototype heat exchanger testing. This chapter will begin with a description of the test facility, then will present experimental results for the HX prototypes. Data acquisition uncertainty analysis will be discussed at the end of the chapter.

3.1 Test Facility Description

Experimental specifications are summarized in Table 12.

Table 12 – Experimental Specifications.

Item	Capacity
Coil Test Dimensions	• Max. 24" X 24" (Width X Height)
Heat Transfer Capacity	• Max. 10 kW
Max. Air Velocity	• Max. 5 m/s for the largest section (24" by 24")
Inlet Air Conditions	• -10°C to 45°C • Humidity control
Working Fluids	• Refrigerant without oil – pumped system • Refrigerant with oil – standard vapor compression system • Water - water flow rate – up to 2.5 kg/s • Brine

The facility should be designed properly to get reliable results. Several facility design criteria are stated herein. The airside and refrigerant side test facilities are modular designed for easy movement between the Heat Pump Lab (Building 0092, UMD) and Energy Lab (Building 0089, UMD). Also, the dimensions of each module must fit the smallest door / space between the Heat Pump and Energy Labs. Second, a wind tunnel is designed which is capable of using two different test sections for use with different sized HX. The two test sections should be mobile and interchangeable. Third, to build an accurate test facility, high accuracy, repeatability, and reliability instrumentations are selected. However, cost must also be considered. Fourth, to create different working and testing conditions for a HX, three different refrigerant loops are applied. Fifth, sealing and insulation should be considered to reduce the error. Finally, to reduce test facility energy consumption, a closed air loop is designed.

3.1.1 Airside Test Facility

A closed air loop was chosen to reduce energy consumption. A schematic diagram of the airside loop is shown in Figure 28.

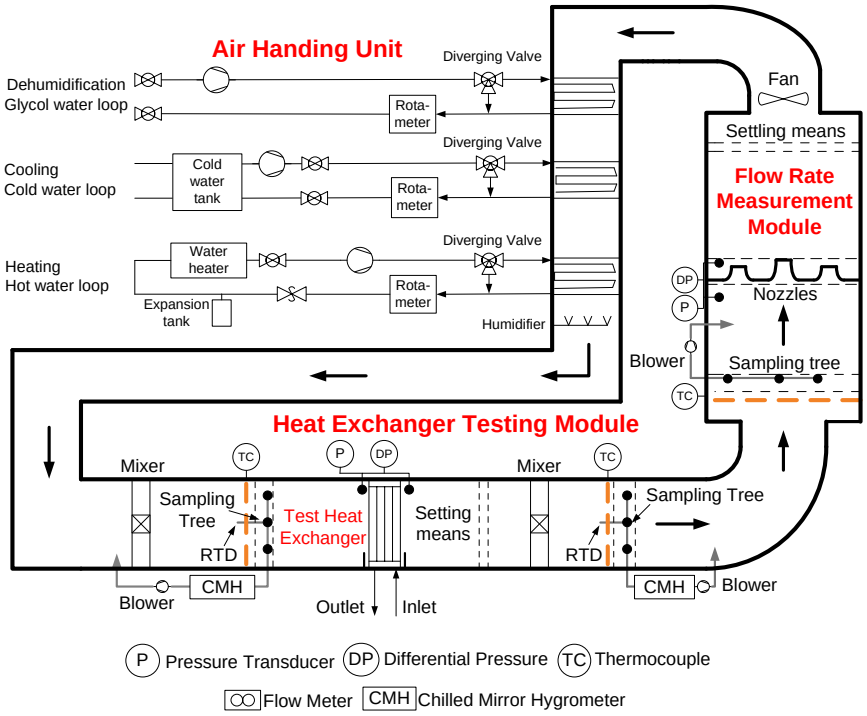

Figure 28 – Schematic Diagram of Airside Test Facility.

3.1.2 Refrigerant Side Test Facility

A refrigerant loop was designed for use with various refrigerants including: R410A, R134a, R404A, R407C, R32 and R1234yf. The refrigerant loop is capable of testing HX's with capacities ranging from 500 to 10,000W. Test facility specifications are listed in Table 13. The facility construction was completed, and the system was tested to ensure it was leak-tight. Refrigerant schematic diagrams are shown in Figure 29, Figure 30, Figure 31, and Figure 32.

Table 13 – Test Facility Specifications

	Fluid	Properties	Small Test Section	Large Test Section
Operating conditions	Air	Capacity	1~10 kW (0.3~3 ton)	3~10 kW (1~3 ton)
		Flow rate	0.03~0.167 m^3/s (66~350 cfm)	0.167~1.42 m^3/s (350~3000 cfm)
		Pressure drop	≤ 246 Pa (≤ 25 mmH_2O)	
		Inlet temperature	6~35 °C (43~95 °F)	
		Inlet humidity	30~95 % RH	
	Water	Flow rate	≤ 500 g/s (≤ 0.13 lb/min)	
		Inlet temperature	6~60 °C (43~140 °F)	
	R410A, R134a, R404A, R407C R32, R1234yf	Flow rate	3~70 g/s (0.4~9.3 lb/min)	
Cross section area		Length	≤ 0.33 m (≤ 13")	≤ 0.64 m (≤ 25")
		Height	≤ 0.33 m (≤ 13")	≤ 0.64 m (≤ 25")
		Depth	≤ 0.25 m (≤ 10")	≤ 0.20 m (≤ 8")

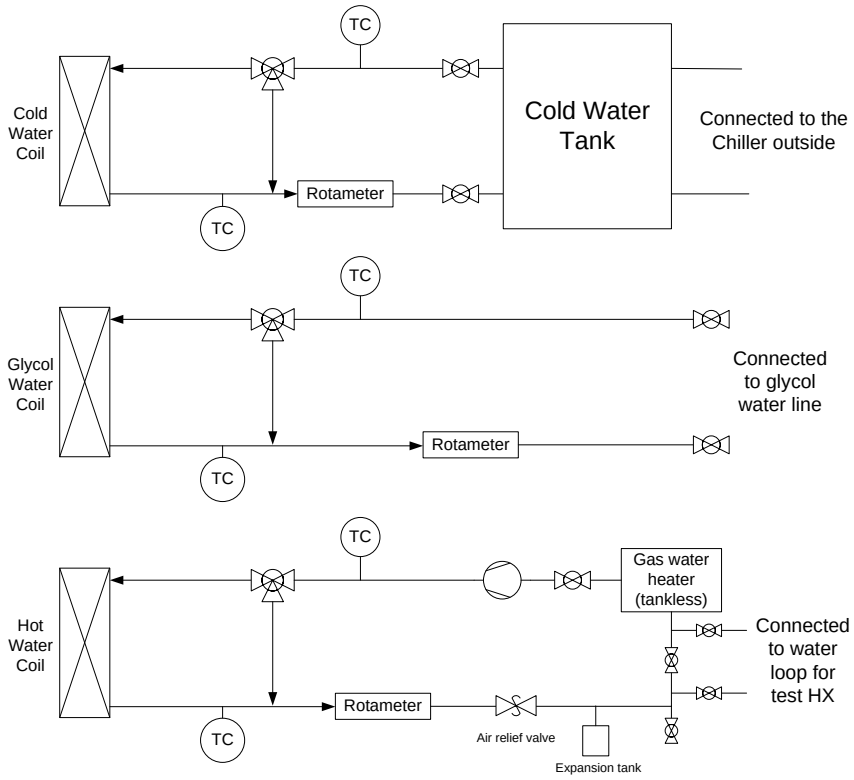

Figure 29 – Cold Water Loop (top), Glycol Water Loop (middle), Hot Water Loop (bottom) Schematic Diagram.

Water/Brines Loop

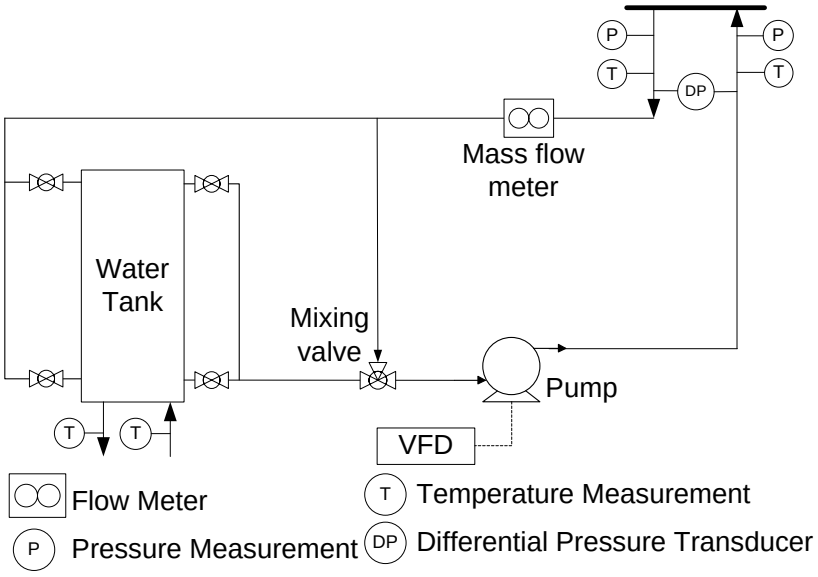

Figure 30 – Water/Brines System Loop Schematic Diagram.

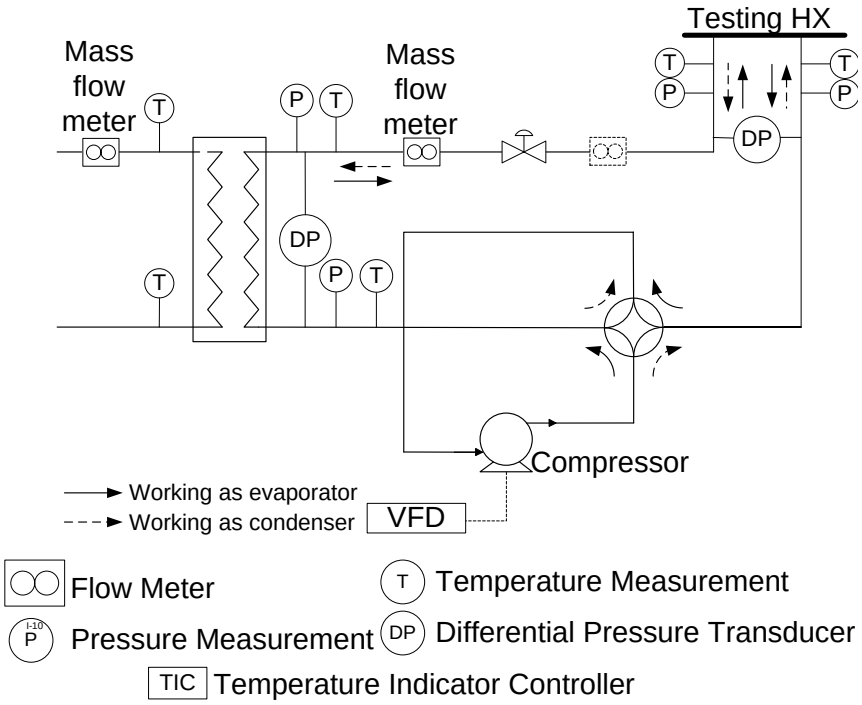

Figure 31 – Refrigerant System with Oil Loop Schematic Diagram.

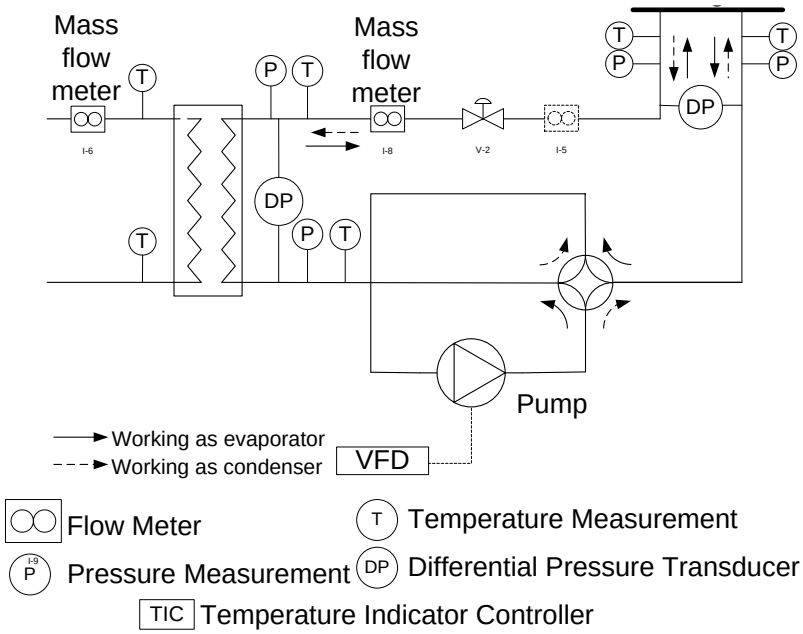

Figure 32 – Refrigerant System without Oil Schematic Diagram.

3.2 NTHX-001

NTHX-001 was developed when including tube shape parametrization to the optimization problem. The tube shapes are created with Non-Uniform Rational B-Spline (NURBS). See Appendix B for a detailed

explanation of NURBS-shape tubes. The key dimensions of NTHX-001 are given in Table 14. The cross-section properties are shown in Figure 33. The 3D-printed NTHX-001 specimen is shown in Figure 34.

Table 14 – NTHX Design for Manufacture.

Design Variable	Unit	NTHX
Tube Width	mm	3
Tube Height	mm	1.11
Min wall thickness	mm	0.3
Pl	mm	2.4
Pt	mm	2
Ports	-	7
Rows	-	45
Tube Length	mm	100

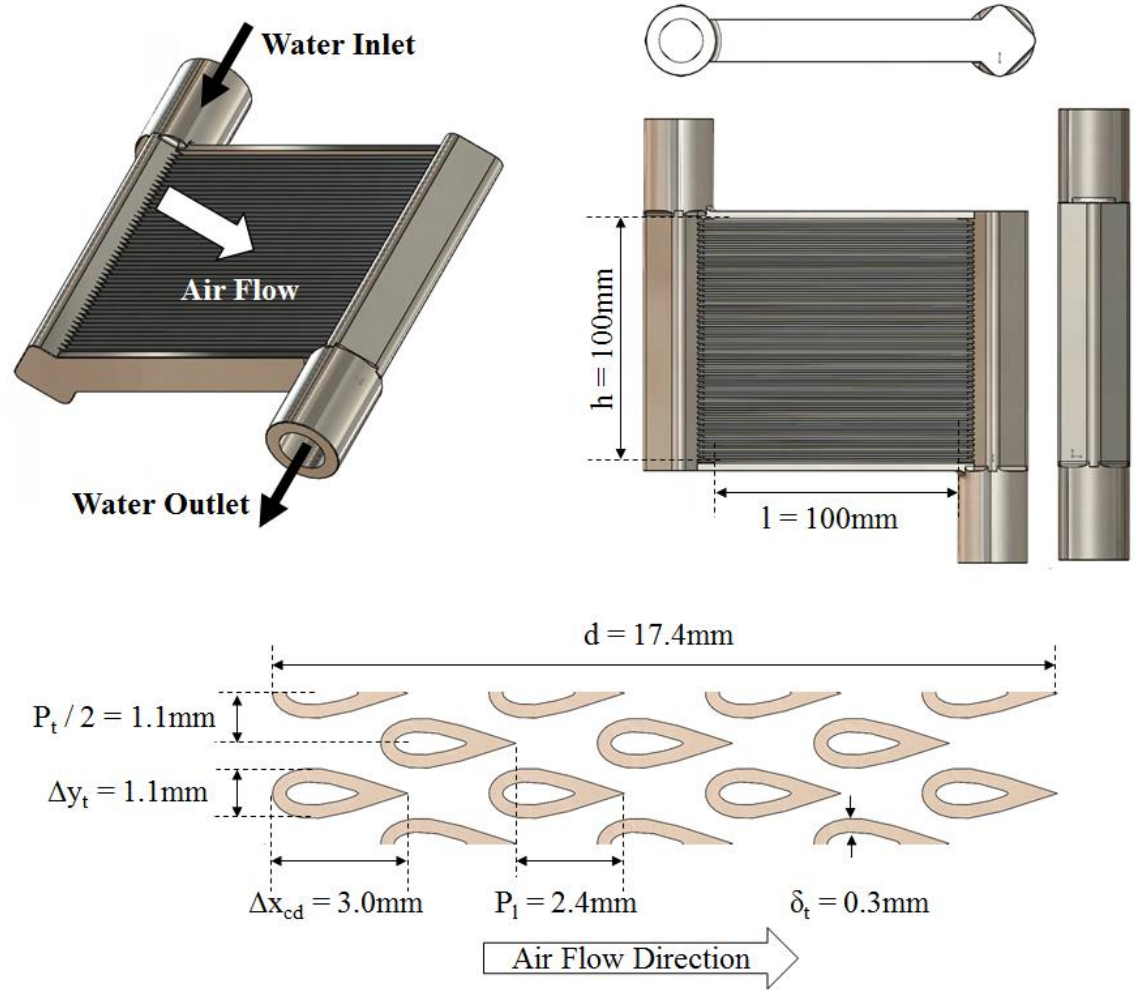

Figure 33 – NURBS Tube Shape HX.

Figure 34 – 3D printed NURBS Shape Tube HX.

3.2.1 Wilson Plot Method

Wilson plot method is a widely-used method to determine convection coefficient using experimental data. The overall thermal resistance can be expressed as the summation of water convection thermal resistance R_w, tube wall thermal resistance R_{tw}, and airside convection thermal resistance R_a. For simplicity, thermal resistances due to fluid fouling are neglected. Thus, overall thermal resistance, R_{ov}, could be written as Eq. (31):

$$R_{ov} = R_a + R_{tw} + R_w \tag{31}$$

Based on experimental data, overall thermal resistance could be evaluated using either ε-NTU method or UA-LMTD method. UA-LMTD method was chosen in current study since there is no specific ε-NTU correlation for NTHX-001 and both the inlet and outlet temperatures of each fluid is measured. For a cross-flow heat exchanger, the heating capacity could be evaluated as Eq. (32):

$$\dot{Q} = UAF\Delta T_{lm} \tag{32}$$

Where ΔT_{lm} is the LMTD for counter-flow and F is the LMTD correction factor for the cross-flow HX. F is determined by temperature effectiveness P, heat capacity rate ratio R_c, and flow pattern. Thus, overall thermal resistance could be expressed as Eq. (33):

$$R_{ov} = \frac{1}{UA} = \frac{F\dot{Q}}{\Delta T_{lm}} \tag{33}$$

In current study, the water flow rate (35 g/s) and inlet water temperature (60°C) were kept constant, thus the Reynolds number (*Re*) and Nusselt number (*Nu*) of water side do not vary much. Thus, the thermal resistance of water side could be taken as constant. Since air inlet temperature and water inlet temperature were both kept constant, the thermal resistance of tube wall could also be taken as constant. That is, water convection thermal resistance and tube wall thermal resistance could be expressed as Eq. (34):

$$R_{tw} + R_w = C_1 \tag{34}$$

Airside heat transfer coefficient can be expressed as a function of velocity as Eq. (35):

$$h_a = C_0 v^m \tag{35}$$

Combining Eq. (33) – (35), the regression form is derived as Eq. (36):

$$R_{ov} = \frac{1}{C_0} \cdot \frac{1}{Av^m} + C_1 \tag{36}$$

A linear regression was applied to obtain the values of C_0, C_1, and best curve fitting was used to find m. The results are shown in Figure 35.

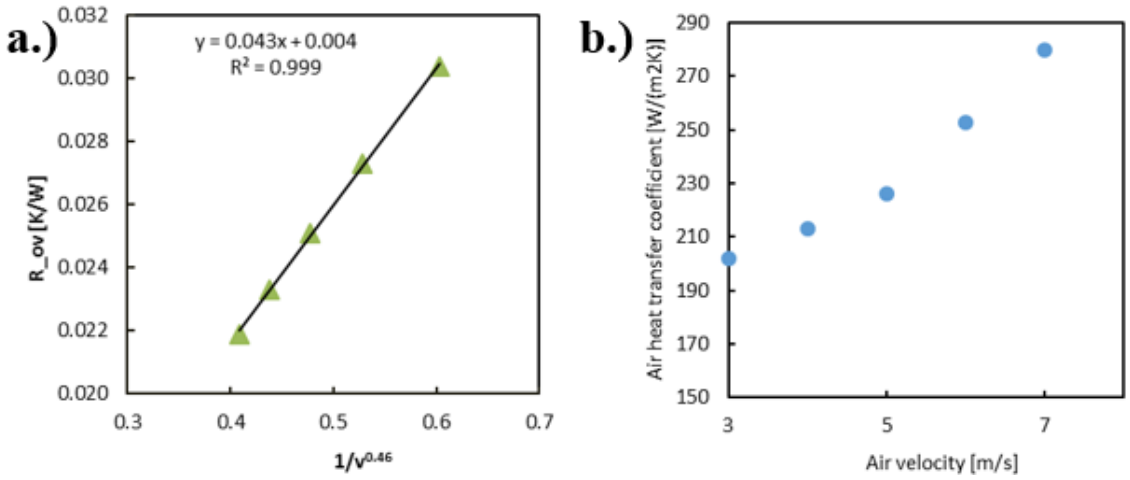

Figure 35 – a.) NTHX-001 Wilson Plot; b.) Air HTC

For this design, a correlation for air heat transfer coefficient and velocity could be developed as:

$$h = 106 v^{0.46}; \quad 3 \le v \le 7 \; m/s \tag{37}$$

3.2.2 Experimental Results

Three different water flow rates and five air flow rates were tested. Results for capacity and airside pressure drop are shown in Figure 36 and

Figure **37**, respectively. Energy balance of water and airside are all within 5% for all test conditions, as shown in

Figure **38**. See Chapter 2.2.1 for experimental/simulation validations.

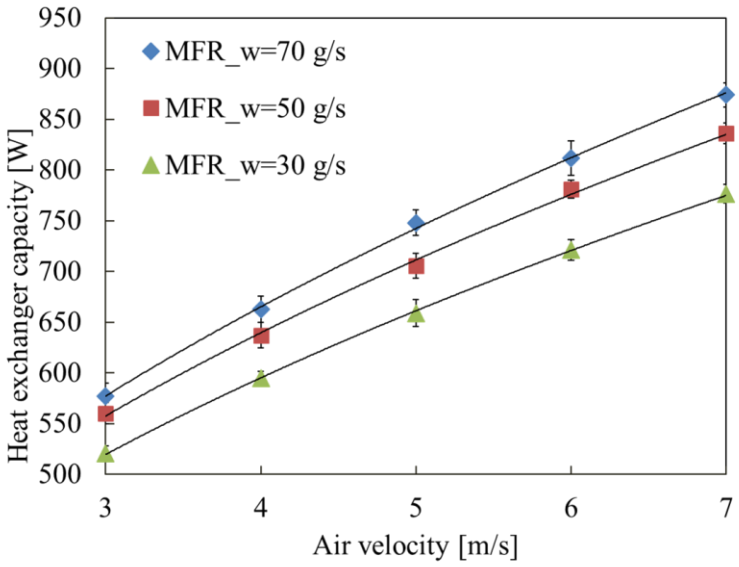

Figure 36 – NTHX-001 Capacity.

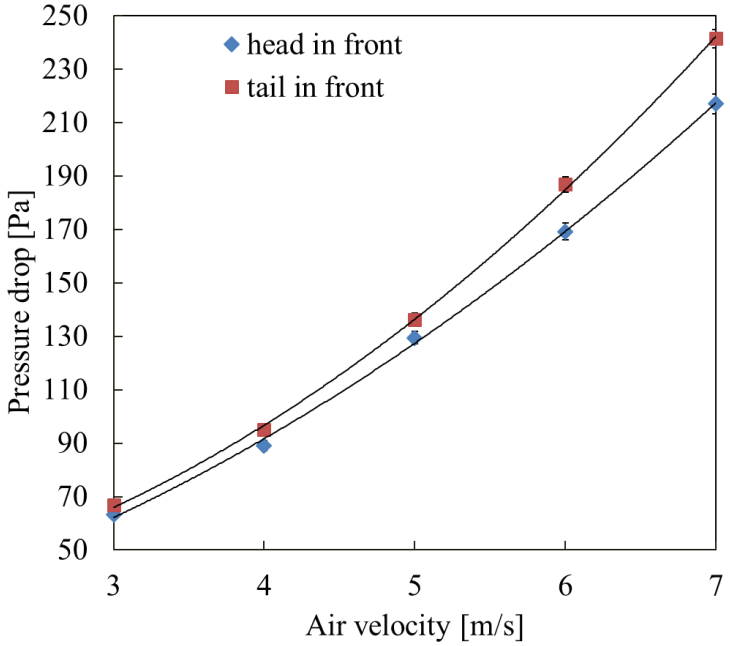

Figure 37 – NTHX-001 Airside Pressure Drop.

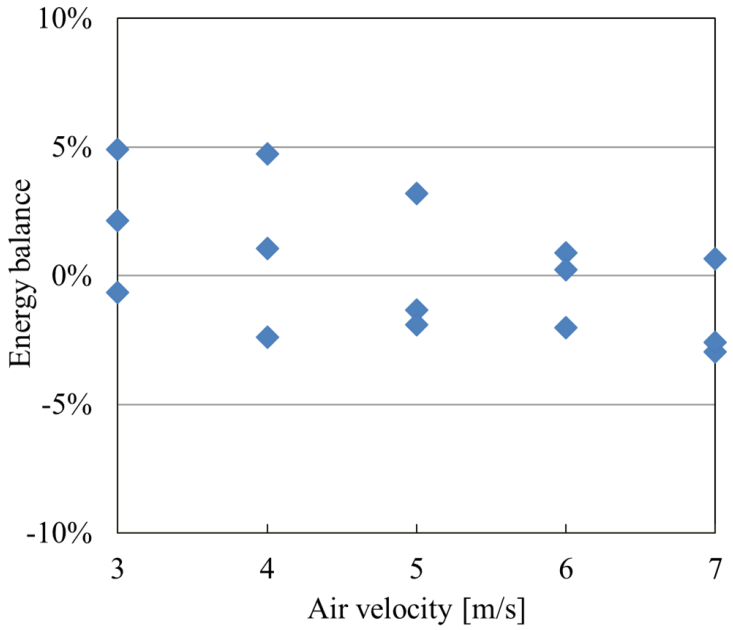

Figure 38 – NTHX-001 Energy Balance.

3.3 BTHX-001

The BTHX-001 was made of 484 stainless steel bare tubes. It was mounted in the duct as shown in Figure 39. A drain pan was placed underneath to collect condensate water. All condensate water was measured using a scale. BTHX-001 was tested under both dry and wet conditions in both vertical and horizontal orientations.

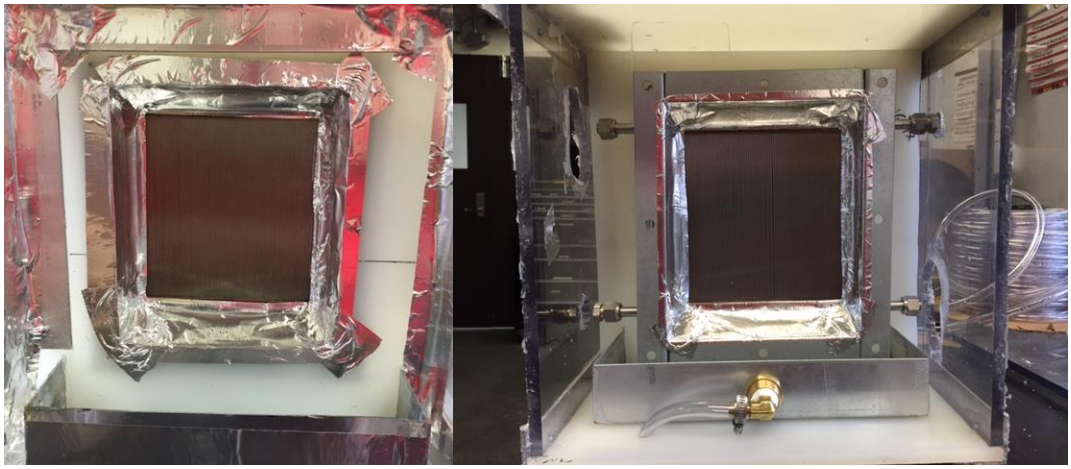

Figure 39 - BTHX-001.

3.3.1 Wilson Plot Method

Three different water flow rates and five air flow rates are tested. Results are shown in Figure 40 and Figure 41. Energy balance between airside and water are within 5% for all test conditions as shown in

Figure 42.

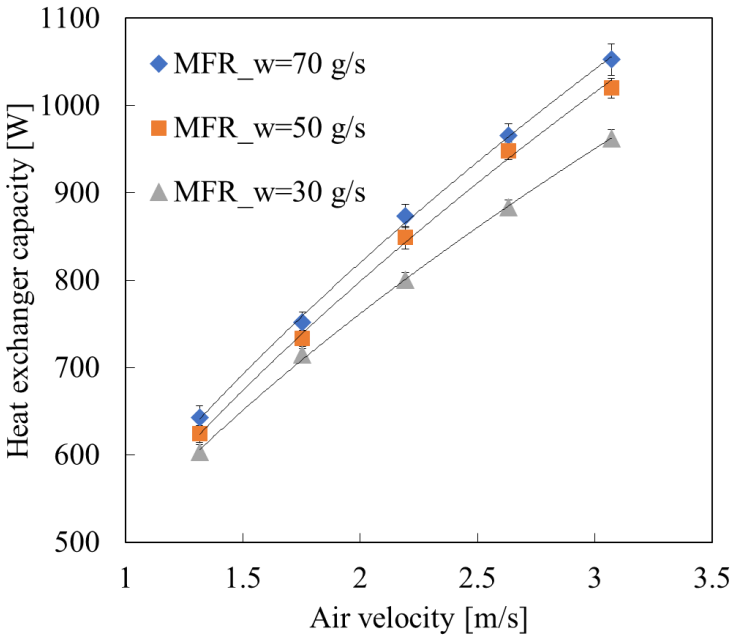

Figure 40 – BTHX-001 Capacity.

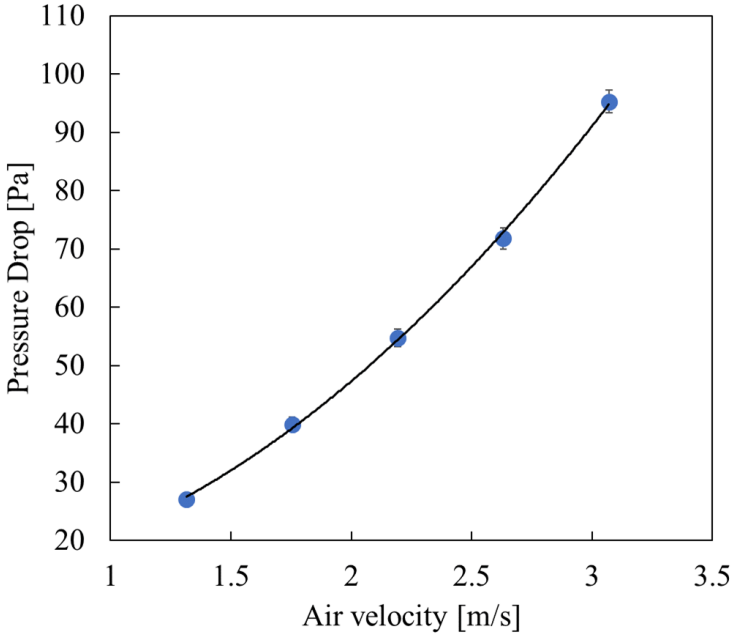

Figure 41 – BTHX-001 Airside Pressure Drop.

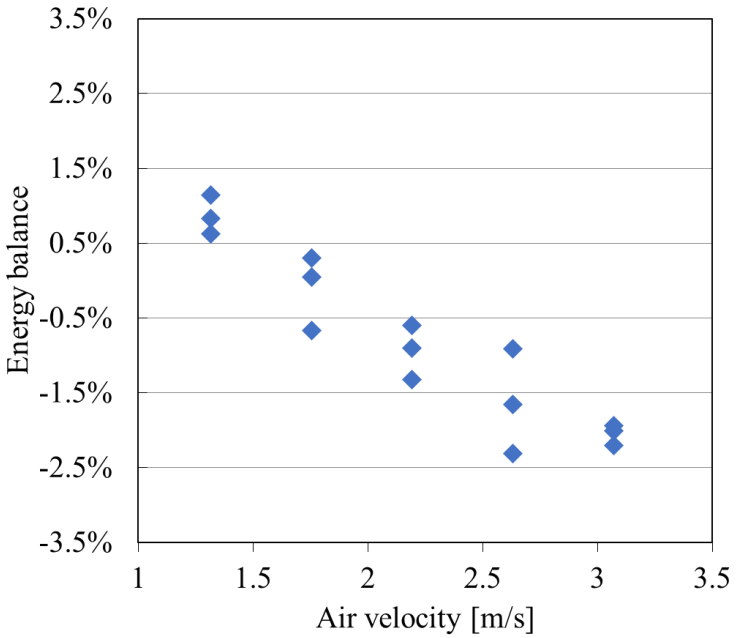

Figure 42 – BTHX-001 Energy Balance.

Wilson plot method was applied to BTHX-001 as well. Results are shown in Figure 43.

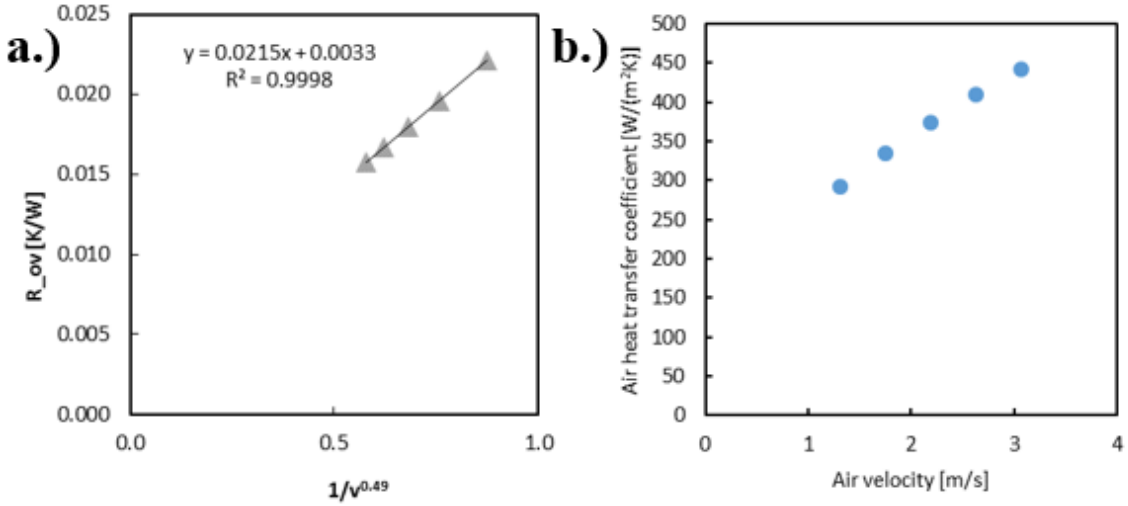

Figure 43 – a.) BTHX-001 Wilson Plot; b.) Air HTC

For this design, an airside heat transfer coefficient and velocity correlation could be developed from the methodology in Chapter 3.2.1 as Eq. (38):

$$h = 253v^{0.49}; \quad 1.3 \le v \le 3.0\ m/s \tag{38}$$

3.3.2 Test Matrix

The test matrix is listed ins

Table **15**. All uncertainty values are based on ASHRAE Standard 33-2000 [22]. See Appendix C for a comprehensive listing of test data tables.s

Table 15 – Wet Condition Test Matrix.

Fluid	Property		Value	Unit
Air	Inlet air temperature		26.7 ± 0.3	°C
	Inlet air condition 1 (dry)	T_wet_bulb	16.6 ± 0.3	°C
		RH	35 ± 1.9	%
		T_dew	10 ± 0.7	°C
	Inlet air condition 2 (wet)	T_wet_bulb	19.4 ± 0.3	°C
		RH	51± 1.9	%
		T_dew	15.6 ± 0.8	°C
	Inlet air condition 3 (wet)	T_wet_bulb	22.5 ± 0.3	°C
		RH	70 ± 2.7	%
		T_dew	20.8 ± 0.5	°C
	Air flow rate		0.03 ± 0.0003	m^3/s
			0.06 ± 0.0003	m^3/s
			0.09 ± 0.0003	m^3/s
Water	Inlet water temperature		12 ± 0.1	°C
	Water mass flow rate		20 ± 0.2	g/s
			35 ± 0.4	g/s
			50 ± 0.5	g/s

3.3.3 Vertical Orientation

All vertical orientation test results will be explained herein. The energy balance of all test data is within ± 4.7%, shown in Figure 44. Capacity results are shown in Figure 45, while sensible and latent heat results are shown in Figure 46 and Figure 47, respectively. As water flow rate increases, total capacity, sensible heat and latent heat all increase. As inlet air relative humidity increases, total capacity increases, sensible heat decreases and latent heat decreases. This is because higher latent heat leads to more accumulation of condensing water on the HX surface, which restrains sensible heat transfer. When air flow rate increases, total heat capacity and sensible heat increase while latent heat can either increase or decrease. Typically, when air flow rate increases, total capacity and water side outlet temperature increase. Thus, the wall temperature is higher, so the latent heat is expected to decrease at higher air flow rates. However, after the HX surface is fully wet, higher flow rates cause the blow out effect, i.e., when condensate water is directly removed from HX tubes by the air stream. This occurs when air velocity is high and surface tension is low. The blow-out effect causes latent heat transfer to increase.s

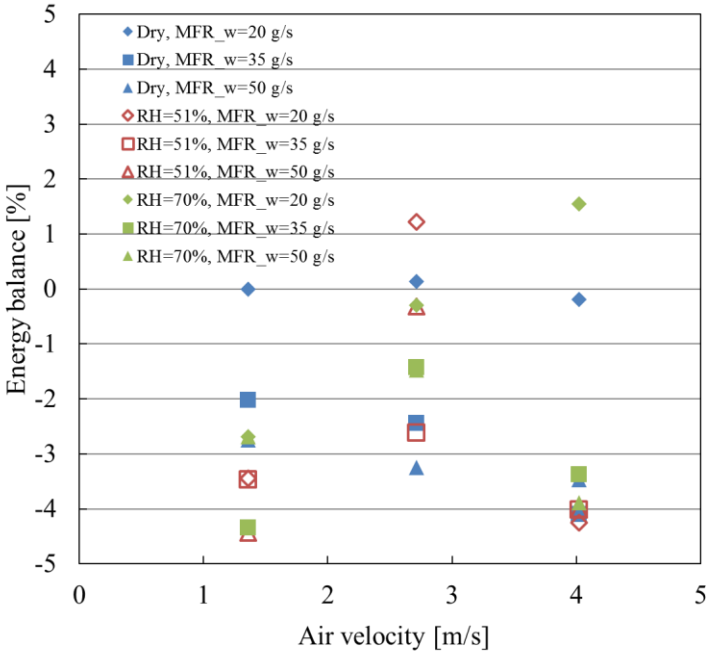

Figure 44 – Vertical Orientation Energy Balance.

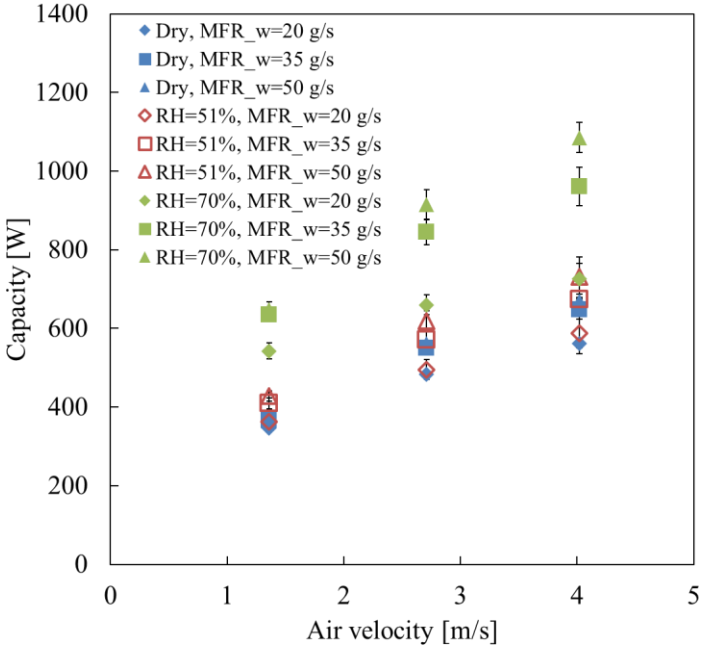

Figure 45 – Vertical Orientation Capacity.

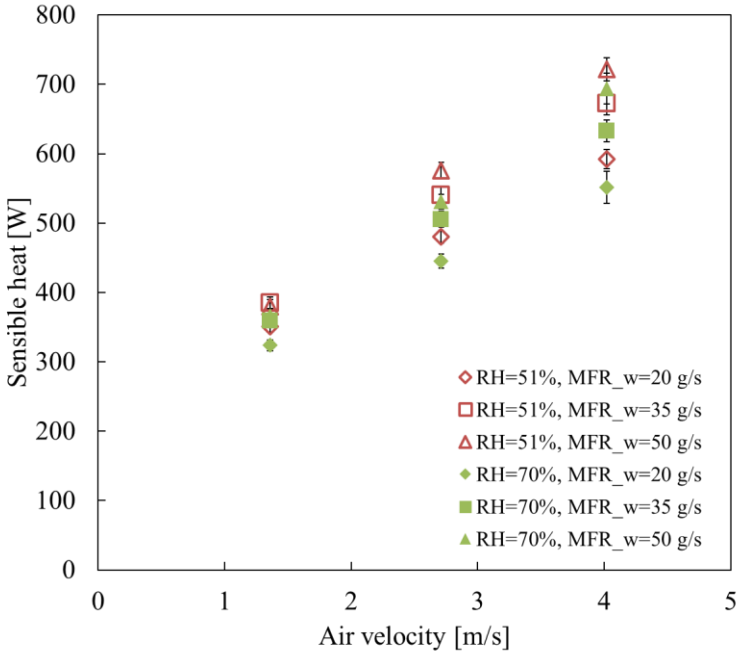

Figure 46 – Vertical Orientation Sensible Heat (Wet Condition).

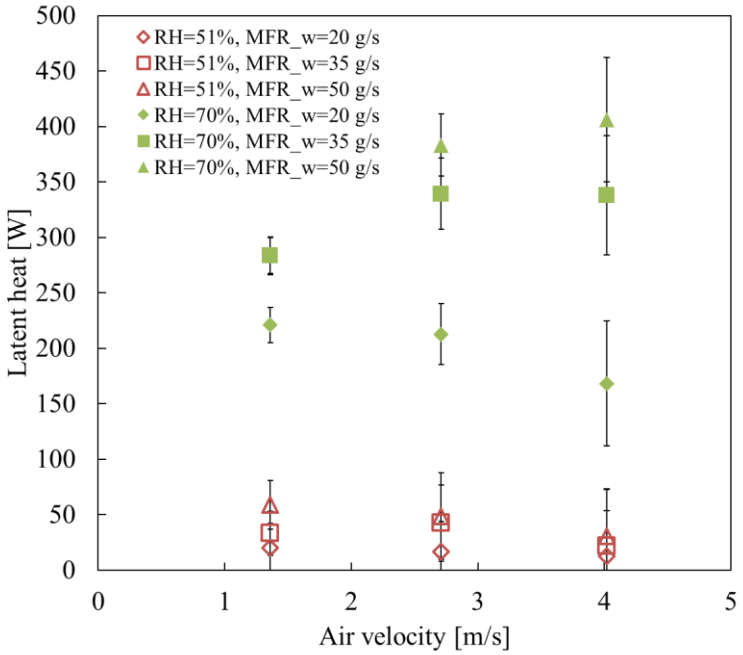

Figure 47 – Verical Orientation Latent Heat (Wet Condition).

Sensible heat ratio is shown in Figure 48. Sensible heat ratio increases as air velocity increases in this range. Airside pressure drop is plotted in Figure 49. Airside pressure drop increases as air flow rate increases. However, air pressure drop is determined by both the air flow rate and the water retention amount on the heat exchanger. Water retention is determined by heat exchanger configuration, water condensing rate, and surface roughness. Water condensing rate is largely related to relative humidity, air flow rate and water

flow rate. Before reaching the maximum water retention amount (cases when inlet air relative humidity is 51%), airside pressure drop is determined simultaneously by air flow rate and water flow rate. Upon reaching maximum water retention amount (cases when inlet air relative humidity is 70%), airside pressure drop is determined mainly by the air flow rate.

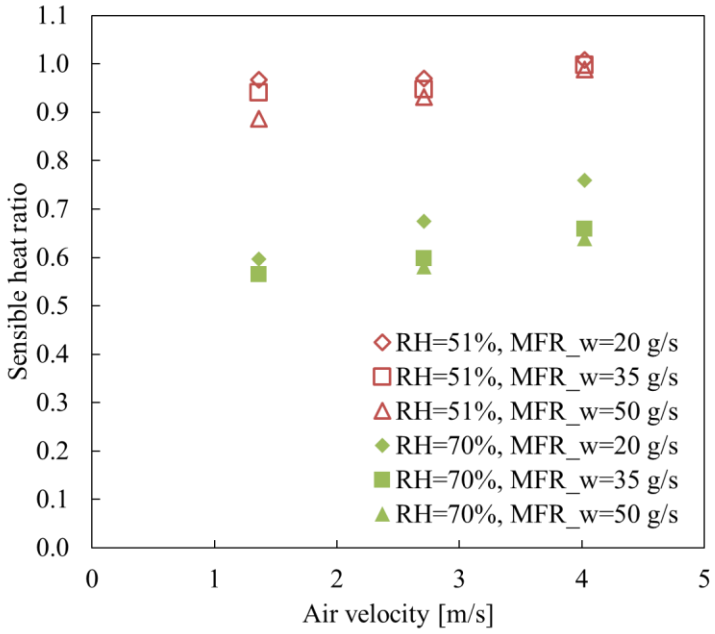

Figure 48 – Vertical Orientation Sensible Heat Ratio (Wet Condition).

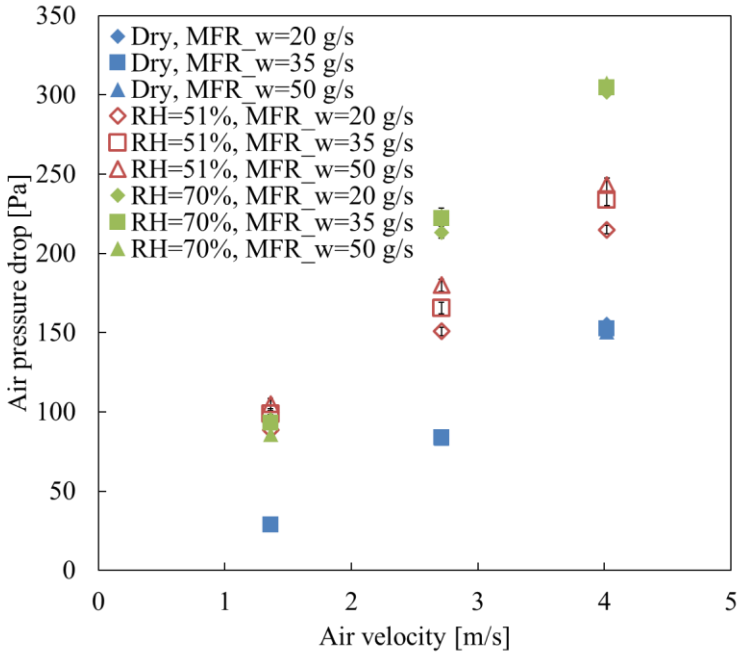

Figure 49 – Vertical Orientation Airside Pressure Drop.

3.3.4 Horizontal Orientation

Horizontal orientation test results are discussed in this section. Total capacity is plotted in Figure 50. Compared to vertical orientation, total capacity of horizontal orientation decreased. Sensible and latent heat are shown in Figure 51 and Figure 52, respectively. Both sensible heat and latent heat of the horizontal orientation are less than that of the vertical orientation. Sensible heat ratio is shown in Figure 53, and Figure 54 shows the airside pressure drop. Pressure drop is higher for horizontal orientation than vertical orientation, indicating that drainage is worse for horizontal orientation. Therefore, vertical orientation is recommended for real application.

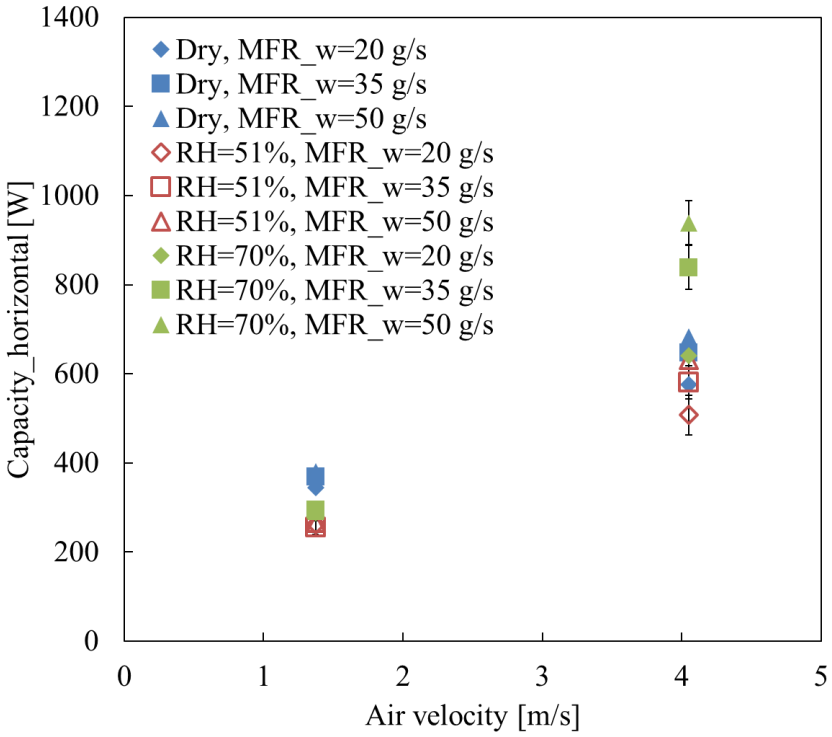

Figure 50 – Horizontal Orientation Capacity.

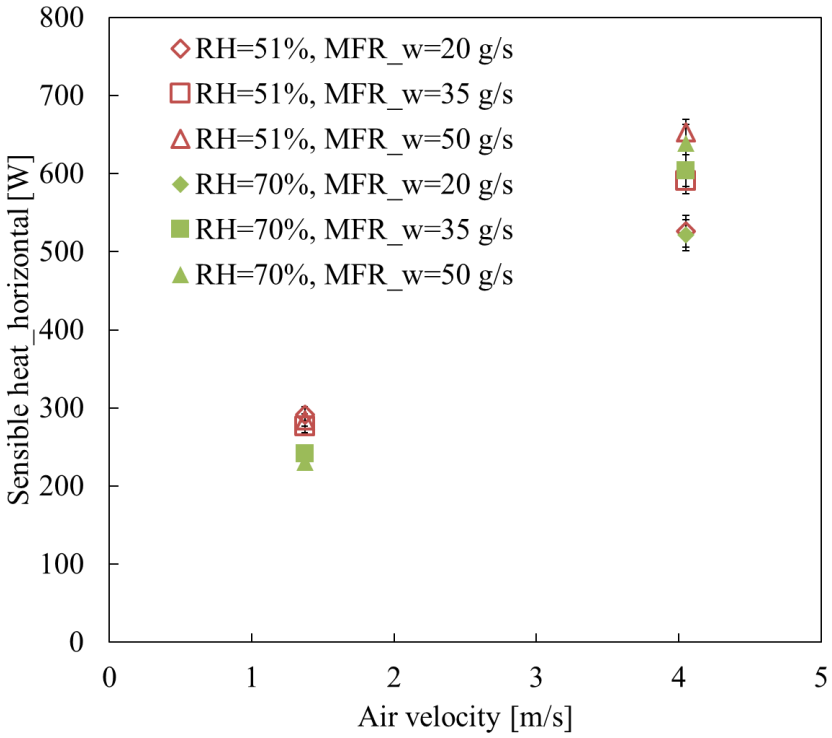

Figure 51 – Horizontal Orientation Sensible Heat (Wet Condition).

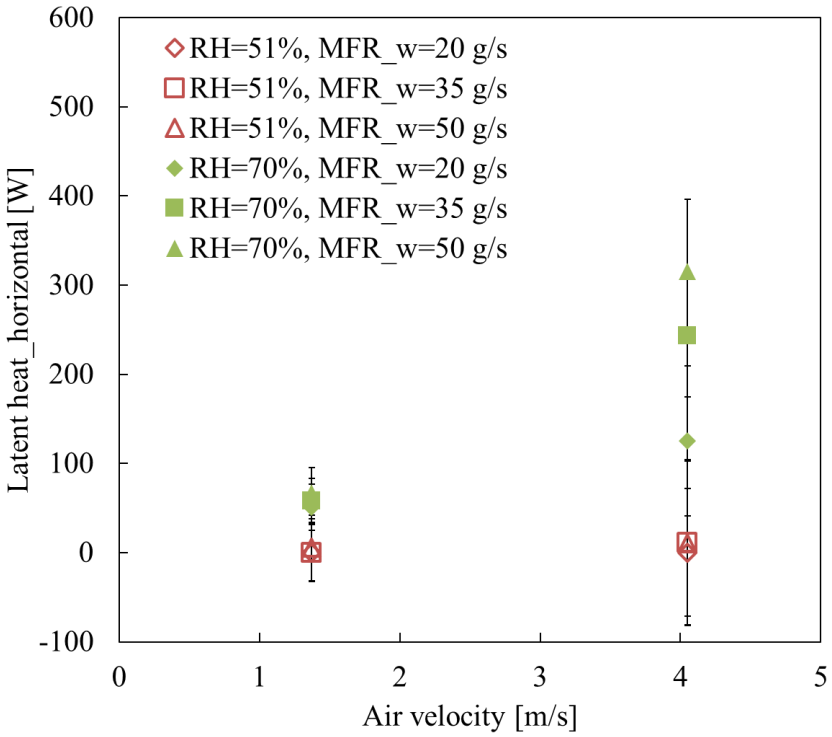

Figure 52 – Horizontal Orientation Latent Heat (Wet Condition).

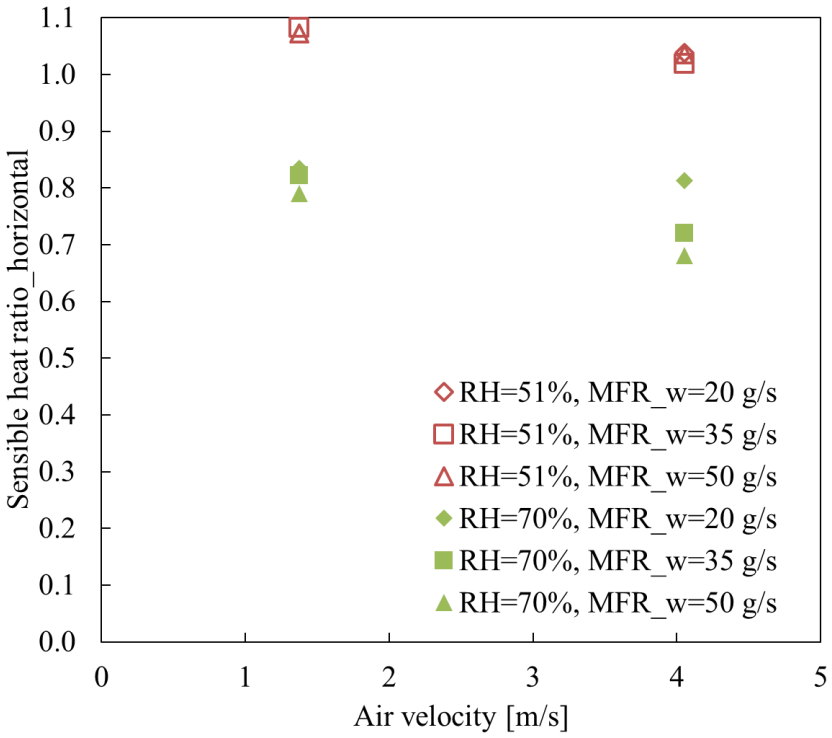

Figure 53 – Horizontal Orientation Sensible Heat Ratio (Wet Condition).

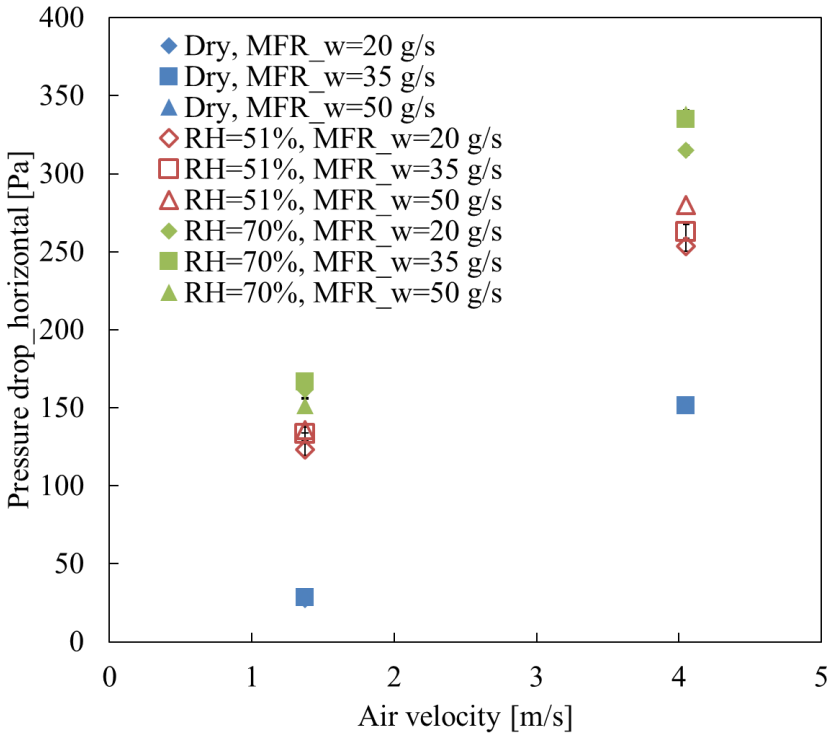

Figure 54 – Horizontal Orientation Airside Pressure Drop Pressure.

3.4 Experimental Validation: 1.0kW Air-to-Water HX

The round bare tube prototypes were tested at the ORNL facilities, and the NURBS bare tube prototype was tested at the University of Maryland facility. Different test metrics were conducted for each HX, as shown below in Table 16. Additional CFD runs were performed to obtain the airside heat transfer coefficient and pressure drop for each case. A full HX simulation in CoilDesigner® [17] was also carried out for each data point to determine predicted capacity. The for capacity and airside pressure drop validation results are shown in Figure 55 and Figure 56, respectively.

Table 16 – 1.0kW Air-to-Water HX Validation Test Results.

Metric		T_{w_in}	T_{w_out}	T_{a_in}	T_{a_out}	MFR_w	VFR_a	u_a	ADP	Q_a	Q_w	EB dev.
HX	Data#	°C	°C	°C	°C	kg/s	m³/s	m/s	Pa	kW	kW	%
BTHX (Cu)	1	67.7	60.2	35.4	49.8	0.0346	0.0602	2.65	96.35	1.074	1.096	2.08
	2	67.6	57.8	35.4	49	0.0247	0.0601	2.65	96.34	1.024	1.025	0.04
	3	67.3	53.1	35.3	47.6	0.015	0.0604	2.66	95.94	0.923	0.897	-2.92
	4	67.2	55.3	34.9	50.3	0.0151	0.0403	1.78	50.42	0.77	0.756	-1.86
	5	67.4	59.4	35	51.8	0.0249	0.04	1.76	50.19	0.835	0.834	-0.12
	6	67.8	61.9	35.4	52.8	0.0353	0.04	1.76		0.866	0.885	2.10
BTHX (SS)	1	67.2	58.9	35.3	51.7	0.035	0.0603	2.66	93.35	1.232	1.22	-1.00
	2	67.2	56.2	35.2	50.9	0.025	0.0601	2.65	92.76	1.17	1.144	-2.33
	3	67.2	51.2	35.2	49.2	0.015	0.06	2.64	91.37	1.042	1.005	-3.64
	4	67.2	53.6	35.1	52.6	0.0149	0.0401	1.77	48.56	0.872	0.849	-2.70
	5	67.4	58.4	35.1	54.5	0.025	0.0398	1.75	49.06	0.962	0.938	-2.49
	6	67.5	60.7	35.1	55.4	0.0351	0.0399	1.76	48.56	1.003	0.997	-0.59
NTHX (Ti)	1	50.6	43	8.62	27.66	0.0346	0.0478	2.11	147.6	1.115	1.103	-1.09
	2	40.7	35.1	8.6	23.51	0.0361	0.0474	2.09	144.5	0.864	0.842	-2.61

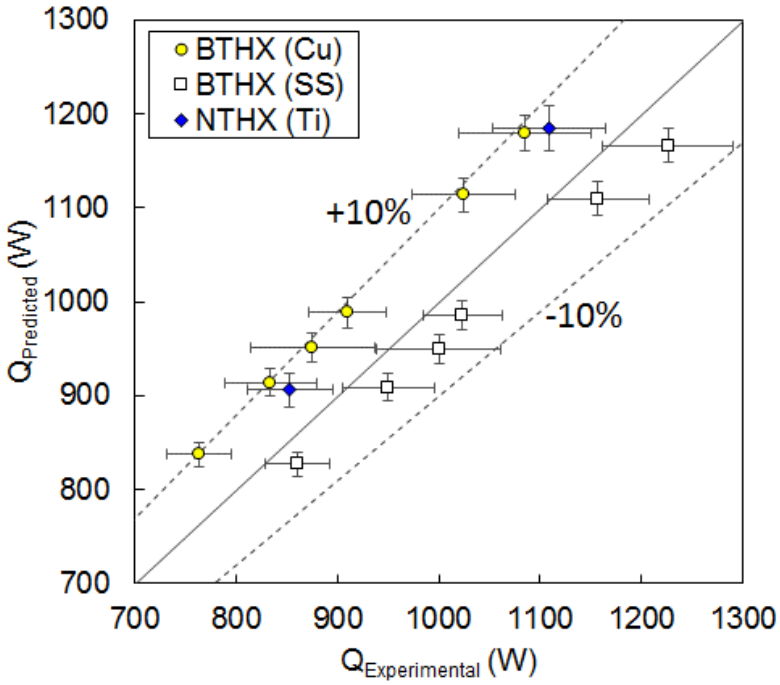

Figure 55 – Experimental Validation: Capacity.

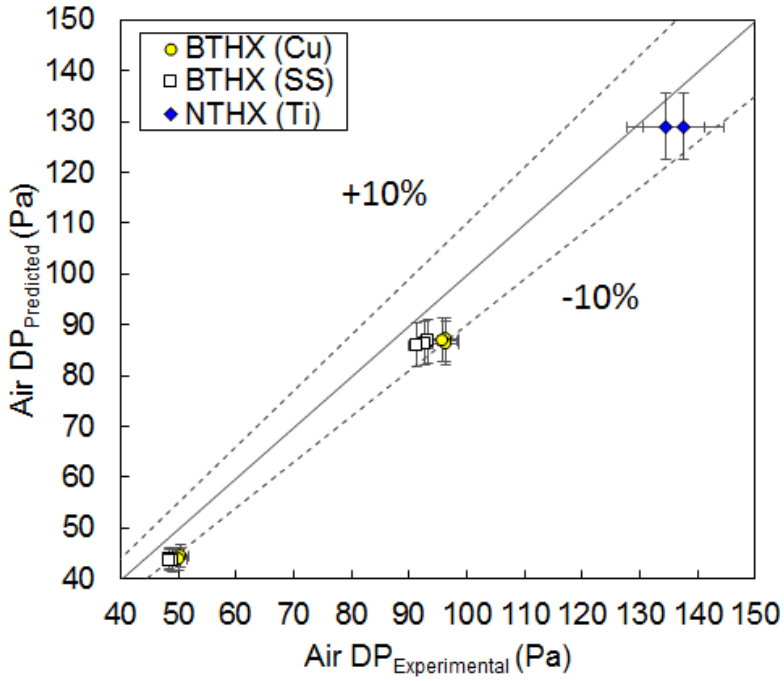

Figure 56 – Experimental Validation: Airside Pressure Drop.

3.5 10 kW BTHX

3.5.1 Blockage Test and Cleaning

The 10kW BTHX is made of 2280 copper tubes and shown in Figure 57.

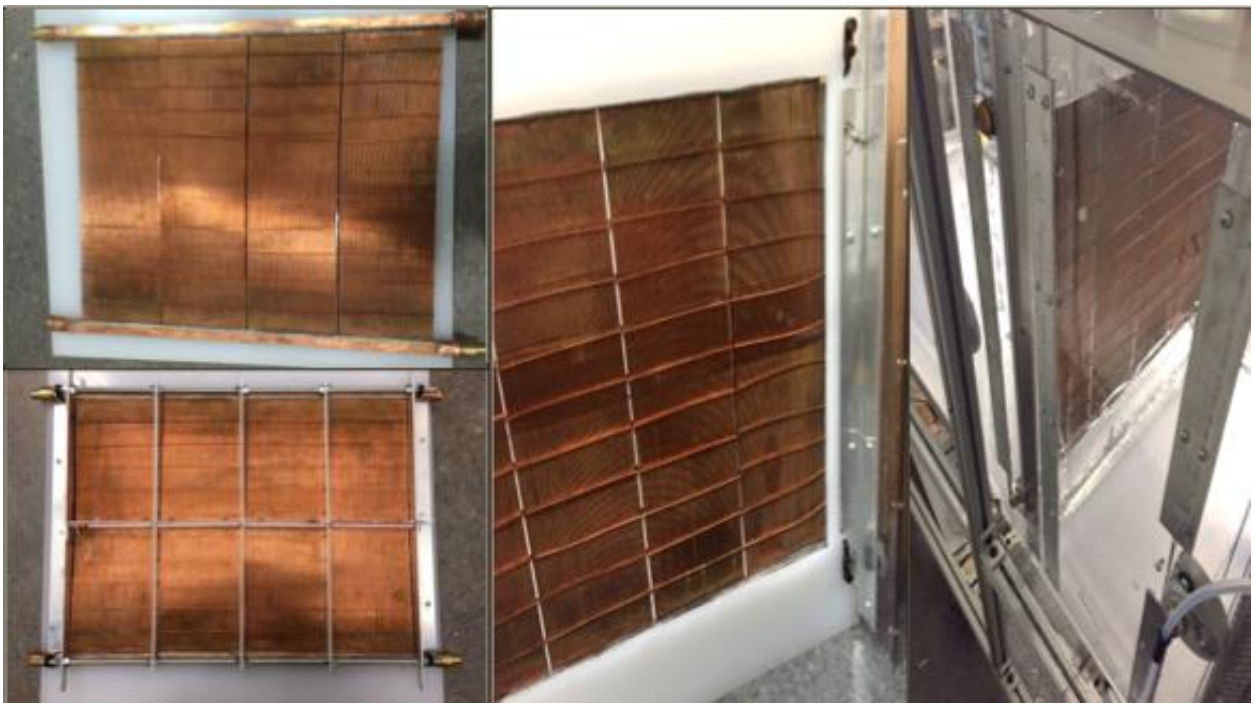

Figure 57 – 10 kW HX.

A blockage test was conducted on the 10kW HX to assess the flow. Hot water was drawn through the HX, and an infrared camera was used to see any blockages. The results of the blockage test is shown in Figure 58. The darker areas indicate no flow in the tube. By estimation, about 20-35% of tubes are blocked.

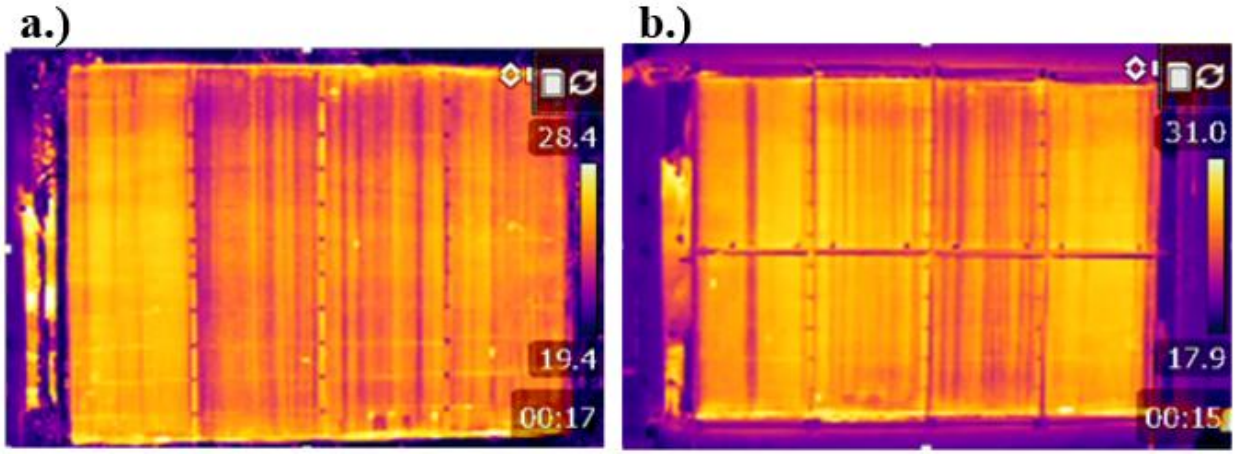

Figure 58 – Blockage Test before Cleaning: (a) Front View; (b) Back View.

Following blockage testing, the 10kW HX was sent back to Heat Transfer Technologies for wire cleaning. A second blockage test was conducted utilizing the same procedure to see whether the blockage issue was addressed. The results are shown in Figure 59. The darker areas again indicate no tube flow. It should be noted that while the flow pattern changed after cleaning, blockages are still present. The blockage area actually increased after cleaning; this can be seen by comparing HX performance in the following sections.

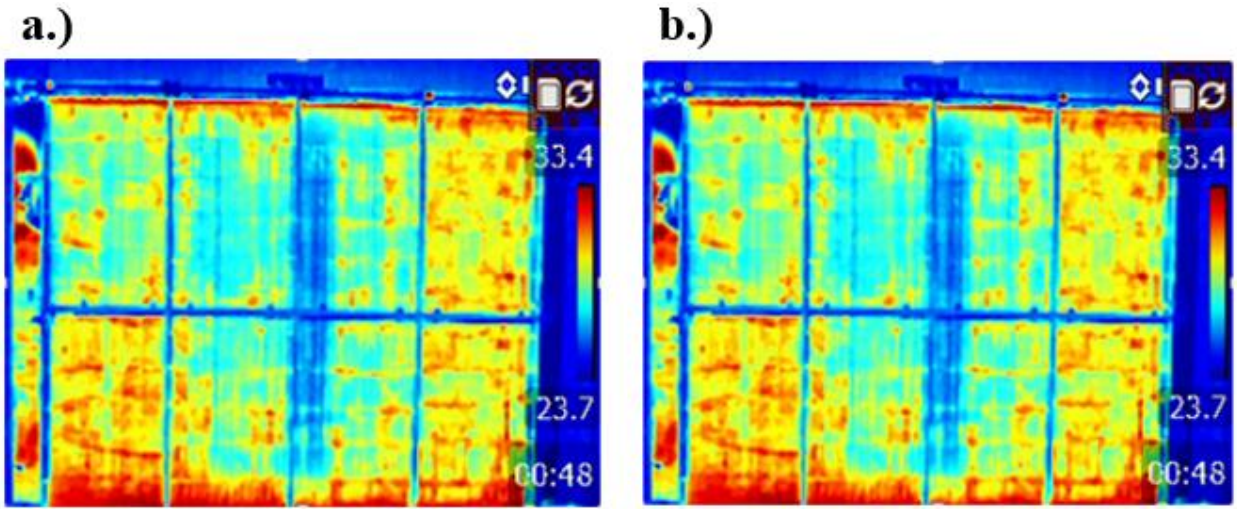

Figure 59 – Blockage Test after Cleaning: (a) Front View; (b) Back View.

3.5.2 Dry Condition Results, Pre-Cleaning

Prior to the wire cleaning for blockages, the 10kW HX was tested under dry conditions. The dry condition test matrix is shown in Table 17. The 10kW HX was tested for three air flow rates and five mass flow rates.

Table 17 – Pre-Cleaning Dry Condition Test Matrix.

Fluid	Property	Value	Unit
Air	Inlet air temperature	30.0 ± 0.3	°C

	Inlet air RH	6 ± 1	%
	Air flow rate	0.16 ± 0.0016	m^3/s
		0.31 ± 0.0031	m^3/s
		0.47 ± 0.0047	m^3/s
Water	Inlet water temperature	55.0 ± 0.6	°C
	Water mass flow rate	71 ± 0.71	g/s
		95 ± 0.95	g/s
		118 ± 1.18	g/s
		141 ± 1.41	g/s
		165 ± 1.65	g/s

The energy balance results are shown in Figure 60. Capacity and airside pressure drop are shown in Figure 61 and Figure 62, respectively. The HX capacity increases non-linearly as air velocity increases and water velocity increases. The gradient of heat exchanger capacity over air velocity, i.e., the slope of the trend line, decreases as the air flow rate increases and increases as water flow increases at a given air velocity. This is because when air flow rate increases or water flow decreases, the portion of airside thermal resistance decreases, so the influence of air velocity on capacity diminishes, and vice versa.

The gradient of HX capacity over water velocity can be seen by comparing the trend line discrepancy in Figure 61. The gradient decreases as water flow rate increases and increases as air flow rate increases. Similar reasoning could be used to explain this, i.e., when water flow rate increases or air flow rate decreases, the portion of water side thermal resistance decreases, reducing the influence of water flow rate on capacity. The HX airside pressure drop increases non-linearly with the increase of air velocity, and the slope increases as air velocity increases. This is since higher air velocity increases frictional losses. The change in water flow rate causes air density to change, resulting in a different airside pressure drop; however, this change is not significant.

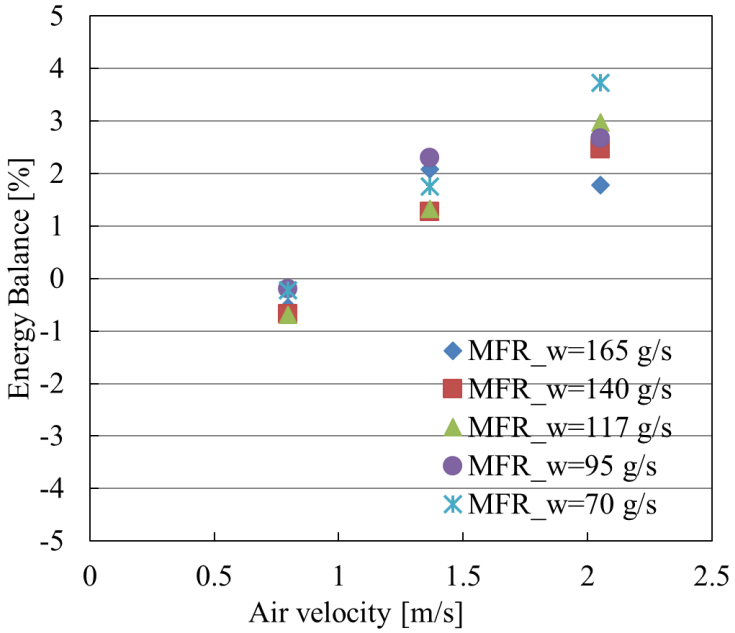

Figure 60 – 10kW HX Energy Balance, Pre-Cleaning, Dry Condition.

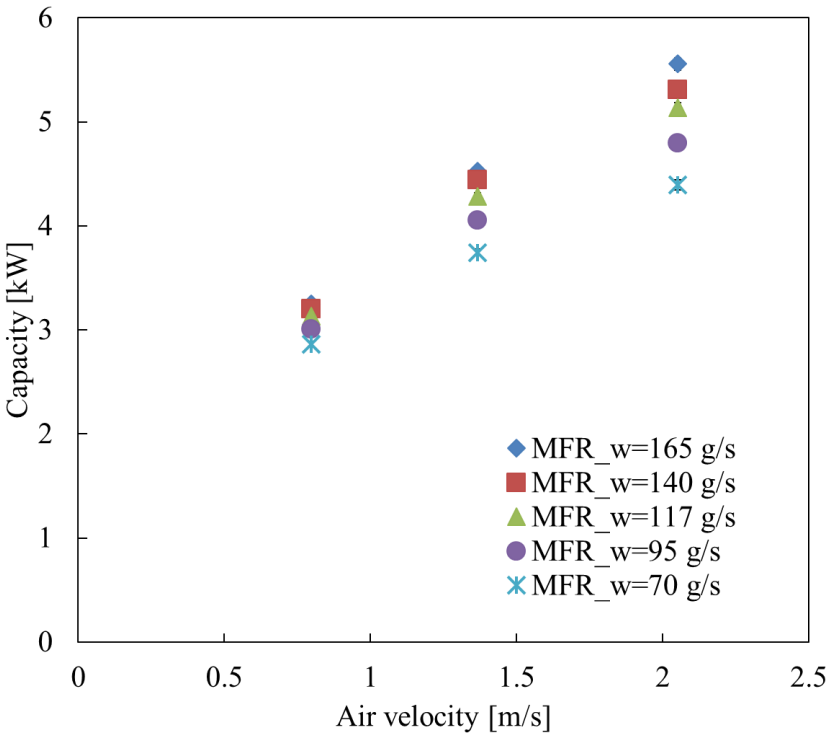

Figure 61 – 10kW HX Capacity, Pre-Cleaning, Dry Condition.

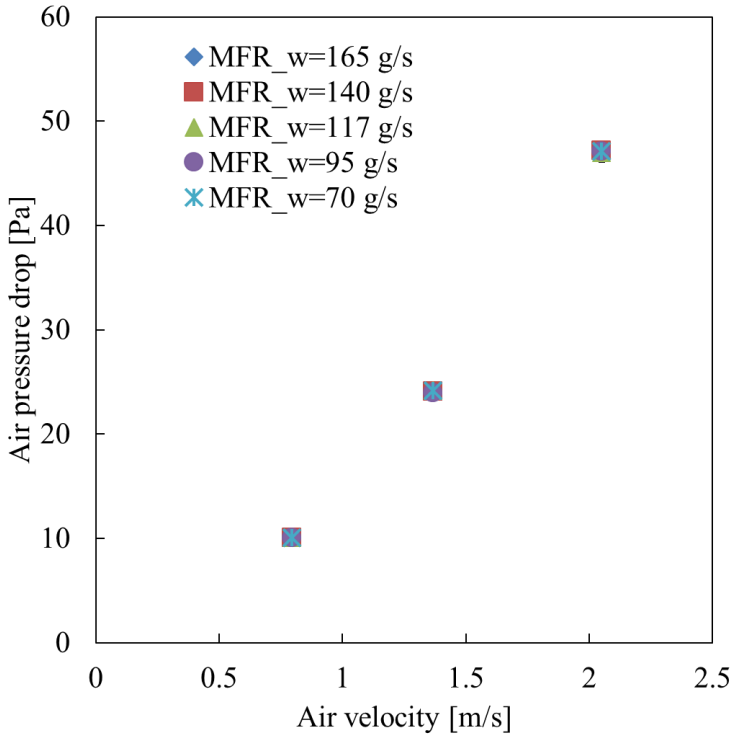

Figure 62 – 10kW HX Airside Pressure Drop, Pre-Cleaning, Dry Condition.

3.5.3 Dry Condition Results, Post-Cleaning

Following the cleaning of the 10kW HX, another dry condition test was performed. The test matrix for the post-cleaning test is shown in Table 18. The post-cleaning test used three air flow rates and water mass flow rates each.

Table 18 – Post-Cleaning Dry Condition Test Matrix.

Fluid	Property	Value	Unit
Air	Inlet air temperature	20.0 ± 0.3	°C
	Inlet air RH	6 ± 1	%
	Air flow rate	0.16 ± 0.0016	m^3/s
		0.31 ± 0.0031	m^3/s
		0.47 ± 0.0047	m^3/s
Water	Inlet water temperature	63.0 ± 0.6	°C
	Water mass flow rate	140	g/s
		235	g/s
		330	g/s

The energy balance results are shown in

Figure **63**. Capacity and airside pressure drop are shown in Figure 64 and Figure 65, respectively. The HX capacity increases non-linearly as air velocity increases and water velocity increases. The gradient of heat exchanger capacity over air velocity, i.e., the slope of the trend line, decreases as the air flow rate increases and increases as water flow increases at a given air velocity. This is because when air flow rate increases or water flow decreases, the portion of airside thermal resistance decreases, so the influence of air velocity on capacity diminishes, and vice versa.

The gradient of HX capacity over water velocity, can be seen by comparing the trend line discrepancy in Figure 65. The gradient decreases as water flow rate increase and increases as air flow rate increases. Similar reasoning could be used to explain this, i.e., when water flow rate increases or air flow rate decreases, the portion of water side thermal resistance decreases, reducing the influence of water flow rate on capacity. The HX airside pressure drop increases non-linearly with the increase of air velocity, and the slope increases as air velocity increases. This is since higher air velocity increases frictional losses. The change in water flow rate causes air density to change, resulting in a different airside pressure drop; however, this change is not significant.

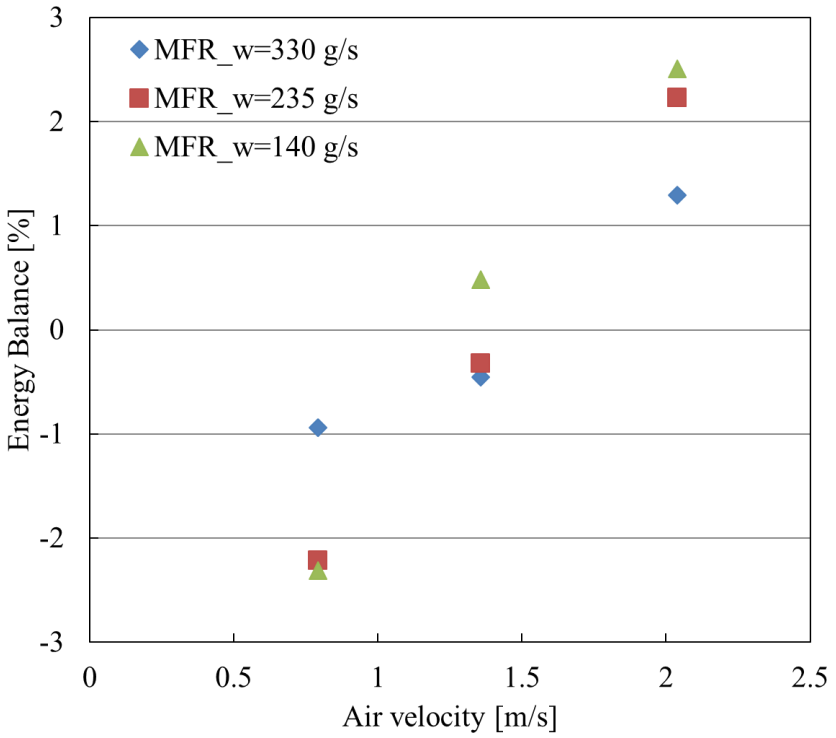

Figure 63 – 10kW HX Energy Balance, Post-Cleaning, Dry Condition.

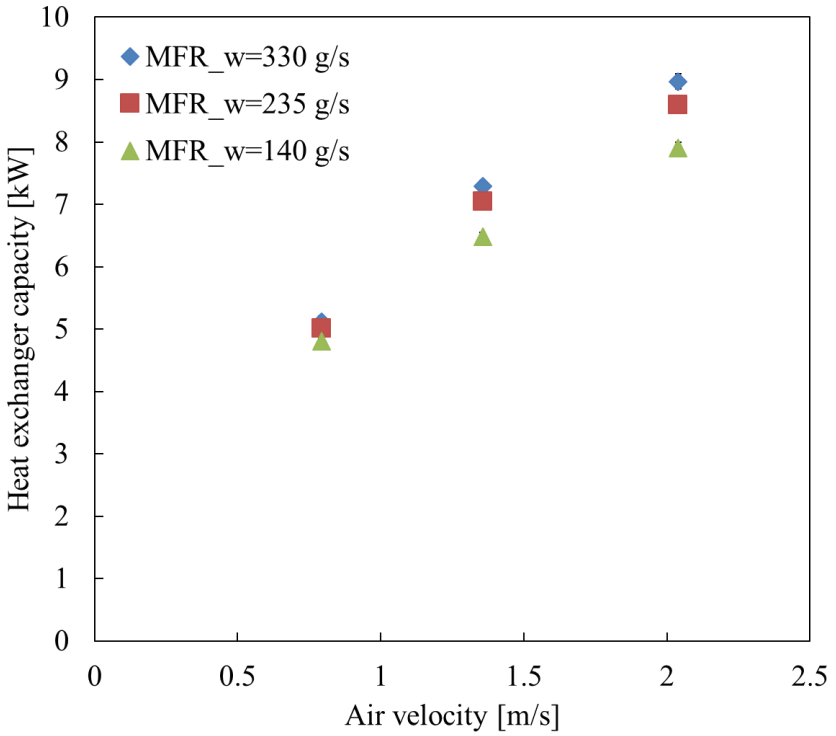

Figure 64 – 10kW HX Capacity, Post-Cleaning, Dry Condition.

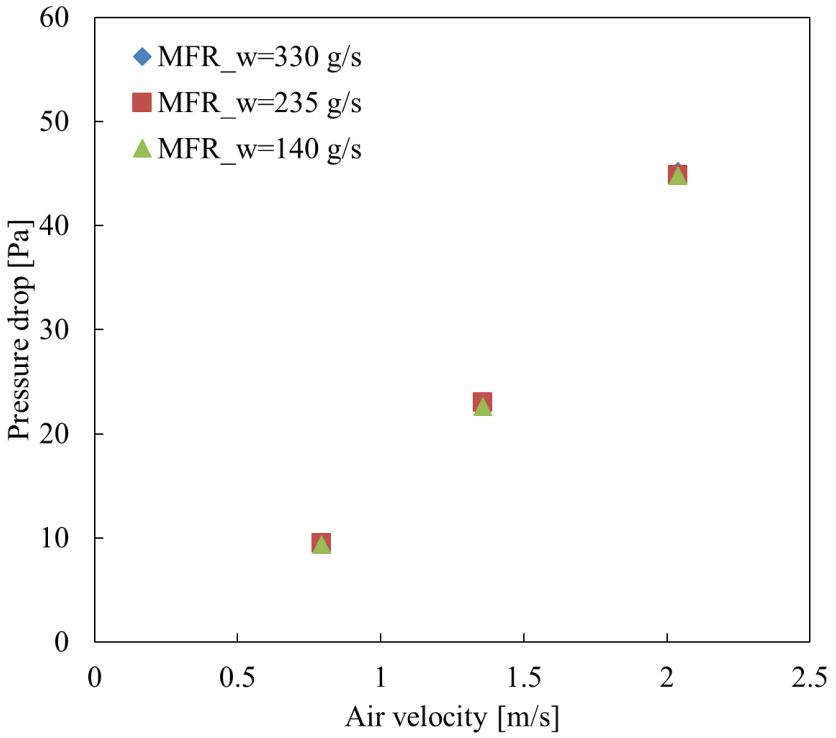

Figure 65 – 10kW HX Airside Pressure Drop, Post-Cleaning, Dry Condition.

3.5.4 Dry Condition Results, Comparison, Pre- and Post-Cleaning

The airside heat transfer coefficient results before and after cleaning are shown in Figure 66 and Figure 67, respectively. As previously noted, the cleaning resulted in more HX blockage. Therefore, the airside heat transfer coeffients presented here are not accurate, as the heat transfer area is over-estimated. The figures are shown to present the effects of the wire cleaning.

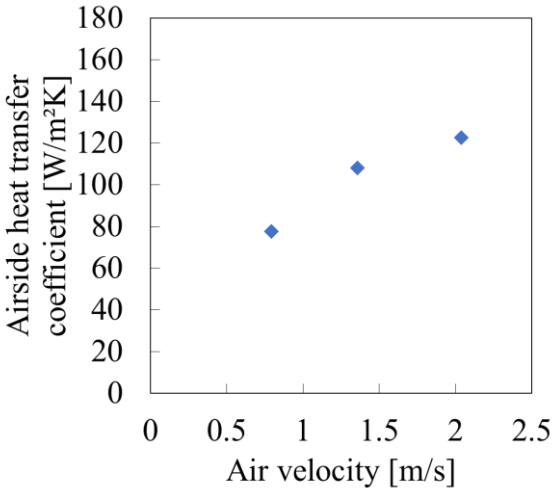

Figure 66 – Air HTC, Pre-Cleaning.

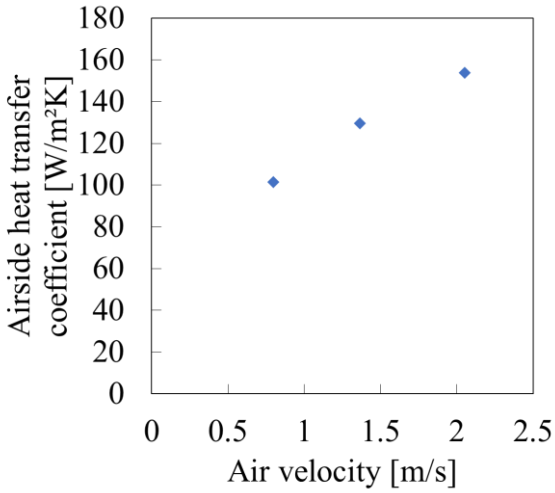

Figure 67 – Air HTC, Post-Cleaning.

The airside pressure drops for 10kW HX before and after cleaning are shown in Figure 68 and Figure 69, respectively. As expected, airside pressure drops are the same at the same air flow rate.

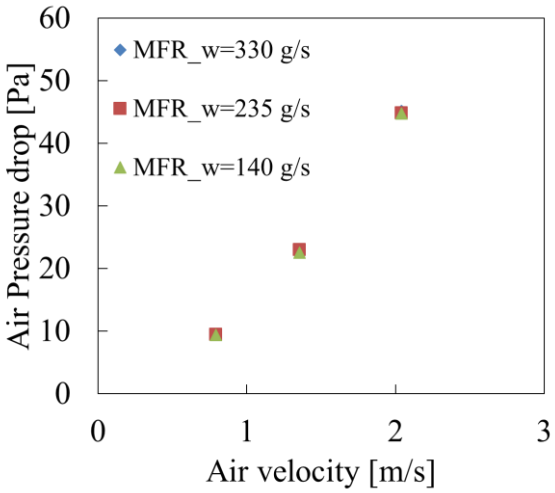

Figure 68 – Airside Pressure Drop, Pre-Cleaning.

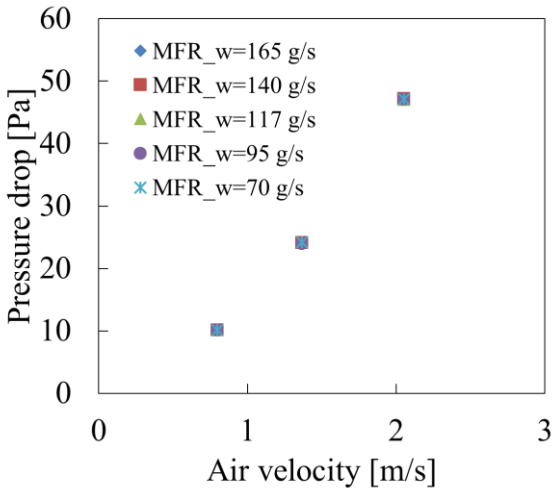

Figure 69 – Airside Pressure Drop, Post-Cleaning.

3.5.5 Dry Condition Results Comparsion, Experimental and Simulation

The experimental data is compared with simulation results from a CoilDesigner® [17] model of the 10kW HX. The results are summarized in Figure 70 through Figure 73. Due to the blockage, the heat transfer capability of this prototype suffers noticeable degradation. Airside heat transfer coefficient and UA values are also not accurate since the actual heat transfer area cannot be accurately calculated due to the blockage. Therefore, the next step should be improving manufacturing methodology to solve the blockage problem.

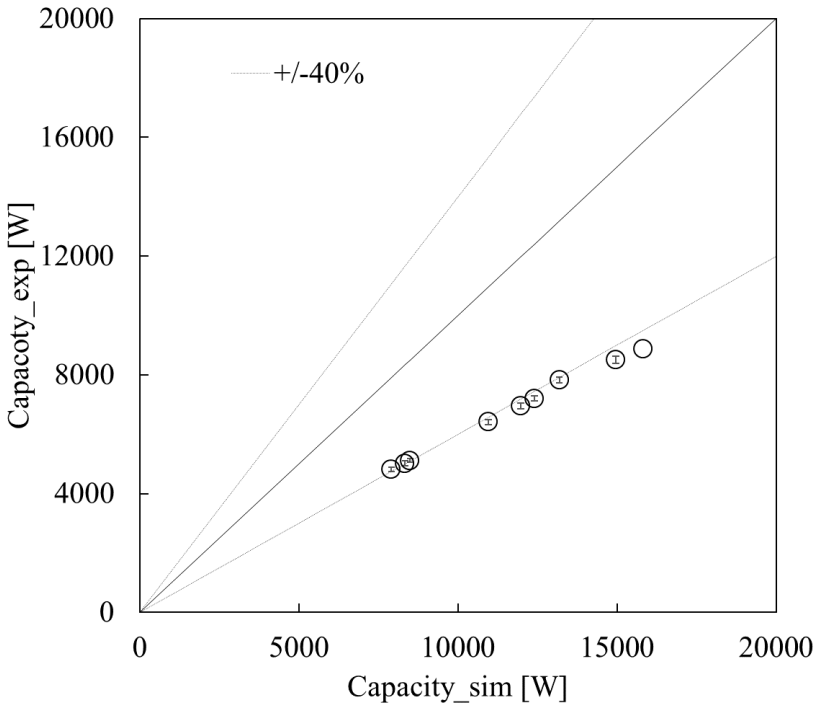

Figure 70 – 10kW HX Capacity, Experiments and Simulations Comparison.

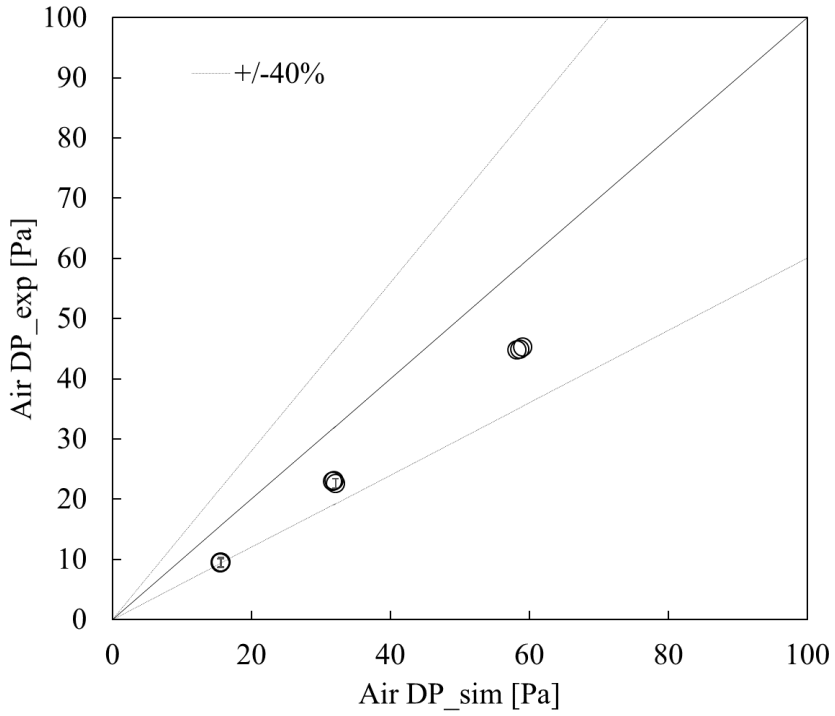

Figure 71 – 10kW HX Airside Pressure Drop, Experiments and Simulations Comparison.

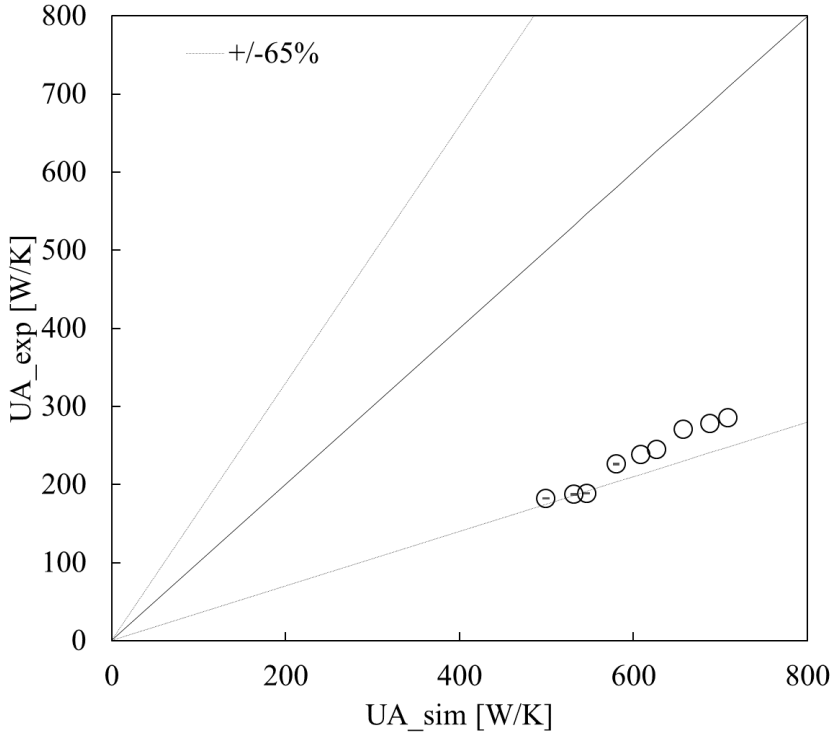

Figure 72 – 10kW HX UA Value, Experiments and Simulations Comparison.

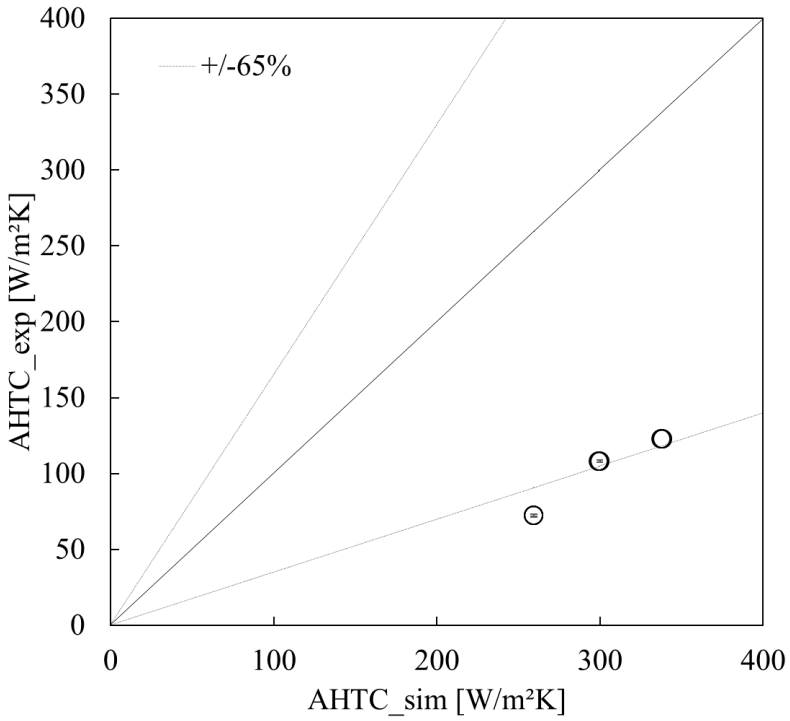

Figure 73 – 10kW HX Air HTC, Experiments and Simulations Comparison.

3.6 WTHX Concept

A prototype of a webbed-tube heat exchanger (WTHX) was designed and tested, as shown in Figure 74. The prototype consists of 13 fins with 6 tubes in each fin. Dimensions of the tubes and fins are shown in Figure 75.

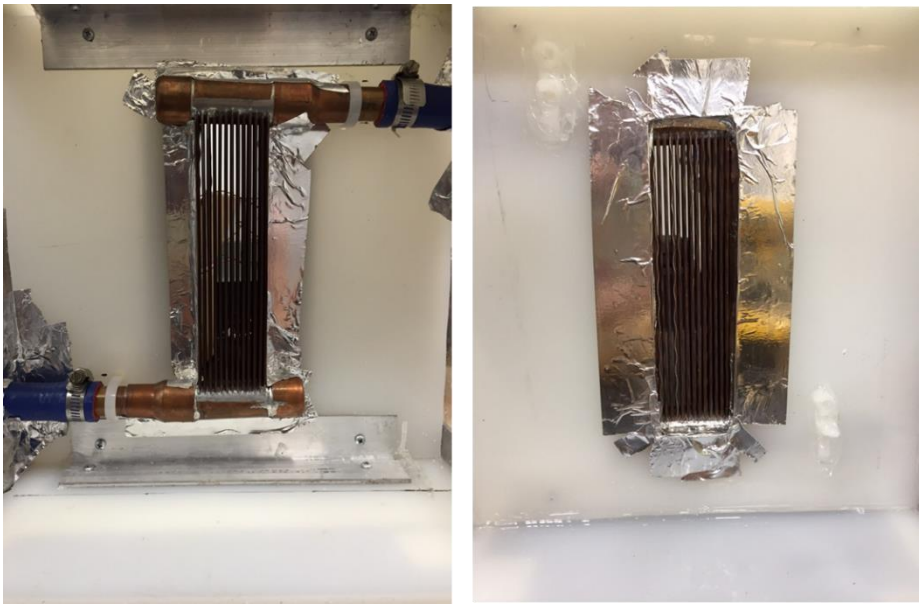

Figure 74 – WTHX.

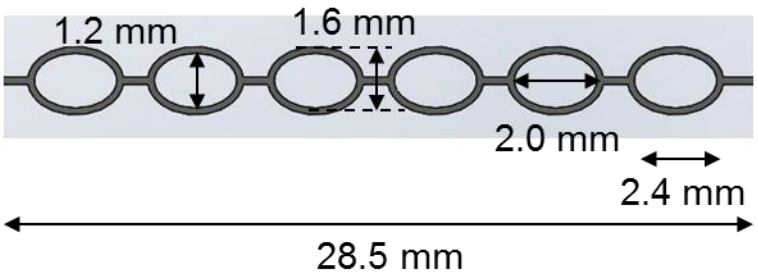

Figure 75 – WTHX Dimensions.

Three water flow rates and five air flow rates were tested. Results are shown in Figure 76 and Figure 77.

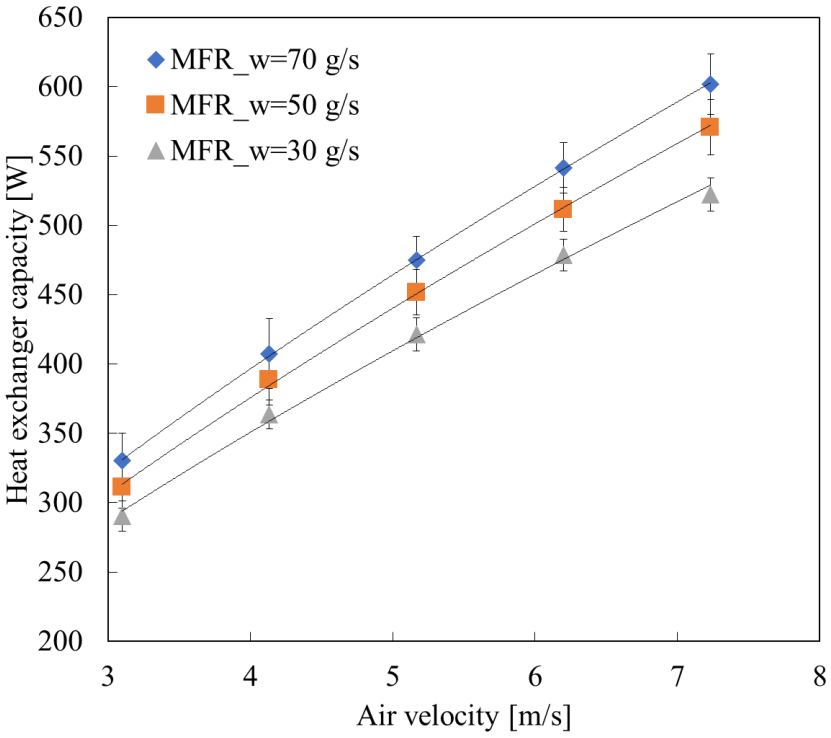

Figure 76 – WTHX Capacity.

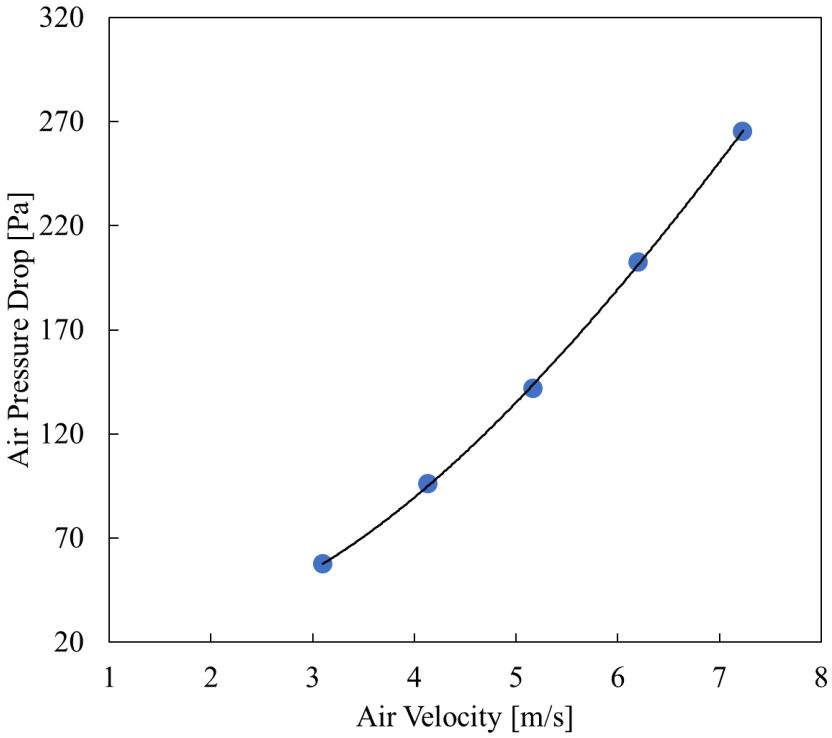

Figure 77 – WTHX Airside Pressure Drop.

Wilson plot method was applied to WTHX. Results are shown in Figure 78.

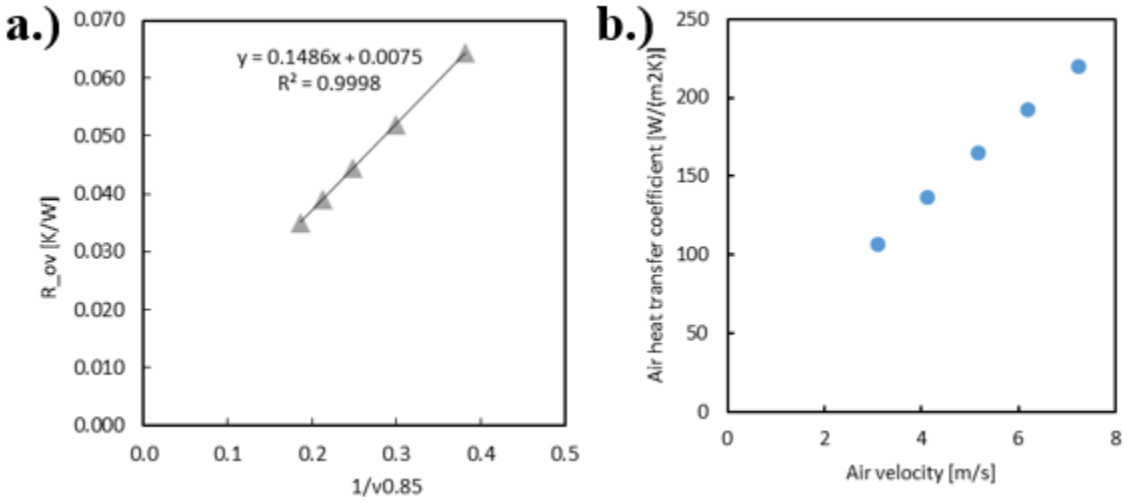

Figure 78 – a.) WTHX Wilson Plot; b.) Air HTC.

For this design, an airside heat transfer coefficient and velocity correlation could be developed from the methodology in Chapter 3.2.1 as Eq. (39):

$$h = 41v^{0.85}; \quad 3.1 \le v \le 7.2\ m/s \tag{39}$$

3.7 Uncertainty Analysis

Total uncertainty of measured parameters is the sum of systematic error and random error for each sensor. Systematic error for each sensor is summarized in .

Table 19. Random error is calculated as standard deviation of the measured value.

Table 19 – Instrument Systematic Error.

Temperature Sensor				
Type	Company	Product	Accuracy	
TC			0.5 °C	
RTD	Omega	PR-25AP series	Class 1/10	
			-10 °C	0.03 °C
			0 °C	0.03 °C
			10 °C	0.04 °C
			20 °C	0.04 °C
			30 °C	0.05 °C
			40 °C	0.06 °C
			50 °C	0.07 °C
Dew Point Hygrometer				
Type	Company	Product	Dew Point Accuracy	
Chilled mirror hygrometer	EdgeTech	DewTrak II Chilled Mirror Transmitter	± 0.2°C dew/frost point	
Pressure Sensor-across Nozzle				
Type	Company	Product	Accuracy	
Differential	Setra	2641005WD11T1F	(+/-0.25%FS) ± 3Pa	
Barometric	Setra	2781600MA1B2BT1	0-40℃	±100Pa
			‘-20 to 50 ℃	±150Pa
			’-40 to 60 ℃	±200Pa
Pressure Sensor-across HX				
Type	Company	Product	Accuracy	
Differential	Setra	2641001WD11T1F	(+/-0.25%FS) ± 0.62Pa	
Barometric	Setra	2781899MA1B2BT1	0-40℃	±60Pa
			‘-20 to 50 ℃	±100Pa
			’-40 to 60 ℃	±150Pa
Measurement of Nozzle Diameter and Duct Diameter				
Type			Accuracy	
ASHRAE standard nozzle			0.001D	

Total uncertainty of calculated parameters is determined by error propagation with total uncertainties of directly measured parameters as in Eq. (40):

$$\omega_f = \sqrt{\left(\frac{\partial f}{\partial x_1}\omega_{x_1}\right)^2 + \left(\frac{\partial f}{\partial x_2}\omega_{x_2}\right)^2 + \cdots + \left(\frac{\partial f}{\partial x_n}\omega_{x_n}\right)^2} \tag{40}$$

3.8 Lessons Learned

The test procedures for all HX’s followed ASHRAE standards [22]. However, several items must be considered because of the unique intrinsic characteristics of bare tube HX’s with such small diameters and different capacities. The following is a brief discussion of lessons learned during this test procedure:

- The fluid flowing in the tubes must be deionized water or filtered water to avoid potential blockages caused by dirt particles in the fluid.
- Ideally, the test facility should be built in a chamber with an air conditioning unit that can keep room temperature constant to minimize heat losses from the wind tunnel. Duct and water pipe insulation should be sufficient to reduce heat loss from both sides. Otherwise, a heat leakage correction test should be conducted following the ASHRAE 41.2 [23]. The above efforts are to ensure an energy balance within ± 5.0%.
- To ensure that the capacity and pressure drop uncertainties are within ±5.0%, instruments with proper accuracy should be selected. However, cost must also be considered. Meanwhile, proper temperature and flow rate control should be utilized to reduce random errors.
- Temperature difference for water side must be sufficiently large, otherwise the uncertainty will not be acceptable. However, the water flow rate must also be small enough to guarantee a sufficient water temperature difference. Minimum recommended temperature difference is 2°C.
- The ratio of duct size and HX frontal area have an impact on air flow measurement. Ideally, the duct size should be the same as the HX size. However, a slightly larger duct is acceptable. If the ratio is too high, i.e., the duct is oversized, then the air flow will be reduced upstream and downstream of the duct, resulting in more heat loss. Further, the local pressure losses due to expansion and contraction will no longer be negligible. The maximum recommended ratio is 5.

4 CFD-Based Correlation Development

The purpose of this task is to leverage the analysis capability developed in the other tasks to develop airside performance correlations for small diameter tube heat exchangers. Such correlations can then be used by engineers in industry to design novel heat exchangers. The correlation development requires 2000+ CFD simulations and iterative data fitting. All correlations are currently available in the latest version of CoilDesigner® [17], which is currently capable of evaluating coils with small diameter tubes. A summary of the developed correlations and their accuracies is shown in Table 20.

Table 20 – CFD-Based Correlations (taken from D. Bacellar Ph.D. Dissertation Defense).

	Fin type	Tube arrangement	Application range	Accuracy (staggered only)
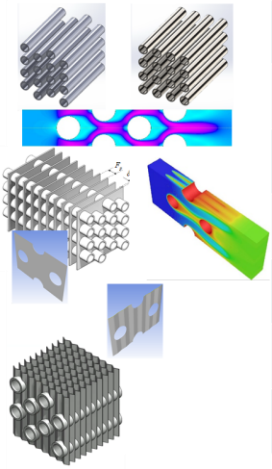	Finless	Staggered	0.5mm≤Do≤2.0mm 2≤N≤40	j : 15%(92.9% of data) f: 15% (88.1% of data)
	Finless	In-line	0.5mm≤Do≤2.0mm 2≤N≤40	j : 20%(80% of data) f: 20%(80% of data)
	Finless	Staggered	2.0mm≤Do≤5.0mm 2≤N≤20	j : 10%(98.5% of data) f: 10%(91.9% of data)
	Flat	Staggered	2.0mm≤Do≤5.0mm 2≤N≤20	j : 15%(82.1% of data) f: 15% (82.3% of data)
	Wavy Herringbone	Staggered	2.0mm≤Do≤5.0mm 2≤N≤20	Nu: 15%(96% of data) Cf: 15%(94% of data)
	Wavy Smooth	Staggered	2.0mm≤Dc≤5.0mm 2≤N≤10	j : 20%(64% of data) f: 20% (66% of data)
	Wavy Smooth	Staggered	2.0mm≤Do≤5.0mm 2≤N≤20	Nu: 15%(94% of data) Cf: 15%(93% of data)

5 List of Publications

D. Bacellar, V. Aute, O. Abdelaziz, R. Radermacher, **Design of Novel Air-to-Refrigerant Heat Exchangers Using Approximation Assisted Optimization**, in *ASME 2014 Verification & Validation Symposium*, Las Vegas, NV, USA, May 7-9, 2014.

D. Bacellar, V. Aute, R. Radermacher, **CFD-Based Correlation Development for Air Side Performance of Finned and Finless Tube Heat Exchangers with Small Diameter Tubes**, *15th International Refrigeration and Air Conditioning Conference*, Purdue University, West Lafayette, IN, USA, July 14-17, 2014.

D. Bacellar, J. Ling, O. Abdelaziz, V. Aute, R. Radermacher, **Multi-Scale Modeling and Approximation Assisted Optimization of Bare Tube Heat Exchangers**, *Proceedings of the 15th International Heat Transfer Conference, IHTC-15*, Kyoto, Japan, August 10-15, 2014.

K. Saleh, D. Bacellar, V. Aute, R. Radermacher, **An Adaptive Multiscale Approximation Assisted Multiobjective Optimization Applied to Compact Heat Exchangers**, *4th International Conference on Engineering Optimization, EngOpt*, Lisbon, Portugal, September 8-11, 2014.

D. Bacellar, O. Abdelaziz, V. Aute, R. Radermacher, **Novel Heat Exchanger Design using Computational Fluid Dynamics and Approximation Assisted Optimization**, *ASHRAE 2015, Winter Conference*, Chicago, IL, USA, January 24-28, 2015.

D. Bacellar, V. Aute, R. Radermacher, **A Method for Air-To-Refrigerant Heat Exchanger Multi-Scale Analysis and Optimization with Tube Shape Parameterization**, *24th IIR International Congress of Refrigeration*, Yokohama, Japan, August 16-22, 2015.

D. Bacellar, V. Aute, R. Radermacher, **CFD-Based Correlation Development for Air Side Performance on Finned Tube Heat Exchangers with Wavy Fins and Small Tube Diameters**, *24th IIR International Congress of Refrigeration*, Yokohama, Japan, August 16-22, 2015.

D. Bacellar, V. Aute, Z. Huang, R. Radermacher, **Multi-Scale Analysis and Shape Optimization Method for High Performance Compact Air-to-Fluid Heat Exchangers Design** (Submitted to the *International Journal of Heat and Mass Transfer*).

D. Bacellar, V. Aute, R. Radermacher, **Novel Airside Heat Transfer Surface Designs using an Integrated Multi-Scale Analysis with Topology and Shape Optimization**, *16th International Refrigeration and Air Conditioning Conference*, Purdue University, West Lafayette, IN, USA, July 11-14, 2016.

D. Bacellar, V. Aute, Z. Huang, R. Radermacher, **Airside Performance Correlations and Optimal Heat Pump Heat Exchanger Designs Based on 0.5mm-2mm Finless Round Tube Bundles**, *16th International Refrigeration and Air Conditioning Conference*, Purdue University, West Lafayette, IN, USA, July 11-14, 2016.

D. Bacellar, V. Aute, R. Radermacher, **Performance Evaluation Criteria Analysis of Compact Air-to-Refrigerant Heat Exchangers and Selection Utility Function for Single Phase Applications**, *16th International Refrigeration and Air Conditioning Conference*, Purdue University, West Lafayette, IN, USA, July 11-14, 2016.

D. Bacellar, V. Aute, R. Radermacher, **Wavy Fin Profile Optimization using NURBS for Air-to-Refrigerant Tube-Fin Heat Exchangers with Small Diameter Tubes**, *16th International Refrigeration and Air Conditioning Conference*, Purdue University, West Lafayette, IN, USA, July 11-14, 2016.

D. Bacellar, V. Aute, R. Radermacher, **CFD-Based Correlation Development for Air Side Performance of Wavy Fin Tube Heat Exchangers using Small Diameter Tubes**, *16th International Refrigeration and Air Conditioning Conference*, Purdue University, West Lafayette, IN, USA, July 11-14, 2016.

Z. Huang, Y. Hwang, V. Aute, R. Radermacher, **Review of Fractal Heat Exchangers**, *16th International Refrigeration and Air Conditioning Conference*, Purdue University, West Lafayette, IN, USA, July 11-14, 2016.

Z. Huang, J. Ling, Y. Hwang, V. Aute, R. Radermacher, **Design and Numerical Parametric Study of Fractal Heat Exchanger**, *16th International Refrigeration and Air Conditioning Conference*, Purdue University, West Lafayette, IN, USA, July 11-14, 2016.

Y. Shabtay, Z. Huang, V. Aute, V. Sharma, R. Radermacher, **Manufacturing & Testing of Air-to-Refrigerant Heat Exchangers Based on 0.8mm Diameter Tubes,** *16th International Refrigeration and Air Conditioning Conference*, Purdue University, West Lafayette, IN, USA, July 11-14, 2016.

D. Bacellar, V. Aute, Z. Huang, R. Radermacher, **Airside Friction and Heat Transfer Characteristics for Staggered Tube Bundle in Crossflow Configuration with Diameters from 0.5mm to 2.0mm**, *International Journal of Heat and Mass Transfer*, vol. 98, pp. 448-454, July 2016.

Z. Huang, Y. Hwang, R. Radermacher, **Review of Nature-Inspired Heat Exchanger Technology**, *International Journal of Refrigeration*, vol. 78, pp. 1-17, June 2017.

Z. Huang, J. Ling, Y. Hwang, V. Aute, R. Radermacher, **Design and Numerical Parametric Study of Fractal Heat Exchanger** (Submitted to *Science and Technology for the Built Environment*).

D. Bacellar, V. Aute, Z. Huang, R. Radermacher, **Design Optimization and Validation of High Performance Heat Exchangers using Multi-Scale Approximation Assisted Optimization and Additive Manufacturing** (Submitted to *Science and Technology for the Built Environment*).

D. Bacellar, Z. Huang, V. Aute, J. Tancabel, R. Radermacher, **Multi-Scale Analysis, Shape Optimization, and Experimental Validation of Novel Air-to-Refrigerant Heat Exchangers** (Extended abstract accepted as Oral Communication, *9th World Conference on Experimental Heat Transfer, Fluid Mechanics, and Thermodynamics*).

6 List of Inventions

Air-to-Refrigerant Heat Exchangers with Parameterized Tube Shapes, Invention Disclosure No. PS-2015-112, September/2015

High-Performance Air-to-Refrigerant Heat Exchangers Using Small Round Tubes, Invention Disclosure No. PS-2015-130, October/2015

Integrated Air-to-Refrigerant Heat Exchanger and Impeller, Invention Disclosure No. PS-2014-181, Provisional Patent No. 62/264692, December/2015

7 Future Work

Many new avenues of study have emerged from the results of this study. The following are some examples of potential future work:

- 1.0kW prototypes two-phase flow testing

- 10kW prototype re-manufacturing
- 10kW prototype water and two-phase flow testing
- 13kW condenser optimization analysis
    - Prototype manufacturing
    - Testing and validation
- 10.5kW Evaporator optimization analysis
    - Prototype manufacturing
    - Testing and validation
- System level evalutation and optimization

8 References

[1] S. Pantakar, Numerical Heat Transfer and Fluid Flow, New York, NY, USA: McGraw-Hill, 1980.

[2] R. Shah, "Advances in Science and Technology of Compact Heat Exchangers," *Heat Transfer Engineering,* vol. 27, no. 5, pp. 3-22, 2006.

[3] S. Paitoonsurikarn, N. Kasagi and Y. Suzuki, "Optimal Design of Micro Bare-Tube Heat Exchanger," in *Proceedings of Symposium on Energy Engineering in the 21st Century*, Hong Kong, 2000.

[4] N. Saji, S. Nagai, K. Tsuchiya, H. Asakura and M. Obata, "Development of a Compact Laminar Flow Heat Exchanger with Stainless Steel Micro-Tubes," *Physica C,* vol. 354, pp. 148-151, 2001.

[5] R. Hilbert, G. Janiga, R. Baron and D. Thevenin, "Multi-Objective Shape Optimization of a Heat Exchanger using Parallel Genetic Algorithms," *International Journal of Heat and Mass Transfer,* vol. 49, pp. 2567-2577, 2006.

[6] P. Ranut, G. Janiga, E. Nobile and D. Thevenin, "Multi-Objective Shape Optimization of a Tube Bundle in Cross-Flow," *International Journal of Heat and Mass Transfer,* vol. 68, pp. 585-598, 2014.

[7] T. Shih, J. Zhu and J. Lumley, "A New Reynolds Stress Algebraic Equation Model," NASA Lewis Research Center, Cleveland, 1994.

[8] U. Schumann, "Realizability of Reynolds-Stress Turbulence Models," *Physics of Fluids,* vol. 20, no. 5, pp. 721-725, 1977.

[9] T. Schmidt, "Heat Transfer Calculations for Extended Surfaces," *Refrigerating Engineering,* vol. 57, no. 4, pp. 351-357, 1949.

[10] T. Ympa, "Historical development of the Newton-Raphson method," *SIAM Review,* vol. 37, no. 4, pp. 531-551, 1995.

[11] C. Roy and W. L. Oberkampf, "A Comprehensive Framework for Verification, Validation, and Uncertainty Quantification in Scientific Computing," *Computational Methods in Applied Mechanics and Engineering,* vol. 200, pp. 2131-2144, 2011.

[12] ASME, "Standard for Verification and Validation in Computational Fluid Dynamics and Heat Transfer," ASME, New York, NY, USA, 2009.

[13] P. Roach, "Quantification of Uncertainty in Computational Fluid Dynamics," *Annual Review of Fluid Mechanics,* vol. 29, pp. 123-160, 1997.

[14] W. Oberkampf and G. Trucano, "Verification and Validation in Computational Fluid Dynamics," Sandia National Laboratories, Albuquerque, NM, USA, 2002.

[15] W. Oberkampf and C. Roy, Verification and Validation in Scientific Computing, Cambridge, UK: Cambridge University Press, 2010.

[16] D. Bacellar, V. Aute, O. Abdelaziz and R. Radermacher, "Design of Novel Air-to-Refrigerant Heat Exchangers Using Approximation Assisted Optimization," in *ASME 2014 Verification & Validation Symposium,* Las Vegas, NV, USA, 2014.

[17] H. Jiang, V. Aute and R. Radermacher, "CoilDesigner: A General Purpose Simulation and Design Tool for Air-to-Refrigerant Heat Exchangers," *International Journal of Heat and Mass Transfer,* vol. 29, pp. 601-610, 2006.

[18] J. Winkler, V. Aute and R. Radermacher, "Comprehensive Investigation of Numerical Methods in Simulating a Steady-State Vapor Compression System," *International Journal of Refrigeration,* vol. 31, no. 5, pp. 930-942, 2008.

[19] S. A. Klein and F. L. Alvarado, *EES: Engineering Equation Solver for the Microsoft Windows Operating System,* F-Chart Software, 1992.

[20] C. Wang, W. Tao and C. Chang, "An Investigation of the Airside Performance of the Slit Fin-and-Tube Heat Exchangers," *International Journal of Refrigeration,* vol. 22, no. 8, pp. 595-603, 1999.

[21] M. Beshr, V. Aute and R. Radermacher, "Multi-Objective Optimization of a Residential Air Source Heat Pump with Small-Diameter Tubes using Genetic Algorithms," *International Journal of Refrigeration,* vol. 67, pp. 134-142, 2016.

[22] ASHRAE, "ANSI/ASHRAE Standard 33-2000, Method of Testing Forced Circulation Air Cooling and Air Heating Coil," Atlanta, GA, USA, 2000.

[23] ASHRAE, "Standard 41.2-1987, Standard Methods for Laboratory Air-Flow Measurement," Atlanta, GA, USA, 1987.

Table 21 – Project Timeline.

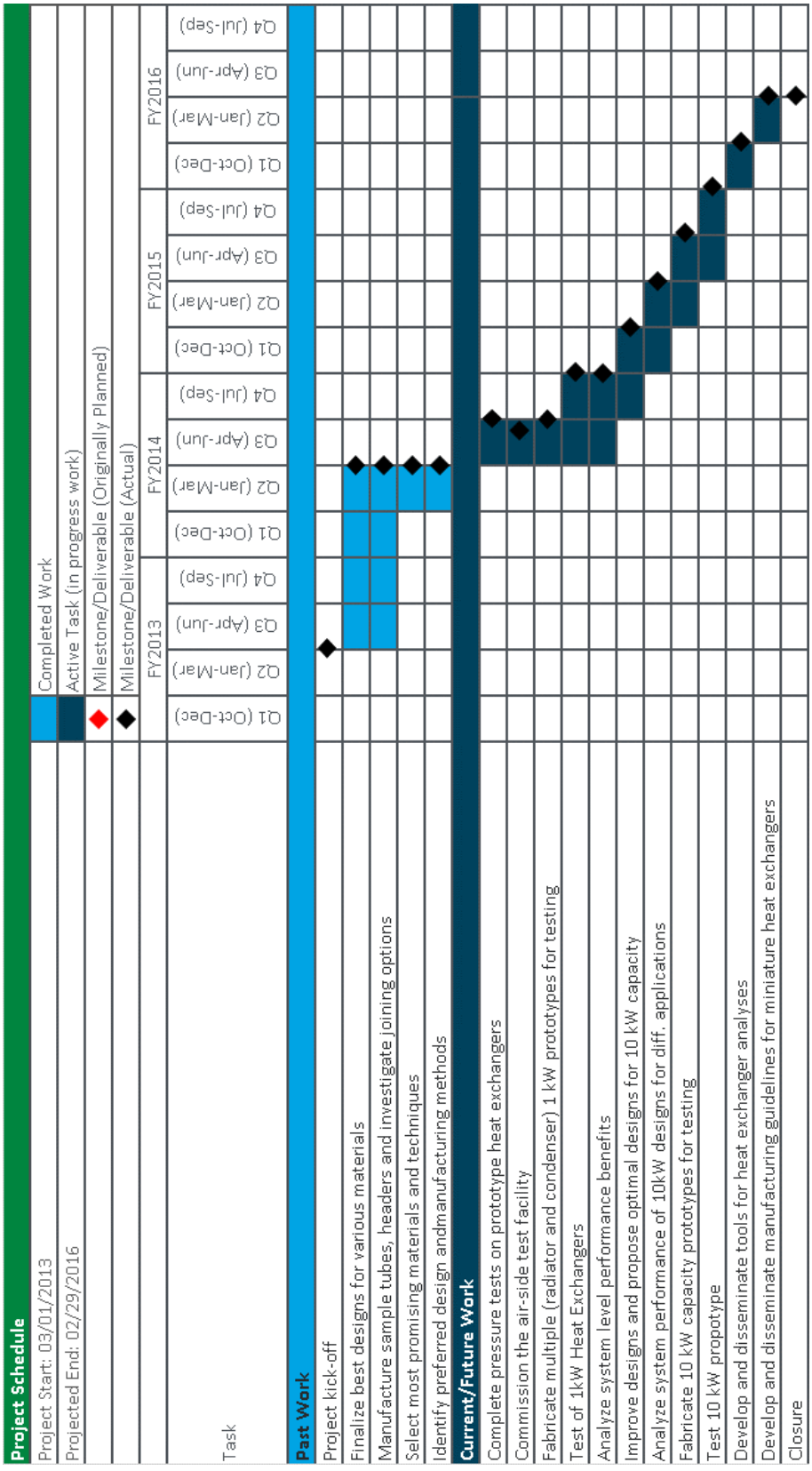

Appendix A – Round Bare Tubes

Two designs from the 0.8mm tube OD curve were chosen for prototyping. Design 1 and 2 (Table 8) were built by Heat Transfer Technologies; the 1 kW air-to-water testing was tested at ORNL facilities.

Table 22 – BTHX Designs being Manufactured.

Design Variable	Unit	Design
OD	mm	0.79
ID	mm	0.59
Pl	mm	1.19
Pt	mm	1.24
Banks	-	4
Rows	-	121
Tube Length	mm	152

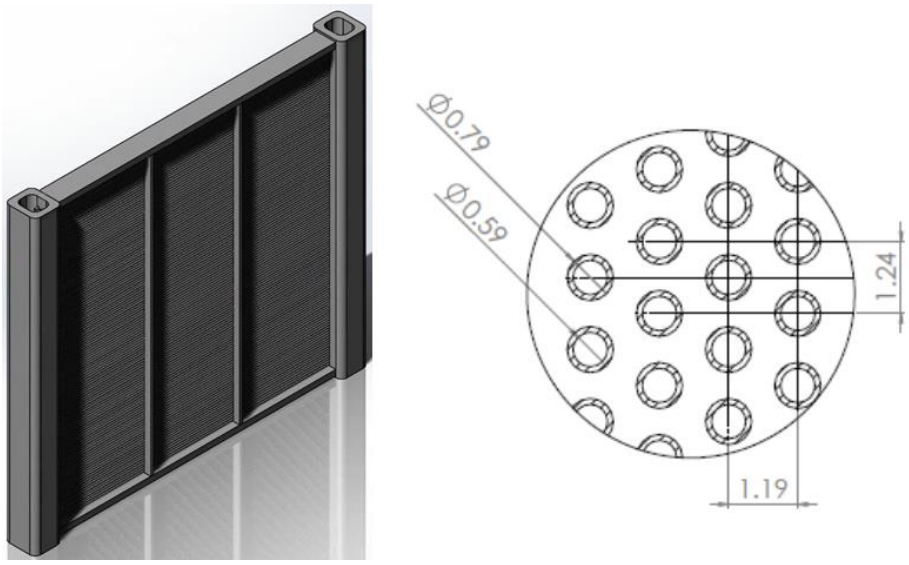

Figure 79 – BTHX Optimum Design.

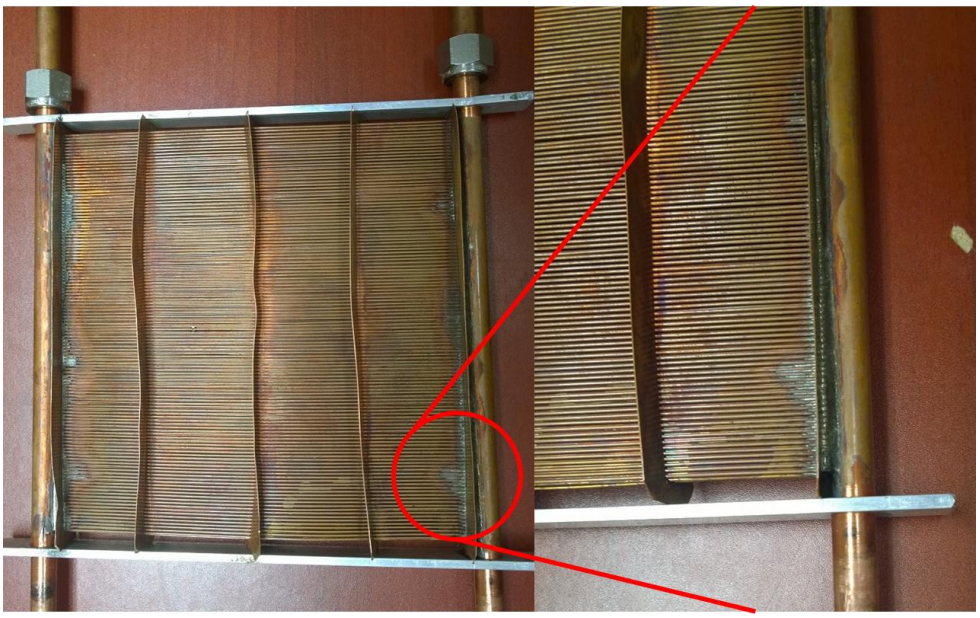

Figure 80 – BTHX Copper Version.

Figure 81 – BTHX Stainless Steel Version.

Appendix B – NURBS Shape Tubes

Previous analysis showed the potential of improvement by including tube shape parametrization to the optimization. A more comprehensive approach would allow the optimizer find the best shape instead of imposing a curve. The Non-Uniform Rational B-Spline (NURBS) shall handle such problem (Figure 82). Although many degrees of freedom are introduced, only important design variables are used to best evaluate the problem. The NURBS with unitary weight vector and highest polynomial order is the case where the curves are the so-called Bezier curves, frequently used in aerospace applications. Such curves will be used for the tube shape parametrization, where the control point are the design variables (Eq. (41).

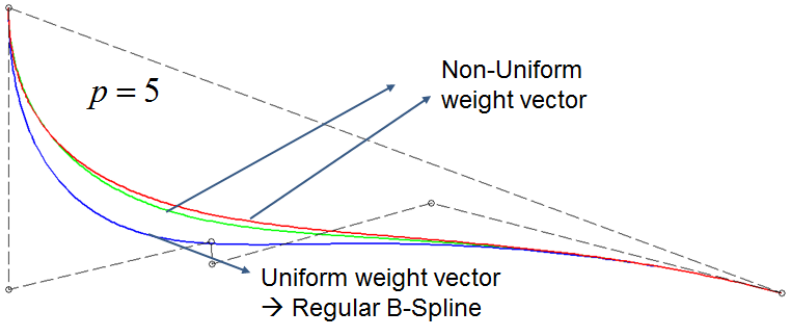

Figure 82 – NURBS Curves generated for a given Control Polygon.

$$C(u) = \sum_{i=1}^{n} \binom{n}{i} (1-u)^{1-i} u^{i} P \tag{41}$$

Additionally, problem complexity can be extended by assuming an asymmetric tube shape and even angle of attack (i.e. the camber line is a straigth line that can be tilted over the air flow direction) (Figure 83).

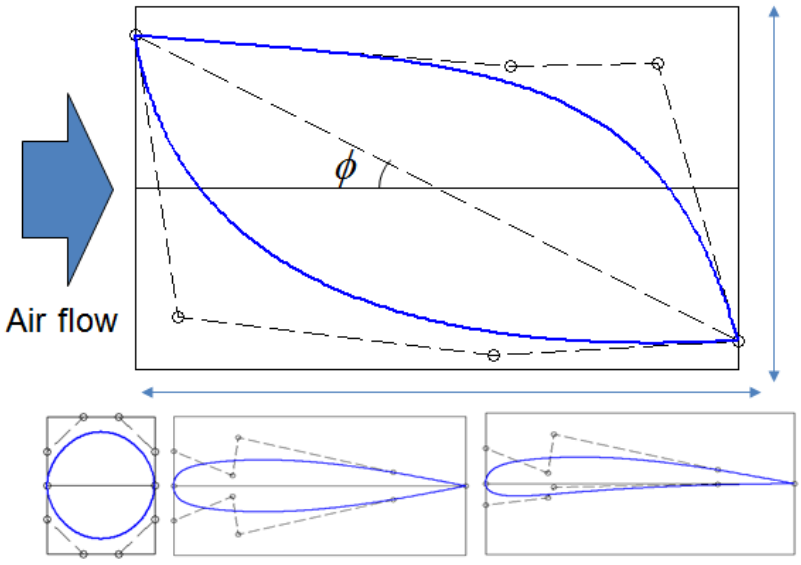

Figure 83 – Tube Shape Parameterization.

Appendix C – BTHX-001 Test Data Tables

Table 23 – Dry Conditions

66 cfm	Tin [°C]		Tout [°C]		RHin [%]		RHout [%]		Volume Flow Rate [m3/s]		Mass Flow Rate [g/s]		Pressure drop [Pa]		Capacity [W]		Heat Loss [W]		Adjusted Capacity [W]		Energy Balance [%]
Air-Side	26.67	± 0.11	17.21	± 0.11	13.7%	± 0.2%	23.8%	± 0.4%	0.0310	± 0.0005	37.79	± 0.63	29.0	± 1.2	361.1	± 8.5	-14.4	346.7	± 8.5	2.4%	0.0%
Water- Side	11.87	± 0.05	15.99	± 0.05	-		-		-		20.11	± 0.20	2.5	± 0.5	346.7	± 7.1	-	346.7	± 7.1	2.0%	
Air-Side	26.67	± 0.11	16.63	± 0.06	14.0%	± 0.3%	25.4%	± 0.4%	0.0310	± 0.0005	37.80	± 0.63	28.9	± 1.2	383.3	± 8.0	-12.8	370.5	± 8.0	2.2%	-2.0%
Water- Side	11.92	± 0.05	14.41	± 0.05	-		-		-		34.89	± 0.20	6.1	± 0.5	363.1	± 9.8	-	363.1	± 9.8	2.7%	
Air-Side	26.67	± 0.09	16.42	± 0.08	13.4%	± 0.2%	24.4%	± 0.4%	0.0310	± 0.0005	37.83	± 0.63	29.1	± 1.1	391.6	± 8.0	-13.2	378.4	± 8.0	2.1%	-2.7%
Water- Side	11.95	± 0.04	13.70	± 0.04	-		-		-		50.16	± 0.09	9.9	± 0.5	368.1	± 12.0	-	368.1	± 12.0	3.3%	

130 cfm	Tin [°C]		Tout [°C]		RHin [%]		RHout [%]		Volume Flow Rate [m3/s]		Mass Flow Rate [g/s]		Pressure drop [Pa]		Capacity [W]		Heat Loss [W]		Adjusted Capacity [W]		Energy Balance [%]
Air-Side	26.69	± 0.08	19.81	± 0.10	14.1%	± 0.2%	20.8%	± 0.4%		± 0.0005	74.68	± 0.59	84.3	± 1.9	519.0	± 10.5	-35.4	483.6	± 10.5	2.2%	0.1%
Water- Side	12.17	± 0.13	17.86	± 0.12	-		-		-		20.34	± 0.25	2.2	± 0.5	484.2	± 16.2	-	484.2	± 16.2	3.3%	
Air-Side	26.73	± 0.09	18.89	± 0.05	14.3%	± 0.3%	22.4%	± 0.4%	0.0615	± 0.0005	74.51	± 0.65	83.8	± 1.9	590.1	± 9.3	-33.0	557.1	± 9.3	1.7%	-2.4%
Water- Side	11.76	± 0.03	15.44	± 0.04	-		-		-		35.34	± 0.08	5.6	± 0.5	543.7	± 7.6	-	543.7	± 7.6	1.4%	
Air-Side	26.82	± 0.08	18.67	± 0.05	15.0%	± 0.4%	23.9%	± 0.6%	0.0613	± 0.0005	74.27	± 0.59	83.3	± 1.9	611.6	± 8.6	-35.0	576.6	± 8.6	1.5%	-3.2%
Water- Side	11.91	± 0.04	14.56	± 0.04	-		-		-		50.27	± 0.09	9.8	± 0.5	558.2	± 12.4	-	558.2	± 12.4	2.2%	

193 cfm	Tin [°C]		Tout [°C]		RHin [%]		RHout [%]		Volume Flow Rate [m3/s]		Mass Flow Rate [g/s]		Pressure drop [Pa]		Capacity [W]		Heat Loss [W]		Adjusted Capacity [W]		Energy Balance [%]
Air-Side	26.61	± 0.09	20.91	± 0.08	15.9%	± 0.3%	21.8%	± 0.4%	0.0917	± 0.0011	110.70	± 1.33	155.5	± 1.8	637.6	± 15.5	-75.7	561.9	± 15.5	2.8%	-0.2%
Water- Side	12.14	± 0.14	18.62	± 0.13	-		-		-		20.70	± 0.07	2.2	± 0.5	560.9	± 16.8	-	560.9	± 16.8	3.0%	
Air-Side	26.65	± 0.10	20.33	± 0.06	21.9%	± 0.5%	30.9%	± 0.7%	0.0912	± 0.0013	109.00	± 1.55	152.4	± 1.8	697.8	± 16.3	-36.8	661.0	± 16.3	2.5%	-4.1%
Water- Side	11.82	± 0.03	16.13	± 0.04	-		-		-		35.18	± 0.11	6.2	± 0.5	634.4	± 7.9	-	634.4	± 7.9	1.2%	
Air-Side	26.63	± 0.12	20.17	± 0.08	24.3%	± 0.7%	34.7%	± 1.0%	0.0912	± 0.0013	108.10	± 1.55	150.4	± 1.9	708.6	± 18.8	-21.9	686.7	± 18.8	2.7%	-3.5%
Water- Side	11.81	± 0.05	14.96	± 0.05	-		-		-		50.32	± 0.10	10.6	± 0.5	663.3	± 15.3	-	663.3	± 15.3	2.3%	

Table 24 – Wet Conditions, Inlet RH=51%

66 cfm	Tin [°C]		Tout [°C]		RHin [%]		RHout [%]		Volume Flow Rate [m3/s]		Mass Flow Rate [g/s]		Pressure drop [Pa]		Capacity [W]		Heat Loss [W]	Adjusted Capacity [W]		Energy Balance [%]
Air-Side	26.56	± 0.11	18.26	± 0.05	50.3%	± 1.0%	81.8%	± 1.1%	0.0339	± 0.0006	40.28	± 0.70	88.5	± 2.7	360.9	± 27.5	8.5	369.4	± 27.5	7.4%
Water- Side	12.00	± 0.05	16.21	± 0.05	-		-		-		20.26	± 0.09	3.3	± 0.5	356.9	± 6.1	-	356.9	± 6.1	1.7%
Air-Side	26.79	± 0.13	17.43	± 0.06	50.6%	± 1.0%	86.8%	± 1.2%	0.0328	± 0.0006	38.88	± 0.72	98.9	± 3.1	404.6	± 27.4	11.8	416.4	± 27.4	6.6%
Water- Side	12.04	± 0.04	14.77	± 0.05	-		-		-		35.16	± 0.08	6.6	± 0.5	402.2	± 9.7	-	402.2	± 9.7	2.4%
Air-Side	26.77	± 0.09	16.92	± 0.06	50.7%	± 0.7%	87.3%	± 1.2%	0.0322	± 0.0007	38.34	± 0.85	104.7	± 3.7	445.0	± 22.3	-7.1	437.9	± 22.3	5.1%
Water- Side	11.89	± 0.04	13.87	± 0.05	-		-		-		50.38	± 0.11	10.6	± 0.5	418.9	± 13.0	-	418.9	± 13.0	3.1%
130 cfm	Tin [°C]		Tout [°C]		RHin [%]		RHout [%]		Volume Flow Rate [m3/s]		Mass Flow Rate [g/s]		Pressure drop [Pa]		Capacity [W]		Heat Loss [W]	Adjusted Capacity [W]		Energy Balance [%]
Air-Side	26.70	± 0.10	20.27	± 0.06	51.2%	± 1.0%	74.8%	± 1.0%	0.0626	± 0.0006	74.62	± 0.77	150.8	± 2.6	504.1	± 50.7	-11.7	492.4	± 50.7	10.3%
Water- Side	12.07	± 0.05	17.92	± 0.05	-		-		-		20.39	± 0.07	3.6	± 0.5	498.5	± 5.8	-	498.5	± 5.8	1.2%
Air-Side	26.69	± 0.12	19.46	± 0.07	51.3%	± 1.0%	77.6%	± 1.5%	0.0619	± 0.0005	73.83	± 0.65	165.5	± 3.6	585.1	± 58.5	-6.7	578.4	± 58.5	10.1%
Water- Side	12.06	± 0.05	15.90	± 0.06	-		-		-		35.10	± 0.09	6.8	± 0.5	563.5	± 11.6	-	563.5	± 11.6	2.1%
Air-Side	26.74	± 0.10	19.04	± 0.07	51.4%	± 1.0%	79.9%	± 1.1%	0.0616	± 0.0005	73.50	± 0.65	180.0	± 3.9	624.1	± 50.2	-4.4	619.7	± 50.2	8.1%
Water- Side	11.99	± 0.04	14.93	± 0.05	-		-		-		50.32	± 0.09	10.8	± 0.5	617.7	± 14.4	-	617.7	± 14.4	2.3%
193 cfm	Tin [°C]		Tout [°C]		RHin [%]		RHout [%]		Volume Flow Rate [m3/s]		Mass Flow Rate [g/s]		Pressure drop [Pa]		Capacity [W]		Heat Loss [W]	Adjusted Capacity [W]		Energy Balance [%]
Air-Side	26.71	± 0.10	21.14	± 0.16	51.5%	± 1.4%	71.6%	± 1.6%	0.0900	± 0.0015	108.20	± 1.79	214.9	± 2.6	625.7	± 102.3	-25.9	599.8	± 102. 3	17.1%
Water- Side	12.00	± 0.05	18.67	± 0.06	-		-		-		20.60	± 0.14	3.4	± 0.5	574.8	± 7.5	-	574.8	± 7.5	1.3%
Air-Side	26.77	± 0.08	20.56	± 0.06	51.3%	± 1.3%	73.9%	± 1.4%	0.0912	± 0.0015	109.90	± 1.77	234.0	± 3.9	715.2	± 102.0	-27.5	687.7	± 102. 0	14.8%
Water- Side	12.06	± 0.04	16.60	± 0.06	-		-		-		34.80	± 0.09	6.7	± 0.5	660.6	± 10.6	-	660.6	± 10.6	1.6%
Air-Side	26.76	± 0.12	20.02	± 0.10	51.0%	± 1.4%	75.7%	± 1.5%	0.0895	± 0.0017	108.00	± 2.02	243.1	± 4.5	769.7	± 100. 7	-24.3	745.4	± 100. 7	13.5%
Water- Side	12.01	± 0.05	15.41	± 0.08	-		-		-		50.43	± 0.09	10.9	± 0.5	716.1	± 19.7	-	716.1	± 19.7	2.7%

Table 25 – Wet Conditions, Inlet RH=70%

66 cfm	Tin		Tout		RHin		RHout		Volume Flow Rate		Mass Flow Rate		Pressure drop		Capacity		Heat Loss	Adjusted Capacity		Energy Balance
	[°C]		[°C]		[%]		[%]		[m3/s]		[g/s]		[Pa]		[W]		[W]	[W]		[%]
Air-Side	26.68	± 0.09	18.63	± 0.12	70.6%	± 1.4%	98.0%	± 2.0%	0.0322	± 0.0006	38.15	± 0.73	95.3	± 3.1	542.9	± 39.6	7.0	549.9	± 39.6	7.2%
Water-Side	11.90	± 0.05	18.24	± 0.07	-	-	-	-	-	-	20.18	± 0.16	3.6	± 0.5	535.3	± 8.2	-	535.3	± 8.2	1.5%
Air-Side	26.68	± 0.11	17.85	± 0.06	70.2%	± 1.4%	97.2%	± 1.3%	0.0323	± 0.0006	38.42	± 0.73	93.1	± 3.4	640.1	± 35.2	9.4	649.5	± 35.2	5.4%
Water-Side	11.87	± 0.05	16.09	± 0.05	-	-	-	-	-	-	35.19	± 0.08	6.6	± 0.5	621.9	± 9.7	-	621.9	± 9.7	1.6%
Air-Side	26.76	± 0.11	17.31	± 0.05	69.4%	± 1.4%	98.7%	± 1.3%	0.0308	± 0.0008	36.51	± 0.89	86.0	± 3.2	645.3	± 34.9	11.2	656.5	± 34.9	5.3%
Water-Side	11.79	± 0.04	14.83	± 0.07	-	-	-	-	-	-	50.18	± 0.09	10.2	± 0.5	639.1	± 16.9	-	639.1	± 16.9	2.6%

130 cfm	Tin		Tout		RHin		RHout		Volume Flow Rate		Mass Flow Rate		Pressure drop		Capacity		Heat Loss	Adjusted Capacity		Energy Balance
	[°C]		[°C]		[%]		[%]		[m3/s]		[g/s]		[Pa]		[W]		[W]	[W]		[%]
Air-Side	26.70	± 0.08	20.61	± 0.06	70.1%	± 0.9%	93.4%	± 1.2%	0.0614	± 0.0006	72.99	± 0.72	213.4	± 4.0	674.4	± 50.2	-13.7	660.7	± 50.2	7.6%
Water-Side	11.81	± 0.05	19.62	± 0.05	-	-	-	-	-	-	20.16	± 0.19	2.3	± 0.5	658.7	± 8.5	-	658.7	± 8.5	1.3%
Air-Side	26.74	± 0.11	19.87	± 0.06	70.4%	± 1.4%	93.6%	± 1.2%	0.0609	± 0.0006	72.54	± 0.72	222.1	± 4.5	859.4	± 64.0	-8.5	850.9	± 64.0	7.5%
Water-Side	11.74	± 0.05	17.45	± 0.05	-	-	-	-	-	-	35.15	± 0.09	5.8	± 0.5	838.8	± 10.5	-	838.8	± 10.5	1.2%
Air-Side	26.67	± 0.10	19.49	± 0.09	70.2%	± 1.4%	93.4%	± 1.8%	0.0609	± 0.0006	72.56	± 0.66	223.8	± 4.8	927.8	± 72.5	-6.5	921.3	± 72.5	7.9%
Water-Side	11.84	± 0.06	16.16	± 0.08	-	-	-	-	-	-	50.22	± 0.09	10.2	± 0.5	907.8	± 20.0	-	907.8	± 20.0	2.2%

193 cfm	Tin		Tout		RHin		RHout		Volume Flow Rate		Mass Flow Rate		Pressure drop		Capacity		Heat Loss	Adjusted Capacity		Energy Balance
	[°C]		[°C]		[%]		[%]		[m3/s]		[g/s]		[Pa]		[W]		[W]	[W]		[%]
Air-Side	26.77	± 0.07	21.53	± 0.06	71.1%	± 0.9%	93.3%	± 1.2%	0.0909	± 0.0015	107.60	± 1.77	279.9	± 0.6	751.4	± 76.9	-31.0	720.4	± 76.9	10.7%
Water-Side	11.98	± 0.05	20.47	± 0.06	-	-	-	-	-	-	20.59	± 0.08	2.7	± 0.5	731.6	± 7.2	-	731.6	± 7.2	1.0%
Air-Side	26.61	± 0.09	20.66	± 0.06	71.4%	± 1.4%	93.7%	± 1.2%	0.0903	± 0.0015	107.00	± 1.78	279.9	± 0.6	1001.0	± 96.6	-24.4	976.6	± 96.6	9.9%
Water-Side	11.89	± 0.05	18.30	± 0.06	-	-	-	-	-	-	35.19	± 0.08	6.1	± 0.5	944.2	± 11.8	-	944.2	± 11.8	1.2%
Air-Side	26.77	± 0.09	20.27	± 0.06	70.3%	± 0.9%	93.6%	± 1.2%	0.0900	± 0.0015	106.80	± 1.79	279.9	± 0.6	1129.0	± 75.2	-22.8	1106.2	± 75.2	6.8%
Water-Side	11.85	± 0.05	16.93	± 0.05	-	-	-	-	-	-	50.02	± 0.11	10.1	± 0.5	1064.0	± 14.7	-	1064.0	± 14.7	1.4%

66 cfm	Energy Balance
	[%]
Air-Side	-2.7%
Water-Side	
Air-Side	-4.3%
Water-Side	
Air-Side	-2.7%
Water-Side	

130 cfm	Energy Balance
	[%]
Air-Side	-0.3%
Water-Side	
Air-Side	-1.4%
Water-Side	
Air-Side	-1.5%
Water-Side	

193 cfm	Energy Balance
	[%]
Air-Side	1.5%
Water-Side	
Air-Side	-3.4%
Water-Side	
Air-Side	-3.9%
Water-Side	